Aristotle University of Thessaloniki

Modeling and Optimization of 3D Stem Cell Bioprocesses

By
Romuald GYŐRGY

under the supervision of
Professor Michael C. Georgiadis

A thesis submitted in partial fulfillment of the requirements
for the degree of Doctor of Philosophy in the

Department of Chemical Engineering

December 2022

Declaration of authorship

I, Romuald GYŐRGY, declare that this thesis titled “Modeling and Optimization of 3D Stem Cell Bioprocesses” and the work presented in it are my own. I confirm that:

- This work was done wholly while in candidature for a research degree at this University.
- Where any part of this thesis has previously been submitted for a degree or any other qualification at this University or any other institution, this has been clearly stated.
- Where I have consulted the published work of others, this is always clearly attributed.
- Where I have quoted from the work of others, the source is always given. Except for such quotations, this thesis is entirely my own work.
- I have acknowledged all main sources of help.
- Where the thesis is based on work done by myself jointly with others, I have made clear exactly what was done by others and what I have contributed myself.

Signed: _____

Date: _____

Modeling and Optimization of 3D Stem Cell Bioprocesses

By Romuald GYŐRGY

Examination committee members

Michael C. Georgiadis
Professor
Supervisor
Department of Chemical Engineering
Aristotle University of Thessaloniki

Athanasios Mantalaris
Professor
Advisory Committee Member
Wallace H. Coulter Department of Biomedical Engineering
Georgia Institute of Technology, Atlanta, GA, USA

Margaritis Kostoglou
Professor
Advisory Committee Member
Department of Chemistry
Aristotle University of Thessaloniki

Andreana N. Assimopoulou
Associate Professor
Examiner
Department of Chemical Engineering
Aristotle University of Thessaloniki

Christos Chatzidoukas
Assistant Professor
Examiner
Department of Chemical Engineering
Aristotle University of Thessaloniki

Alexandros D. Kiparissides
Assistant Professor
Examiner
Department of Chemical Engineering
Aristotle University of Thessaloniki

Xanthippi S. Chatzistavrou
Assistant Professor
Examiner
Department of Chemical Engineering
Aristotle University of Thessaloniki

“Computers are useless. They can only give you answers.”

(Pablo Picasso, 1968)

ARISTOTLE UNIVERSITY OF THESSALONIKI

Abstract

Faculty of Engineering
Department of Chemical Engineering

Doctor of Philosophy

Modeling and Optimization of 3D Stem Cell Bioprocesses

By Romuald GYŐRGY

Clinical need for bone implants has been steadily increasing in the last few decades. The rising demand is partially attributed to the rise in living standards across the world and a corresponding increase in the percentage of elderly people (who are more susceptible to injury) in the general population.

Together with the rising demand, newer medical procedures that are more effective and are associated with fewer risks (such as donor site morbidity) have been developed. Both in the past, and to continue the useful trend into the future, cells suitable for implantation in critical sized bone defects can be produced by the *in-vitro* expansion and osteogenic differentiation of stem cells.

To help make such experimental processes more efficient — both in terms of cost, as well as the quality of the product (bone cell implant) — mathematical models can accelerate the model-based optimization of the experimental techniques used for producing the implants, and the cells contained within the implants themselves.

Towards this end, this PhD thesis introduces two mathematical models for the osteogenic differentiation of mesenchymal stem cells *in vitro*. The first model addresses osteogenic differentiation in well-plate cultures and is

constructed around a population balance core that enables it to capture and deconvolute cell cycle heterogeneity; it also incorporates the activity of key intracellular metabolic pathways (*i.e.*, glycolysis and tricarboxylic acid cycle) and representative osteogenic genes (*Runx2* and *osteonectin*). The mathematical model is built from first-principles and obeys mass conservation laws. The key finding based on simulation results implies the existence of a tradeoff between proliferation and differentiation, predicting a delay in the onset of differentiation when cells are allowed to cycle faster. The simulations leading to this conclusion did not model energy competition and suggest that the tradeoff is intrinsic, beyond the constraints imposed by the limited availability of energy molecules within cells.

The mathematical model is then extended to a rotating-wall bioreactor, whereby cells (cultured in a three-dimensional environment) are encapsulated in alginate-gelatin beads, introducing a multiscale description of the osteogenic differentiation process: from the cellular size scale, through the alginate-gelatin bead scale, to the bioreactor size scale. The mathematical model incorporates the same metabolic pathways and key genes, additionally capturing spatial heterogeneity within the beads. The discretized formulation of the model consists of 12,563 simultaneous ordinary differential equations. Predicted metabolic changes and gene activation (*Runx2* and *osteonectin*) in alginate-gelatin-bead-encapsulated cells are slightly delayed compared with well-plate cultures, result attributed to mass transfer limitations within the hydrogel bead.

Global sensitivity analysis revealed that parameters related to gene expression (decay rates and gene transcription activation constants) carry the most significance and should be the focus of future parameter estimation efforts. Hydrogel bead size does not meaningfully impact simulation outcomes for beads smaller than 4 mm in diameter. An analysis of the mathematical model renders the outcome of the simulations qualitatively correct, within the limitations imposed by the reduced subset of metabolites and genes included in the model.

The mathematical models introduced by the research showcased in this thesis can function as a framework for future model-based bioreactor and bioprocess optimization. Due to the large size of the mathematical model in terms

of number of equations, the multiscale model requires the use of high-performance computing systems to reduce the currently prohibitive time required to solve optimization problems on a single computer.

Περίληψη

Η κλινική ανάγκη για οστικά εμφυτεύματα αυξάνεται σταθερά τις τελευταίες δεκαετίες. Η αυξανόμενη αυτή ζήτηση αποδίδεται εν μέρει στην άνοδο του βιοτικού επιπέδου παγκοσμίως και στην σημαντική αύξηση του ποσοστού των ηλικιωμένων (που είναι πιο επιρρεπείς σε τραυματισμούς) στον γενικό πληθυσμό.

Παράλληλα με την αυξανόμενη ζήτηση, έχουν αναπτυχθεί νεότερες ιατρικές τεχνικές που είναι πιο αποτελεσματικές και συνδέονται με λιγότερους κινδύνους (όπως η νοσηρότητα του δότη). Τόσο στο παρελθόν, όσο και για να συνεχιστεί η χρήσιμη τάση στο μέλλον, κύτταρα κρίσιμου μεγέθους, κατάλληλα για εμφύτευση σε οστικά ελαττώματα, μπορούν να παραχθούν με την in vitro ανάπτυξη και την οστεογονική διαφοροποίηση των βλαστοκυττάρων.

Για να γίνουν πιο αποτελεσματικές τέτοιες πειραματικές διεργασίες — τόσο από άποψη κόστους όσο και από άποψη ποιότητας του τελικού προϊόντος (εμφύτευμα οστικών κυττάρων) — μαθηματικά μοντέλα μπορούν να επιταχύνουν τη βελτιστοποίηση (βάσει μοντέλου) των πειραματικών τεχνικών που χρησιμοποιούνται τόσο για την παραγωγή των εμφυτευμάτων όσο και την ανάπτυξη των κυττάρων που περιέχονται στα ίδια τα εμφυτεύματα.

Η παρούσα διατριβή προτείνει αρχικά ένα μαθηματικό μοντέλο για την οστεογονική διαφοροποίηση των μεσεγχυματικών βλαστοκυττάρων *in vitro*. Τα μοντέλα έχουν αναπτυχθεί γύρω από ένα πληθυσμιακό ισοζύγιο που επιτρέπει την λεπτομερή μοντελοποίηση της εγγενούς ετερογένειας του κυτταρικού κύκλου, ενσωματώνοντας τη δραστηριότητα βασικών ενδοκυτταρικών μεταβολικών οδών (κύκλος γλυκόλυσης και τρικαρβοξυλικού οξέος) και αντιπροσωπευτικά οστεογονικά γονίδια. Το μοντέλο βασίζεται σε θεμελιώδεις αρχές και ισχύοντες νόμους διατήρησης. Τα αποτελέσματα της προσομοίωσης των μοντέλων αποδεικνύουν την ύπαρξη αντιστάθμισης μεταξύ του πολλαπλασιασμού και της διαφοροποίησης των κυττάρων, προβλέποντας μια καθυστέρηση στην έναρξη της διαφοροποίησης όταν τα κύτταρα αφήνονται να ανακυκλωθούν ταχύτερα.

Το αρχικό μαθηματικό μοντέλο επεκτείνεται στη συνέχεια σε έναν βιοαντιδραστήρα περιστρεφόμενου τοιχώματος, όπου τα κύτταρα

ενθυλακώνονται σε σφαιρίδια αλγινικής ζελατίνης, εισάγοντας έτσι την δυνατότητα περιγραφής πολλαπλών κλιμάκων της διαδικασίας διαφοροποίησης: από την κλίμακα κυτταρικού μεγέθους, μέσω της κλίμακας σφαιριδίων αλγινικής ζελατίνης και τέλος στην κλίμακα μεγέθους του βιοαντιδραστήρα. Το μαθηματικό μοντέλο ενσωματώνει τις ίδιες μεταβολικές οδούς και βασικά γονίδια, καταγράφοντας επιπλέον τη χωρική ετερογένεια μέσα στα σφαιρίδια. Το διακριτοποιημένο μοντέλου αποτελείται από 12.563 συνήθεις διαφορικές εξισώσεις. Οι συγκεντρώσεις βασικών μεταβολιτών (π.χ. γλυκόζη, πυροσταφυλικό, γλουταμίνη, γαλακτικό) συγκρίνονται με πειραματικά δεδομένα από καλλιέργειες στατικών πλακών φρεατίων, αποδεικνύοντας ότι οι προβλέψεις του μοντέλου είναι ικανοποιητικές. Φαίνεται επίσης ότι η γονιδιακή ενεργοποίηση (Runx2 και οστεονεκτίνη) σε κύτταρα ενθυλακωμένα με σφαιρίδια αλγινικής ζελατίνης καθυστερεί ελαφρώς σε σύγκριση με καλλιέργειες σε πλακίδια . Μια ολική ανάλυση ευαισθησίας αποκαλύπτει ότι οι παράμετροι που σχετίζονται με την έκφραση των γονιδίων (ρυθμοί διάσπασης και σταθερές ενεργοποίησης μεταγραφής γονιδίων) έχουν τη μεγαλύτερη βαρύτητα και θα πρέπει να αποτελούν το επίκεντρο της μελλοντικής εκτίμησης παραμέτρων. Το μέγεθος των σφαιριδίων υδρογέλης δεν επηρεάζει σημαντικά τα αποτελέσματα της προσομοίωσης για διαμέτρους σφαιριδίων στην περιοχή 2–3 mm.

Τα μαθηματικά μοντέλα που παρουσιάζονται σε αυτή τη διατριβή μπορούν να εξασφαλίσουν ένα υπολογιστικό πλαίσιο για την μελλοντική βελτιστοποίηση βιοαντιδραστήρων και βιοδιαδικασιών βάσει μοντέλων. Λόγω του μεγάλου μεγέθους τους, τα προτεινόμενα μοντέλα πολλαπλής κλίμακας απαιτούν τη χρήση υπολογιστικών συστημάτων υψηλής απόδοσης για τη μείωση του επί του παρόντος υψηλού υπολογιστικού χρόνου που απαιτείται για την επίλυση τέτοιων προβλημάτων βελτιστοποίησης σε έναν μόνο υπολογιστή.

Acknowledgements

I find myself at an important milestone of my life's journey. Looking back upon the voyage thus far, there are countless people who have shaped me, either by their words, or through their actions, and sometimes by their stillness.

To enable me to undertake the doctoral journey, first I had to be born. I am grateful to my parents for lending me part of their own designs and for raising me, alongside my extended family, including my grandparents, and my great-grandmother who shaped me in my early years. I am grateful to my (older) siblings for frequently challenging me intellectually and helping me uncover my interest in structured logical thinking and language semantics.

Many teachers and educators have guided me along the way. I am particularly grateful to my maternal language and mathematics teachers from secondary school and high school, and most of all to my high-school chemistry teacher, Mariana Doicescu. I would like to express my gratitude and appreciation towards my bachelor's and master's degree supervisor, professor Sorin Bîldea, for his adaptive teaching strategy and specifically for building a friendship underneath our student-professor relationship.

I am thankful for the funding offered through the European Union Horizon 2020 research and innovation programs, under the Marie Skłodowska-Curie SyMBioSys ITN, grant agreement no. 675585. The financial support offered by the program is the pragmatic aspect that convinced me to leave my home country and seek international experience. I would like to thank Professor Athanasios Mantalaris for coordinating this European project and for setting ambitious goals for my own research. I am thankful to my supervisor, Professor Michael Georgiadis, who welcomed me into his research group and placed me on a path filled with challenging topics such as mathematical model formulation and numerical solution methods applied to systems biology and bioprocess optimization. Looking back on the last few years I feel pride in having accomplished the ambitions that I set out to achieve at the beginning of the PhD and recognize the vital role that my supervisor had in enabling all this. I am also grateful to Prof. Georgiadis for the many people that I was introduced to during

my years in Thessaloniki. I am thankful to Professor Margaritis Kostoglou for our discussions on mathematical model formulation. Stemming from insight gathered during these conversations, I worked relentlessly to produce a mathematical model that not only matches experimental data but is also built from first principles (balance equations) and, therefore, more robust.

The research presented in this thesis has substantially benefited from my partnership with Michail Klontzas (Imperial College, London, UK), who performed most of the experiments that have been used in this work, from probing for behavior to include in the mathematical representation, to experiments used in the estimation of parameters and the validation of the mathematical model. I am also thankful for his friendship, and that of other early-stage researchers involved in the SyMBioSys ITN.

I am thankful to Magda Kalaitzidou, George Nikolaidis, and Spyros Mastrogeorgopoulos for helping me to get settled and adapt to the Greek culture at the beginning of my doctoral journey. I am also grateful for meeting and becoming friends with Panos Karakostas, Apostolis Elekidis, and George Georgiadis. I was fortunate enough to be an advisor for the bachelor thesis of Foteini Zagklavara, who became my friend.

In the final stages of my doctoral journey, I started teaching university classes in Romania, made new friendships with Ana Maria Brezoiu, and strengthened older ones, with Ionuț Banu; I am indebted to him for helping me find the surge of motivation that enabled me to complete this thesis.

I am grateful for my fate in having met the love of my life, Teodora, more than a decade ago, and for having been together through these years. I am also thankful for my daughter who, despite having no scientific involvement in my thesis, contributes immensely to my life with her joyous outlook.

Table of contents

List of figures

List of tables

List of abbreviations

ATP	adenosine triphosphate
DNA	deoxyribonucleic acid
mRNA	messenger RNA
MSC	mesenchymal stem cell
NADH	nicotinamide adenine dinucleotide (and hydrogen)
OBC	osteoblast
PBE	population balance equation
PBM	population balance model
PRE	pre-osteoblast
RHS	right-hand side
RNA	ribonucleic acid
TCA *cycle*	tricarboxylic acid *cycle*, also known as the Krebs or citric acid *cycle*
TGF	transforming growth factor
UCB	umbilical cord blood

Nomenclature

Latin letters

$A_{Gi}^{(TYP)}$ [*dimensionless*] – RNA transcription activator level for gene i (Runx2, or osteonectin) in cells at differentiation state TYP

$C_{IN,m}$ [pmol/L] – concentration of metabolite m (glucose, lactate, or glutamine) in the reactor feed (culture medium)

CC_m [pmol/L] – concentration of metabolite m (glucose, lactate, or glutamine) in the culture medium

$C_m(r,t)$ [pmol/L] – concentration of metabolite m (glucose, lactate, or glutamine) inside the alginate-gelatin bead

$C_{M_i,out}$ [pmol/L] – extracellular concentration of metabolite i (glucose, lactate, or glutamine) inside the alginate-gelatin bead

CPD_G [*dimensionless*] – cumulative probability distribution function indicating the fraction of cells which differentiate while traversing phase G, before reaching growth coordinate x (given by the argument of the function)

C_{R_i} [pmol/L] – intracellular concentration of the metabolite that plays the role of the reactant in the i^{th} intracellular reaction; i ranges between 1 and 9

Dex_{cell} [nmol/L] – intracellular dexamethasone concentration

$Dex_{culture}$ [nmol/L] – dexamethasone concentration in the culture medium

$Dex_{bead}(r,t)$ [nmol/L] – dexamethasone concentration in the alginate-gelatin bead at radial position r (and time t)

$D_{in}^{(TYP)}$ [cell/L/day] – growth-coordinate-dependent differentiation rate of cells into differentiation state TYP (from the preceding state); $D_{in}^{(TYP)} = D_{out}^{(TYP-1)}$

$D_{out}^{(TYP)}$ [cell/L/day] – growth-coordinate-dependent differentiation rate into the next state after differentiation state TYP; $D_{out}^{(TYP)} = D_{in}^{(TYP+1)}$

$\mathcal{D}_m$ [dm²/day] – mass diffusion coefficient of metabolite m (glucose, lactate, or glutamine) in water

dxp [*dimensionless*] – differentiation exponent

$duration_{\pi}^{(TYP)}$ [day] – duration of phase π (G, S, or M) for cells at differentiation state TYP (MSC, PRE, or OBC)

$E_m^{(TYP)}$ [L/pmol] – conversion factor relating the production of energy cofactor m (ATP or NADH) to the duration of phase G for cells at differentiation state TYP

$f_{diff}^{(TYP)}$ [*dimensionless*] – fraction of cells that are leaving state TYP while traversing phase G by differentiating into (phase G of) the next state, before they can transition to the synthesis phase (of the current state TYP)

F_{IN} [L/day] – culture medium perfusion flowrate

F_m [pmol/dm²/day] – molar flux density vector for metabolite m (glucose, lactate, or glutamine) inside the alginate-gelatin bead

$F_{m,r}$ [pmol/dm²/day] – radial component of molar flux for metabolite m inside the alginate-gelatin bead, in the radial direction, oriented from the center toward the outer surface of the bead

$G_i^{(TYP)}$ [*dimensionless*] – relative expression level of gene i (Runx2 or osteonectin) in cells at differentiation state TYP

$G_{key}^{(TYP)}$ [*dimensionless*] – relative expression of the gene that controls differentiation from differentiation state TYP; $G_{key} = Runx2$ for mesenchymal stem cells and $G_{key} = osteonectin$ for pre-osteoblasts

i [*dimensionless*] – counter variable ranging from 1 up to the number of variables of the specified category (8 intracellular metabolites, 2 genes, 9 intracellular metabolic reactions, 3 cross-membrane transport flows, etc.)

$k_{bead,m}$ [dm/day] – mass transport coefficient for transfer of metabolite m between the culture medium and the (surface of the) alginate-gelatin bead

$k_{cat,i}$ [day⁻¹] – kinetic constant for intracellular reaction i; $i \in \overline{1,9}$

k_{decay} [day⁻¹] – RNA decay rate

$k_{DNA,i}$ [*dimensionless*] – DNA binding constant for the RNA transcription of gene i (Runx2 or osteonectin)

$k_{E,i}^{(TYP)}$ [L/day] – cross-membrane transport coefficient for the enzyme connected with flowrate i for cells at differentiation state TYP; see also: $TRate_i^{(TYP)}$; $i \in \overline{1,3}$

$k_{T,i}$ [pmol/L] – transport inhibition constant for cross-membrane transport flowrate i; $i \in \overline{1,3}$

$k_{trans,i}$ [day⁻¹] – RNA transcription rate for gene i (Runx2 or osteonectin); $i \in \overline{1,2}$

$M_m^{(TYP)}$ [pmol/L] – intracellular concentration of intracellular metabolite (or energy cofactor) m in cells at differentiation state TYP

$M_{T_i}^{(TYP)}$ [pmol/L] – intracellular concentration of metabolite transported across the cell membrane by flowrate i

N_{bead} [*dimensionless*] – number of (alginate-gelatin) beads inside the perfusion reactor

N_R [*dimensionless*] – number of intracellular metabolic reactions included in the mathematical description of osteogenesis ($N_R = 9$)

N_T [*dimensionless*] – number of cross-membrane transport reactions included in the mathematical description of osteogenesis ($N_T = 3$)

$N_{total}^{(TYP)}$ [cell/L] – total count of cells at differentiation state TYP

n_{trans} [*dimensionless*] – RNA transcription exponent

$N_\pi^{(TYP)}$ [cell/L] – cell count distribution of cells at differentiation state TYP that are currently traversing the π cell division cycle phase

$P_{norm}(x, \mu, \sigma)$ [*dimensionless*] – cumulative normal probability function, parameterized by the mean value μ and standard deviation σ; the symbol μ is used here for the mean value of the distribution and has the meaning of phase traversal rate elsewhere in the thesis (see $\mu_\pi^{(TYP)}$)

$P_\pi(x)$ [*dimensionless*] – cumulative probability of transition to the subsequent phase in the cell cycle; $\pi \in \{G, M\}$

r [dm] – radial coordinate inside the alginate-gelatin bead sphere

R_{bead} [dm] – outer radius of spherical alginate-gelatin beads

Re [*dimensionless*] – Reynolds number

$RRate_i^{(TYP)}$ [pmol/L/day] – rate of intracellular metabolic reaction i for cells at differentiation state TYP

RV_{Dex} [pmol/L/day] – net volumetric equivalent generation rate for dexamethasone inside the hydrogel bead

RV_m [pmol/L/day] – net volumetric equivalent generation rate for metabolite m inside the hydrogel bead (for glucose, lactate, and glutamine)

Sc_m [*dimensionless*] – Schmidt number, for extracellular metabolite m

Sh_m [*dimensionless*] – Sherwood number, for extracellular metabolite m

$STOIC_{m,i}$ [*dimensionless*] – stoichiometric coefficient of metabolite m for intracellular metabolic reaction (or cross-membrane transport) i

t [day] – time

$T_{\pi,in}^{(TYP)}$ [day^{-1}] – transition rate into phase π, for cells at differentiation state TYP

$T_{\pi,out}^{(TYP)}$ [day^{-1}] – distributed transition rate (onto the next phase in the cell cycle) for cells at differentiation state TYP that are traversing phase π

$TRate_i^{(TYP)}$ [pmol/day] – cross-membrane transport flowrate i for cells at differentiation state TYP

TYP [*dimensionless*] – one of the three differentiation states considered by the mathematical model: mesenchymal stem cell (MSC=1), pre-osteoblast (PRE=2), or osteoblast (OBC=3)

V_{cell} [L] – average cell volume

V_R [L] – volume of culture medium inside the containing vessel (*e.g.*, a well plate or a bioreactor)

x [*dimensionless*] – cell cycle phase coordinate

$x_{max,\pi}$ [*dimensionless*] – upper bound of the phase coordinate domain for cell cycle phase π

$x_{min,\pi}$ [*dimensionless*] – lower bound of the phase coordinate domain for cell cycle phase π

$x_{threshold,\pi}$ [*dimensionless*] – average value of the phase coordinate at transition into the next cell cycle phase from phase π; applicable only to phases G and M

Greek letters

$\delta(x_1, x_2)$ [*dimensionless*] – Kronecker delta function; takes the value 1 if the two arguments are equal and 0 otherwise

$\theta_\pi^{(TYP)}$ [day^{-1}] – cell death rate for cells at differentiation state TYP while traversing growth phase π

$\lambda_{membrane}$ [L/day] – permeability coefficient for the mass transport of dexamethasone through the cell membrane

$\mu_\pi^{(TYP)}$ [day^{-1}] – cell cycle traversal rate for cells at differentiation state TYP, while traversing growth phase π

π [*dimensionless*] – subscript; one of the three cell cycle phases described by the mathematical model: phase G ($\pi = 1$), phase S ($\pi = 2$), or phase M ($\pi = 3$) – ratio between the length of the circumference and the diameter of a circle; the meaning of the symbol π should be clear based on the context in which it appears

ω_i [day^{-1}] – base expression rate of gene i in mesenchymal stem cells

Chapter 1. Introduction

1.1. Motivation and objectives

Currently, there is a continuously increasing clinical demand for bone implants for a wide variety of surgical procedures for bone loss alleviation, most often involving bone tissue in the head and limbs. In grafting procedures, autografts are preferable to allografts as they mitigate the risk of disease transmission, but they do have shortcomings such as limited availability and donor site morbidity. Available synthetic graft substitutes generally lack osteoinductive or osteogenic properties [1]. There is currently no system that can mimic all the biological functions of autografts, clinical practice uses composite grafts combining scaffolding with biological elements that stimulate cell differentiation and osteogenesis [2]. As the incidence of bone disorders continues to increase, bone tissue engineering may provide a viable alternative to conventional grafts [3] by combining stem cells, biomaterial scaffolds, and biologically active growth factors to make bone grafts readily available [4]. Meeting these increasingly high demands can be achieved with the use of stem cells that can be differentiated *in vitro* towards the osteogenic lineage, aiming to produce cells suitable for implantation in critical-size bone defects. High-quality engineered grafts require efficient osteogenic differentiation of stem cells, ensuring extracellular matrix protein secretion and successful integration with the patients' own tissue. In the specialized field of osteogenic stem cell differentiation, mesenchymal stem cells (MSCs) are the predominant focus of cellular research efforts, owing to their high osteogenic differentiation capacity and availability from multiple cell sources of fetal and adult origin, including umbilical cord blood, which present increased proliferative capacity and immunomodulatory properties. [5–7].

During osteogenesis stem cell cultures consist of heterogeneous populations at various stages of differentiation and in different cell cycle growth phases. Most experimental techniques measure population-aggregated values, masking cell-to-cell variability and overlooking the heterogeneous nature of the cell culture. A comprehensive understanding of the evolution of the different coexisting cell populations during the osteogenic differentiation process can

support culture and reactor level optimization by providing a necessary instrument in the production of high-quality bone constructs [8]. Furthermore, bioreactor phenomena inherently occur at multiple scales simultaneously. Since more details are available during simulation, multiscale mathematical models describing the bioreactor at all relevant geometric scales support superior bioprocess control precision, potentially leading to improved stem cell products that are better suited to clinical applications for the treatment of bone defects and injuries.

To sum up in a single sentence, the main goal of the thesis is to develop and implement a mathematical model to capture heterogeneity across many scales in biosystems using population balance modelling. In service of the main goal, the following objectives should be achieved:

- The formulation of a mathematical description of a single cell cycle phase to describe the traversal of representative growth stages within the larger function of cellular duplication, using population balances. When faced with multiple options for the design of the mathematical model, formulations where the parameters or variables carry biological or physical significance should be preferred.

- Inclusion of “ports” in the implementation of the mathematical model for cell cycle phases, which allows for cell cycle phases to connect and form the cell cycle without requiring correction factors between adjacent cell cycle phases to account for differences in phase duration, traversal rate, or numerical discretization scheme.

- The formulation of a reduced mathematical model for intracellular metabolism supported by *in-vitro* experimental results.

- A biologically accurate connection between the intracellular and extracellular compartments, allowing for metabolite transport across the cell membrane. The model should account for factors promoting and inhibiting the transport process.

- The formulation of a mathematical model to describe gene expression, considering the biological mechanism giving the order in which the genes are activated; the gene expression model should be connected to at least one exogenous signal that triggers and maintains the gene expression chain.

- Connection of the description of cell proliferation and differentiation, gene expression and intracellular metabolism with bioreactor scale mass transport phenomena, incorporating any intermediate scales into the model.

1.2. Stem cells

Complex multicellular organisms are generally comprised of a plethora of cell types performing various functions within the host organism. Cell types and their differences can be thoroughly characterized by referring to their shape, cell structure, function, gene expression, and biochemical composition. These cell types are referred to as differentiated or specialized cells and develop from less differentiated or undifferentiated counterparts (*i.e.*, stem cells) by means of a tightly regulated complex process, known as cellular differentiation [9].

Stem cells are functionally unspecialized cells that must possess two key capabilities: self-renewal, and multipotency. The proliferative (self-renewal) capability constitutes the main difference between stem cells and their more differentiated progeny and is the mechanism enabling stem cells to maintain their population size throughout the lifetime of the organism they reside within. Multipotency is the ability of stem cells to differentiate into multiple types of more specialized cells and is the reason why stem cells are the focus of many medical research teams around the world [10].

Evidence for the existence of stem cells dates to 1961, when it was observed that cell colonies were forming in the spleen of previously irradiated mice after being intravenously injected with bone marrow cells [11]. This experiment revealed the existence of hematopoietic stem cells and suggested that bone marrow transplantation could be used for the clinical treatment of blood formation disorders [12].

Stem cell populations are generally heterogeneous in terms of their shape and intracellular biochemical composition; cells may shift between different metastable states, possibly enabling stem cells to react to differentiation stimuli while simultaneously maintaining population numbers, depending on their state [13].

The results of some experimental tests for stemness depend on the response of the cells to specific environmental signals; one drawback of the resulting dynamic description of stemness is its unequivocal connection to a unique cell population, stemming from its dependence on environmental conditions [9]. Other approaches focus on the detection of certain stem cell markers that are specific to each cell type [14,15].

While all cell types found in living multicellular organisms are derived from embryonic stem cells, which exist during the early stages of life, adult (tissue) stem cells, which exist throughout the entire lifetime of the organism can only differentiate into a limited number of cell types. Adult stem cells are responsible for the maintenance and recovery after injury for the tissues they reside within [9].

Among the relatively large number of different kinds (of stem cells), pluripotent stem cells are those that can differentiate into cell types of any tissue of the body. There are two types of pluripotent stem cells recognized in publicly available scientific literature: embryonic stem cells (ESC) and induced pluripotent stem cells (iPSC). ESCs originate in the inner cell mass of embryos and can be cultured as pluripotent stem cells *in vitro* [16]. Alternatively, iPSCs can be obtained from adult cells by induced de-differentiation (or reprogramming of the cell) [17,18]. Both experimental techniques produce stem cells that can differentiate into all three germ layers (endoderm, mesoderm, and exoderm) and are also capable of undergoing unlimited cellular divisions [12]. Following the discovery of iPSCs, significant research efforts have focused on techniques to isolate and characterize them [19]. After they were first derived (in mice) in 1981 [20], pluripotent stem cells have enriched humanity’s understanding of essential areas of cellular biology and have provided the means to develop and test medical hypotheses and cell-based therapies [21].

Another important and widely researched type [22] is the hematopoietic stem cell (HSC), which can differentiate into any cell type from the blood cell lineage, such as: red blood cells, white blood cells, or thrombocytes [23]. Hematopoietic stem cells (HSCs), also referred to as blood stem cells, are found in the bone marrow, peripheral blood, and umbilical cord blood (UCB). HSCs are one of the essential cell sources in stem cell biology and are also used in the clinical treatment of blood cancers and regenerative diseases including non-hematopoietic tissue regeneration (*e.g.*, liver disease treatment). Despite their low numbers and relative rarity, hematopoietic stem cells are very active in the human body, producing about one trillion cells per day to maintain homeostasis [24]. Although bone marrow transplants have been successful at treating various hematopoietic deficiencies, significant immunological barriers affecting allogeneic blood stem cell transplants still exist; past and future research efforts focus on creating protocols for effective hematopoietic stem cell manipulation (such as genome editing) [25]. Currently, research on the transplantation of hematopoietic stem cells is still very active, with novel strategies for isolation, expansion, and implantation are continuously being developed [26].

While generally undesirable within the living body of individuals, cancer stem cells (CSCs) are also an important research topic; discovering markers that signal the existence of these cells [27] and using them in clinical settings to screen for known cancer types can be very impactful for patients, making it possible to treat the disease with diminished suffering of the individual or, in some cases, prevent their death (which would likely occur in the absence of early cancer detection). The existence of CSCs was first documented in leukemia, and in many other cancers since then [28], particularly in solid and blood cancers. Cancer stem cells have been proven to possess sustained self-renewal capacity and have been associated with cell proliferation and tumor growth. It is hypothesized that exposure to chemotherapy or radiotherapy may induce “stemness” in cancerous tissue cells, making tumors resistant to treatment [29]. The fact that CSCs generally constitute only a small fraction of the cell population within tumors [30] can make the cancer more difficult to treat, sometimes causing relapses even when the tumor has been physically removed from the patient [29].

Stem cells also play an important role in the production of monoclonal antibodies for a large variety of applications, such as in the treatment of leukemia [31]. Monoclonal antibodies can also be used to treat tumors by targeting key regulators of cancerous stem cells using a modeling framework to characterize the cells and specific molecules involved in the process; the approach shows promising results both in reducing the size as well as slowing the growth of the tumor [32]. In modeling the production of monoclonal antibodies, it is important to have access to a complete and accurate mathematical description the stem cell line that produces the antibodies facilitating the optimization of culture conditions and the produced antibodies, guiding experiment design, and potentially reducing the associated experimental costs and time-to-market [33]. Mathematical models that include the binding of antibodies to their targets are being developed, aiming to produce antibodies that target multiple receptors, which may mitigate the resistance to medication that some cancers acquire during clinical treatment [34]. More monoclonal antibodies are sanctioned for disease treatment every year, as their efficacy and safety increase. Biosimilar products promise to make the treatment of various diseases more accessible and affordable in the coming years [35]. Monoclonal antibodies have also been used in the COVID-19 pandemic [36] (which has affected a large part of the world in recent years), because one of their key advantages, particularly important during the sanitary crisis, is that treatments can be developed, manufactured, tested, and approved faster than in the case of vaccines or antimicrobials [37].

Mesenchymal stem cells (MSCs) are one of the major stem cell types. The first description of MSCs is attributed to a 1966 article, characterizing them as “a population of adherent, colony-forming, fibroblast-like cells able to undergo osteogenic differentiation” [38]; in addition to the osteogenic lineage, MSCs can also differentiate into muscle and cartilage cells, among several other types [39]. MSCs are stromal cells that can self-renew and differentiate into multiple cell lineages, and can be sourced from multiple tissues, the most practical for experimental and clinical applications being umbilical cord and menses blood, fat tissue and bone marrow. Although the highly complex mechanisms for MSC differentiation and mobilization present significant challenges for the research community, their multipotency makes them attractive for clinical applications [40].

In addition, MSCs possess anti-inflammatory and immune-modulatory properties, providing the greatest focus of human MSCs in clinical testing; *in-vitro* cultures suggest even broader applications with many clinical trials investigating medical applications of MSCs. Although the current understanding of mesenchymal stem cells is rooted in a strong scientific foundation, important details are not completely understood, such as intercellular and intracellular signaling [41].

Important phenotypic modifications mark the osteogenic differentiation route. One of the characteristic changes in mesenchymal stem cell physiology during osteogenesis is the shift of metabolic energy production from glycolysis to oxidative phosphorylation [42–46]. In addition to the metabolic changes that occur during osteogenic differentiation, a study of umbilical cord blood mesenchymal stem cells in laboratory conditions showed that metabolic activity is high during the first week of differentiation and decreases to an oxidative state analogous to that of osteoblasts during the second and third weeks [44]. The acquisition of the osteoblast phenotype is accompanied by changes in gene expression, including the Runt related transcription factor-2 (*Runx2*), expressed during the first few days of differentiation, and bone extracellular matrix-related genes that are expressed later in the differentiation process, such as *osteocalcin*, *osteonectin* and *bone sialoprotein* [47]. The transition from an undifferentiated proliferative phenotype to a differentiated one is linked to a gradual lengthening of the cell division cycle [48].

1.2.1. Mathematical models for stem cell proliferation and differentiation

Research into the dynamics of the cellular division cycle promises to have notable clinical impact, especially when informed by and coupled with the large amounts of biological data that are becoming accessible with recent technological advances [9]. Mathematical models for cell growth can be implemented and solved in a deterministic or stochastic manner. While some processes are inherently stochastic in nature [49], simulating large stochastic models is less feasible, due to the exponentially larger associated simulation duration of the larger models (in terms of the number of equations in the mathematical description); furthermore, when the process involves many stochastic

components (particles, cells, *etc.*) the average stochastic run is well represented by the equivalent deterministic solution.

Common mathematical formulations that describe cellular division and the cell cycle to various degrees of accuracy are (ordered from simple to complex): ordinary differential equations (ODE), delay differential equations (DDE), and population balance equations (PBE). Of the three listed approaches, ODEs are the simplest to implement and verify; DDEs improv the description of cultures where heterogeneity is important and are most suited if the delays (*i.e.*, cell cycle phase durations) are constant; PBEs are the most flexible option, correctly describing the distribution of cells within cell cycle phases and allowing for non-uniform growth, death, and transition events over the modelled cell cycle phase.

The cell cycle and stem cell proliferation are commonly described using ordinary differential equations (ODEs). An ODE-based model was applied to examine the lifespan and senescent behavior of periosteum derived progenitor cells, concluding that early-passage cells may be suitable for different applications than late-passage cells [50]. A mathematical model of MSC chondrogenesis was developed to investigate the effects of endogenous and exogenous transforming growth factor beta (TGF-β) on the chondrogenic differentiation of mesenchymal stem cells [51].

Although they are the simplest mathematical option for dynamic simulations, ordinary differential equations also have some shortcomings, particularly under cyclic or varying conditions; since each ODE only calculates one number (usually the total cell population of a compartment), it lacks a description of the cell density profile along the growth coordinate for that compartment. To address this issue, delay differential equations have been used in scientific publications in various fields, from leukemia chemotherapy [52] to mathematical modeling of HIV-AIDS [53].

The importance of cell cycle heterogeneity has been acknowledged in applications such as chemical cancer treatment [54]. Population balance models are used in a variety of scientific fields and are particularly valuable in applications with large numbers of entities that are distributed over a continuum of possible

states. Wu *et al.* used population balance models to study cell aggregation in stirred-suspension bioreactor cultures and identified the effect of cluster size on cellular oxygen availability and risk of hypoxia [55]. Bartolini *et al.* researched stem cell cycle dynamics and proliferation in suspension bioreactors by means of population balance equations; their results infer the existence of a non-trivial optimum cell concentration in suspension cultures [56]. More recently, Banerjee *et al.* constructed a mechanistic model for the agglomeration of Chinese hamster ovary cells in acoustic standing waves in which population balances were used to predict the particle size distribution and evaluate the cell separation efficiency of the technique [57]. Seidel and Eibl modelled oxygen supply in aerobic cultures and used population balances as one of the possible mathematical descriptions for bubble coalescence and breakup [58]; even without a direct description of the cells, the information provided by such a model can be very relevant for aerobic cell cultures by enabling the calculation of oxygen transfer rates from the gas phase into the aqueous phase.

1.2.1.1. Differentiation of stem cells

Stem cell differentiation phenomena are integrated in mathematical models by allocating each modelled cell type its own compartment and including additional differentiation-rate-related terms to the proliferation equations to track the number of cells transitioning between compartments [59]. If differentiation is modelled as a mitotic event, then differentiation can occur either by symmetric or asymmetric division; symmetric division produces two differentiated cells, while asymmetric division produces one differentiated cell and one stem cell. Targeted studies suggest that stem cell division is generally symmetric [60,61]. On the other hand, cell differentiation can also occur during the cell cycle, allowing for multiple cellular divisions before terminal differentiation at one end, or for successive differentiations across multiple compartments (or differentiation milestones) before undergoing mitosis at the other end [10].

1.3. Bioreactor modeling

Bioreactors are widely used for various applications, from general large-scale fermenters to micro-bioreactors that are used for more specific

purposes, including the culturing of mammalian stem cells in three-dimensional scaffolds [62].

The development of models that mimic the *in-vivo* environment can be technically challenging; for example, differentiation into and maintenance of cartilage tissue, requires high hydrostatic pressures to be applied at various strengths to resemble regular daily activity of the tissue, and poses the additional problem of mass-transfer-limited gas bubble removal from the culture medium and scaffolds [63].

Accurate models approach bioreactor modeling from a mechanistic point of view, carefully choosing the phenomena to be described mathematically (*e.g.*, temperature, metabolite concentrations, and pH) and ignoring less relevant aspects of the problem, based on insight and key assumptions [64].

Computer implementations of mathematical models can enhance description of fluid flow and cell dynamics and can help improve the geometry of scaffolds and aid in the design of experiments. Mathematical models also have their limitations, stemming from their simplification of reality and the validity of underlying assumptions. To ensure they are applicable, models should always be tested and validated if possible [65].

Mathematical models have been used to study oxygen mass transport limitations in biopharmaceutical processes, based on calculation of the mass transfer coefficient of oxygen and experimental measurement of the gas bubble size distribution; computational fluid dynamics simulations are presented as a viable alternative for improving the accuracy of empirical correlations while at the same time providing detailed cost-effective characterization of prototypes [66].

With recent advances in computing power a new level of model fidelity has emerged, termed “digital twin”, a highly detailed and accurate computer representation of a real process or device that has access to real-time process data. The virtual model can use a combination of simulation, machine learning and reasoning to generate valuable insight that is applicable to the original physical system [67]. The “digital twin” approach is slowly being adopted by the biochemical engineering industry and integrated into the design bioprocesses,

such as the *in-vitro* expansion of human mesenchymal stem cells, where the expansion process and cultivation methods are coupled with computational fluid dynamics (CFD) for modeling growth kinetics and local bioreactor characteristics (as opposed to averaged, global ones). CFD models and simulations are valuable tools with many applications including the determination of parameters that are difficult to determine experimentally [68].

A series of recent publications tackle computational fluid dynamics (CFD) and recognize the importance of multiscale mathematical descriptions for bioprocesses. Flow conditions (hydrodynamics) play a crucial role in chemical processes, due to their influence on sheer stresses, and mass and heat transfer. To enable the application of CFD models for practical bioengineering applications, their results require experimental validation; ultimately, such multiscale models support the use of digital twins for high performance and high accuracy process control [69]. A critical step of process development is the scale-up of laboratory-scale models; a scale-up methodology coupled with CFD and integrating cellular physiology could guide the development of future bioprocess designs [70]. In addition to the combination of biological models and CFD, data-driven modeling (*i.e.*, machine learning) also has the potential to accelerate and improve the development of digital twins that can guide the selection between biological models and aid scale-up calculations for fermentation and other bioprocesses [71]. Computational fluid dynamics are increasingly being used in tissue engineering applications, as computing power becomes more accessible and practical simulation knowledge spreads among researchers. For example, using fluid dynamics calculations, a recent study found that, in the case of a rotary bioreactor for esophagus tissue engineering, moderate perfusion and rotation speeds are appropriate experimental conditions for culture [72].

1.4. Global (parameter) sensitivity analysis

Global analysis techniques aim to assess the impact of the uncertainty (often conveyed using confidence intervals) in the values of the parameters of the model onto the prediction of the model, and to apportion the observed variance to each of the parameters subjected to the (global sensitivity) assessment. The

term *sensitivity* implies the (direct or indirect) use of derivatives, while the term *global* reveals that the result of the analysis is mediated over the entire parameter space. While local sensitivities are employed to identify the important parameters when using nominal values, global sensitivities reveal the important parameters when their values are allowed to vary in a specified parameter space [73] (*i.e.*, when there is inherent associated uncertainty in the nominal values of a model's parameters).

Sensitivity analysis can impactfully aid the modeling process at many stages of (its) development, such as identification, calibration, and verification; for example, sensitivity analysis can reveal if parts of the model can be lumped, kept at fixed values, or even completely removed, without affecting the outcome of the model. Although sensitivity analysis is very powerful and can potentially yield notable results in terms of model simplification or parameter identification, the analysis should only be applied to carefully selected outputs with clear meaning or purpose within the model; in this manner, the time required to perform the calculations is kept low, and the sensitivity analysis is more transparent [74].

1.4.1. A brief history of sensitivity analysis research

In 1995 two highly cited authors in the field of global sensitivity analysis (Sobol I. and Saltelli A.) introduced the method of rank transformation to calculate (first-order or main effect) sensitivity indices [75]. The methodology was further improved with the introduction of a technique allowing for the calculation of the "fractional contribution of the input parameters to the variance of the model prediction" and total effect sensitivity indices whose values capture synergetic interaction effects between each parameter and all the others, using rank transformation to boost the reproducibility of the approach [76].

Although the sensitivity analysis technique is very powerful, it was not immediately performed as routine practice, with many publications still using one-factor-at-a-time (OAT) analyses in 2005. Variance-based measures (and others) are described as easy to implement and capable of overcoming OAT shortcomings. Rigorously defining the concept of factor importance, renders the result of the analysis (*i.e.*, the ranking of the factors) unambiguous [77].

Global sensitivity analysis (GSA) is still an active research field. While GSA is mainly used to study the effects of uncertainty in the values of the inputs on the outputs of a model, GSA can also aid with variable selection in regression models, by applying a measure of global sensitivity to a model-fit criterion, in effect ranking the possible regression variables by importance; Becker et al. recently presented and demonstrated a method for model selection based on global sensitivity analysis [78].

1.4.2. High-dimensional model representation

The mathematical models presented in this thesis have been subjected to global sensitivity analysis using the GUI-HDMR software tool [79]; the tool offers a tried-and-tested method that has been used in the sensitivity analysis of multiple mathematical models at the Biological Systems Engineering Laboratory at Imperial College London [80]. Before the analysis, an uncertainty interval is chosen for each input (*i.e.*, all the parameters of a mathematical model, or a subset). Then, many sets of parameter values are generated for the selected inputs using the Sobol sequence [81,82], and the base simulation is repeated for each set of parameter values. When performing sensitivity analysis, it is crucial to cover as much as possible of the domain of interest for the parameters. The naïve rectangular grid approach becomes unfeasible for large numbers of factors (input parameters), since the total number of simulations to be carried out increases exponentially (with the number of factors). The Sobol sequence generates points that belong to a quasi-random point set which fills space in an efficient and highly uniform manner.

Based on the table of inputs and corresponding outputs obtained by repeated simulations, the GUI-HDMR software tool then computes first-order sensitivity indices $S_i^{(1)}$ and second-order contributions $S_{i,j}^{(2)}$ for each of the model outputs (denoted by the subscript index i or j). The total sensitivity index for any of the given outputs is calculated using equation (1.1). Parameters with a total sensitivity index above the threshold value of 0.1 [83] were deemed significant (*i.e.*, the design of future parameter estimation efforts should prioritize the refinement of these parameters' values).

$$TSI_i = S_i^{(1)} + \sum_{i \neq j} S_{i,j}^{(2)} \tag{1.1}$$

1.5. Thesis overview

The thesis has the following overall structure:

Chapter 2 tackles the development and implementation of a mathematical model for the osteogenic differentiation of mesenchymal stem cells cultured in well plates. The model is built from first principles, and the modeling approach relies on balance equations for all conserved quantities, from population balances modeling the traversal of cell division cycle phases, to mass balances for intracellular and extracellular metabolism and gene expression. Simulation results match experimental measurements for cell counts, metabolic and gene expression levels, confirming the model is appropriate. Sensitivity analysis reveals that the parameters carrying the most significance for the model are directly involved in the differentiation and proliferation behaviors of the cells. An uncertainty analysis of the effects of cell cycle duration reveals that there may be inherent trade-offs between proliferation and differentiation even if the two aspects of stem cell dynamics were not competing for energy resources.

Chapter 3 extends the mathematical model formulated in Chapter 2 by supplementing it with a description of the alginate-gelatin beads that stem cells are encapsulated in and of the bioreactor where the osteogenic differentiation process is carried out. This inclusion corresponds to a multiscale approach for bioreactor modeling, as it includes phenomena from the cellular, to the alginate-gelatin bead, and bioreactor scales. Although the multiscale approach is not a novel idea, mathematical models that implement it are scarce, because of the associated difficulties in the model formulation and solution stages. The results of the mathematical models from Chapter 2 and Chapter 3 are compared, highlighting both the similarities and the differences in their predictions. Chapter 3 concludes with an analysis designed to check the output of the mathematical model under various biologically meaningful scenarios, rendering the model adequate and its predictions qualitatively accurate from the biological point of view.

Chapter 4 summarizes the main results of the mathematical models presented in this thesis and their significance and suggests possible directions to complement osteogenic differentiation research.

Chapter 2. Mathematical modeling of the osteogenic differentiation of mesenchymal stem cells in well-plate culture

This chapter introduces a mathematical model for the *in-vitro* osteogenic differentiation of mesenchymal stem cells (MSCs). In the experiments supporting the development of the mathematical model, MSCs derived from umbilical cord blood (UCB) were isolated [44] and subsequently differentiated in well plates over a 21-day period. The process of MSCs isolation began with cord blood dilution and extraction of the mononuclear cells by density gradient centrifugation; cells were then washed with phosphate-buffered saline and suspended in a culture medium comprised of 89% αMEM GlutaMax-I [84], 10% fetal bovine serum, and 1% penicillin/streptomycin. The cells were then seeded in tissue culture flasks and incubated for two days at 37°C, 21% oxygen, and 5% CO_2. Non-adherent cells were then discarded, and culture continued until confluence, subculturing adherent MSCs until passage 5. For the 21-day osteogenic process, the same basal culture medium was used, supplemented with 10 mmol/L β-glycerophosphate, 50 mg/L ascorbic acid 2-phosphate, and dexamethasone to initiate osteogenic induction.

During osteogenesis, the concentrations of intracellular metabolites (that are included in the mathematical description) were determined based on published metabolomics data [44] by GC-MS analysis (gas chromatograph coupled to a mass spectrometer). Peak areas reported by the analysis were converted to concentration values (in pmol/L) by normalizing with ribitol concentration, which was used as an internal standard.

For gene expression measurements, RNA was extracted from the cells and quantified using real-time qRT-PCR (quantitative reverse transcription polymerase chain reaction): 5 minutes of reverse transcription at 42°C, followed by 3 minutes of enzyme inactivation at 95°C, and 40 cycles of 3-second denaturation at 95°C and 30 seconds of annealing at 62°C using a StepOne Plus

qRT-PCR instrument. After extraction, the expression of *Runx2* and *osteonectin* was measured by mRNA quantification using specific primers; the measurements were then normalized using RPL13a (ribosomal protein L13 antibody) as a housekeeping gene and expressed as relative mRNA levels.

Total cell counts were measured indirectly, by washing the cells with phosphate-buffered saline (PBS) and incubated overnight in a quantification buffer: 1 mmol/L EDTA, 10 mmol/L Tris, 0.1% Triton-X, and 0.1 mg/mL Proteinase K. After diluting the resulting DNA solution 1:10 using PBS, 100 µL of each sample were incubated in darkness with PicoGreen working solution. The fluorescence of the solution was measured using a fluorescence reader at 485 nm / 530 nm excitation/emission; finally, cell numbers were calculated based on a custom-made standard curve.

All measurements (intracellular metabolite concentration, relative gene expression levels, and total cell counts) were carried out on samples obtained at days 0, 7, 14, and 21 of the osteogenic differentiation process [85].

2.1. Mathematical model formulation

2.1.1. Assumptions

The following statements were assumed to be true during the development of the mathematical model:

- To divide, the cells must traverse three consecutive growth stages (*i.e.*, cell cycle phases). Cell division occurs at the end of the last cell cycle phase (*i.e.*, mitosis).
- Cell growth is directly proportional to the rate of energy currency production (ATP and NADH molecules) for each cell type (*i.e.*, differentiation state).
- Three differentiation states are considered. Mesenchymal stem cells may differentiate into pre-osteoblasts, which may differentiate into osteoblasts, in turn. Differentiation in the opposite direction is considered negligible in the presence of dexamethasone (the osteogenic differentiation agent).

Differentiation states cannot be skipped, but cells may quickly differentiate further, reaching the terminal point (*i.e.*, osteoblast state).

- The differentiation behavior is controlled by a key gene for each cell type. Gene expression of the two selected genes described by the model are enhanced by the presence of dexamethasone in the culture medium. Dexamethasone may be transferred across the cell membrane, regarded as a permeable barrier (together with the nuclear membrane).

- Cellular behaviors (metabolism, gene expression, growth, and differentiation) only depend on their current (intracellular) state. Cells have no memory of previous (intracellular and extracellular) environmental conditions. Cells react to changes in their environment instantaneously — while it takes time for their behavior to shift to the one matching their new state, there is no lag in beginning the state transition.

- Transport across the cell membrane obeys conservation of mass (e.g., for glucose, glutamine, lactate, and dexamethasone), contributing to the decrease in the transported component in the source compartment and to the increase of the same component in the destination compartment. Cells also obey the mass conservation law when they differentiate: no mass is created or destroyed during differentiation and the transition of metabolism and gene expression towards a new steady state requires time, influencing population-averaged measured concentration values during this process.

2.1.2. Structure of the mathematical model

The core component of the mathematical model consists of a concise description of intracellular metabolic and genetic activities coupled to cell growth (Figure 2.1) and differentiation (Figure 2.2). 8 metabolites from key pathways (glycolysis, oxidative phosphorylation, and glutaminolysis) that showed significant changes during osteogenesis [44] are included in the model. Four of the modelled intracellular metabolic reactions produce cofactors serving as energy currency in the cell [86,87]. Intracellular cofactor levels (ATP and NADH) were not explicitly modeled because of their intricate interactions with many other metabolic pathways that are nonessential to the analysis in this study; instead,

the production rates of energy cofactors are correlated with the traversal (growth) rate of cells during the Gap 1 (phase “G” in the mathematical model) cell cycle phase by means of a proportionality constant.

Figure 2.1 indicates the progression order for the cell cycle phases, as well as the experimentally determined duration for phases “S” (DNA synthesis) and “M” (lumped Gap 2 and mitosis) [85]; phase “G” represents the lumped Gap 0 and Gap 1 cell cycle phases. The differentiation agent (dexamethasone) crosses the cellular membrane, then the nuclear membrane, and indirectly activates the expression of Runt-related transcription factor 2 (*Runx2*) through a series of steps; in turn, *Runx2* triggers a chain of genetic activity leading to the expression of osteogenic genes, such as osteonectin [88]. The mathematical model concisely represents the transcription of *Runx2* and osteonectin genes as single-step interactions with their activators (dexamethasone and *Runx2*, respectively).

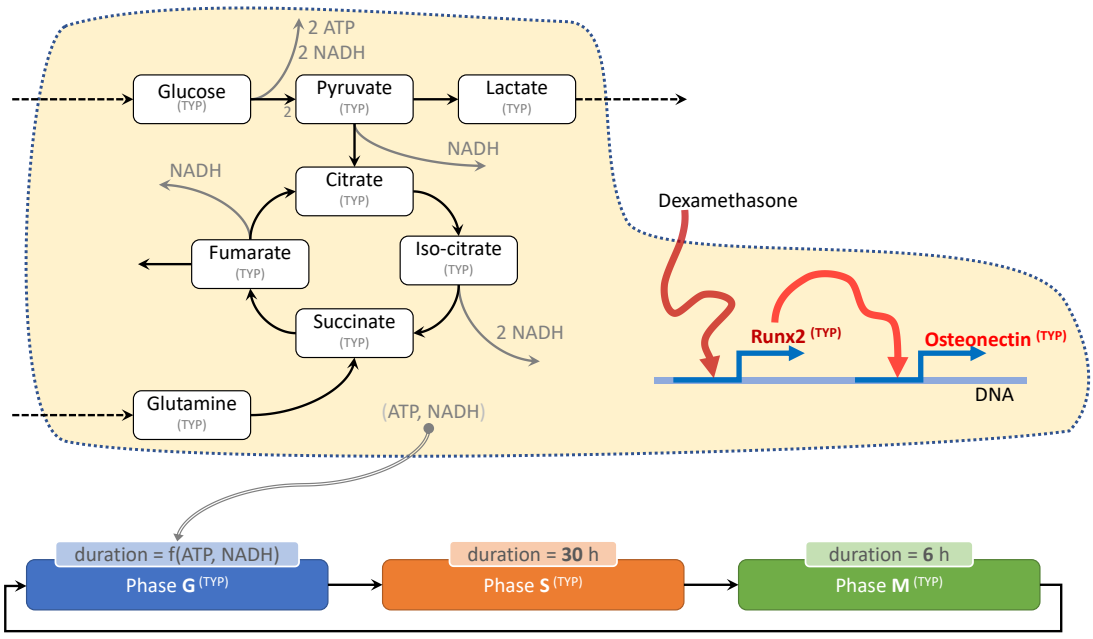

Figure 2.1. Visual representation of the structure of the mathematical model at the cellular scale: intracellular metabolism, gene expression, and cell division cycle. [89]

The osteogenic differentiation route of MSCs (Figure 2.2) is marked by three distinct milestones: the initial state (mesenchymal stem cells, labeled “MSC”), one intermediary state (pre-osteoblasts, labeled “PRE”), and the final state (osteoblast cells, labeled “OBC”). The placeholder “TYP” (used in Figure 2.1 and elsewhere throughout the mathematical model) represents any of the

differentiation states, as the mathematical description applies to each of them. Differentiation is restricted to phase G, as the objective of the cell shifts toward cell cycle completion and cellular division once the cell enters phase S (when DNA strain duplication occurs). Differentiation rates are controlled by the levels of gene expression of the two modelled genes: *Runx2* level in MSC cells controls their differentiation into PRE, while *osteonectin* in PRE cells controls their differentiation into osteoblasts (OBC); OBCs are the terminal point of differentiation. The values of constant entities of the mathematical model (*i.e.*, parameters) are given in Table 2.1 below.

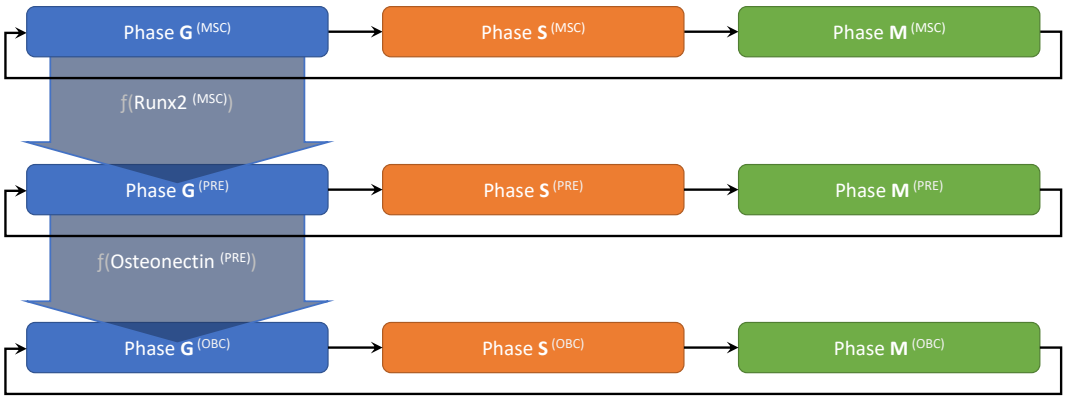

Figure 2.2. Visual representation of the structure of the mathematical model at the cell population level (scale): cell cycle heterogeneity and the osteogenic differentiation route; G=lumped Gap 0 and Gap 1; S=DNA synthesis phase; M=lumped Gap 2 and mitosis; MSC=mesenchymal stem cell; PRE=pre-osteoblast; OBC=osteoblast [89]

2.1.3. Balance equations for intracellular metabolism

Intracellular metabolic activity is succinctly characterized using the two most important pathways for the osteogenic differentiation of MSCs: glycolysis and oxidative phosphorylation [43,46]. A total of 8 experimentally measurable metabolites that showed significant concentration changes over the course of the differentiation process [44] are included in the mathematical model: glucose, pyruvate, lactate, citrate, iso-citrate, succinate, fumarate, and glutamine. The concentration levels of these metabolites are potentially different between cellular differentiation states and can also depend on time; the well plated cells are considered spatially homogeneous.

Figure 2.3 depicts the 8 metabolites that are part of the mathematical description of MSCs during osteogenic differentiation, as well as the chain of

metabolic reactions they are involved in. The figure also shows the production of energy-related cofactors (ATP and NADH) by some of the metabolic reactions. The yellow background represents the cell, while its dotted border represents the cell membrane. Three of the metabolites can be transported across the cell membrane, represented by dashed arrows indicating the direction of transport. Fumarate is involved as a reactant in two metabolic reactions: the first one is part of the TCA cycle and contributes to the production of citrate, while the second one contributes to the generation of other metabolites that were not included in the mathematical model. Although all the metabolites included in the mathematical description are involved in other intracellular reactions from several different metabolic pathways, only one such reaction was included, to allow the TCA cycle to reach a steady state within the framework of the current mathematical model — otherwise, metabolite levels withing the TCA cycle (involving citrate, iso-citrate, succinate, and fumarate) would continuously increase without bounds, which is not biologically accurate.

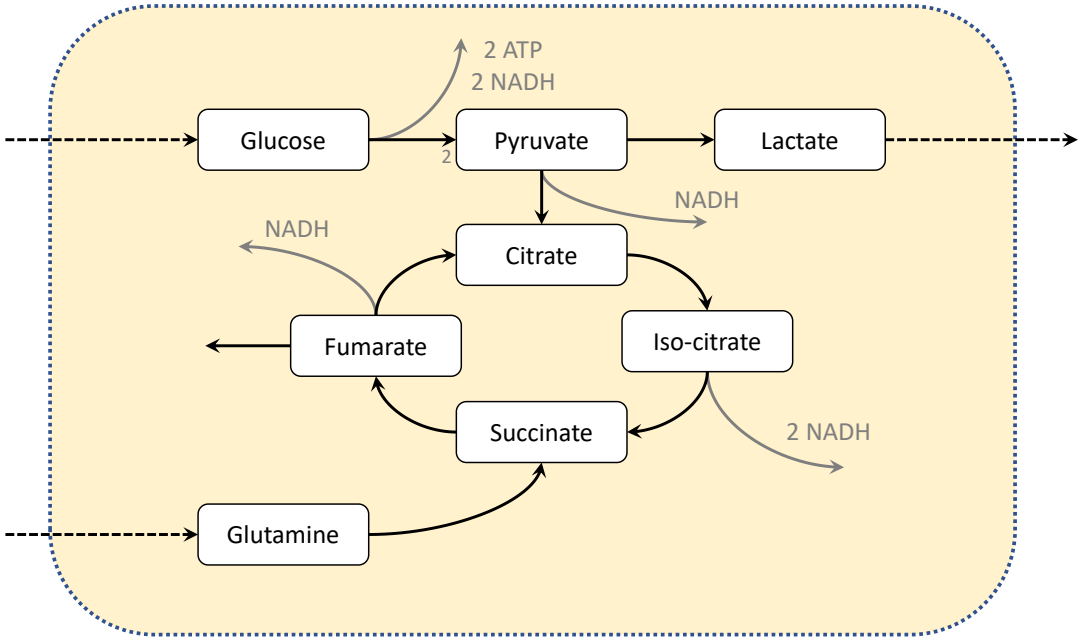

Figure 2.3. Conceptual model of intracellular metabolism

The molar balance for each intracellular metabolite is expressed by equation (2.1) for MSC cells. The net accumulation rate of each metabolite m is influenced by intracellular reactions and cross-membrane metabolic transport: the first term on the right-hand side (RHS) accounts for the contribution of

intracellular metabolic reactions (weighted by their respective stoichiometric coefficients), while the second RHS term accounts for metabolite transport across the cell membrane (only for glucose, lactate, and glutamine; the other metabolites do not cross the cell membrane as shown in Figure 2.3).

$$\frac{\partial M_m^{(MSC)}(t)}{\partial t} = \sum_{i=1}^{N_R} \left(STOIC_{m,i} \cdot RRate_i^{(MSC)}(t) \right) + \sum_{j=1}^{N_T} \left(STOIC_{m,j+N_R} \cdot \frac{TRate_j^{(MSC)}(t)}{V_{cell}} \right) \tag{2.1}$$

The impact of each intracellular ($RRate_i$) or cross-membrane ($TRate_i$) reaction is coded by the stoichiometric matrix, $STOIC$, which encodes the connection between intracellular metabolites and the enzymatic reactions they are involved in (the stoichiometric coefficient is negative for reactants and positive for products). The stoichiometric matrix is shown in equation (2.2). Each column corresponds to one of the reactions encompassed by the mathematical model: columns labelled R_1 through R_9 correspond to intracellular enzymatic reaction rates and are combined with the $RRate_i^{(TYP)}$ variable(s) from equations (2.1) and (2.3), and columns labeled T_1 through T_3 correspond to cross-membrane transport rates and are combined with the $TRate_i^{(TYP)}$ variables. The rows of the stoichiometric matrix correspond to metabolites and cofactors, whose names have been omitted from the equation to conserve horizontal space on the page, in the following order: glucose (row 1), pyruvate (row 2), lactate (row 3), citrate (row 4), iso-citrate (row 5), succinate (row 6), fumarate (row 7), glutamine (row 8), ATP (row 9) and NADH (row 10). ATP stands for adenosine triphosphate, and NADH stands for nicotinamide adenine dinucleotide (and hydrogen). An alternative approach may use yields to link metabolites to reaction rates instead of stoichiometric coefficients.

$$STOIC = \begin{pmatrix} R_1 & R_2 & R_3 & R_4 & R_5 & R_6 & R_7 & R_8 & R_9 & T_1 & T_2 & T_3 \\ -1 & 0 & 0 & 0 & 0 & 0 & 0 & 0 & 0 & +1 & 0 & 0 \\ +2 & -1 & 0 & -1 & 0 & 0 & 0 & 0 & 0 & 0 & 0 & 0 \\ 0 & +1 & 0 & 0 & 0 & 0 & 0 & 0 & 0 & 0 & -1 & 0 \\ 0 & 0 & 0 & +1 & -1 & 0 & 0 & +1 & 0 & 0 & 0 & 0 \\ 0 & 0 & 0 & 0 & +1 & -1 & 0 & 0 & 0 & 0 & 0 & 0 \\ 0 & 0 & +1 & 0 & 0 & +1 & -1 & 0 & 0 & 0 & 0 & 0 \\ 0 & 0 & 0 & 0 & 0 & 0 & +1 & -1 & -1 & 0 & 0 & 0 \\ 0 & 0 & -1 & 0 & 0 & 0 & 0 & 0 & 0 & 0 & 0 & +1 \\ +2 & 0 & 0 & 0 & 0 & 0 & 0 & 0 & 0 & 0 & 0 & 0 \\ +2 & 0 & 0 & +1 & 0 & +2 & 0 & +1 & 0 & 0 & 0 & 0 \end{pmatrix} \quad (2.2)$$

Equation (2.3) introduces the intracellular metabolite molar balance for PRE and OBC cells. It contains an additional RHS term, which accounts for differences in the (intracellular) metabolite levels between cells at neighboring differentiation states as the cells undergo differentiation. The necessity for this additional term arises from the fact that when cells differentiate (or change state, in the mathematical model) they do not instantaneously shift their intracellular metabolism and genetic activity to new levels but do so gradually while obeying the mass conservation law. *E.g.*, when cells differentiate from MSC to become members of the PRE state, they also diminish the measured average metabolic activity level for the PRE type because MSC metabolism is lower than that of PRE; the metabolic levels then recover, as the newly added cells adjust their behavior and match PRE characteristics.

$$\begin{aligned} \frac{\partial M_m^{(TYP)}(t)}{\partial t} = & \sum_{i=1}^{N_R} \left(STOIC_{m,i} \cdot RRate_i^{(TYP)}(t) \right) \\ & + \sum_{j=1}^{N_T} \left(STOIC_{m,j+N_R} \cdot \frac{TRate_j^{(TYP)}(t)}{V_{cell}} \right) \\ & + \frac{\int_{x_{min,G}}^{x_{max,G}} D_{out}^{(TYP-1)}(x,t)\, dx}{N_{total}^{(TYP)}} \cdot \left(M_m^{(TYP)}(t) - M_m^{(TYP-1)}(t) \right) \end{aligned} \quad (2.3)$$

When constructing the molar balance equation (2.3) in this way, the mathematical model accounts for the combined effect of adding both the volume of the new cells as well as their intracellular substance amounts to the existing population of cells of type (or differentiation state) “TYP”. The integral of $D_{out}(x,t)$

in the last RHS term corresponds to the instantaneous rate at which cells are differentiating into state TYP, while $N_{total}^{(TYP)}$ represents the total number of cells at differentiation state TYP, as given by equation (2.13). In this context, TYP can be seen as a numeric value, where MSC=1, PRE=2, and OBC=3. The last term of equation (2.3) might be easier to understand by analogy with the mass balance for a continuous stirred tank reactor (CSTR) model in which the integral of the $D_{out}(x,t)$ variable corresponds to the inlet flowrate of the CSTR, while $N_{total}^{(TYP)}$ corresponds to its volume. See chapter 2.1.5 for more information about the variable $D_{out}(x,t)$ and parameters $x_{min,G}$ and $x_{max,G}$.

Intracellular reaction rates are described by first-order kinetics, equation (2.4). Although Monod kinetics would provide more flexibility and precision to the mathematical model, they would also require additional parameters to be determined from (currently) insufficient experimental data.

$$RRate_i^{(TYP)}(t) = k_{cat,i} \cdot C_{R_i}(t) \tag{2.4}$$

Cross-membrane flowrates are described using equation (2.5), which corresponds to product-inhibited enzymatic transport and was obtained under the pseudo-steady state hypothesis for the transport enzyme concentration on the cell membrane, while allowing each differentiation state to manifest different transport enzyme levels, $k_{E,i}^{(TYP)}$, in the cell membrane.

$$TRate_i^{(TYP)}(t) = \frac{k_{E,i}^{(TYP)} \cdot C_{M_i,out}(t) \cdot k_{T,i}}{k_{T,i} + M_{T_i}^{(TYP)}(t)} \tag{2.5}$$

Transport of nutrients and waste products across the cell membrane also affects the culture medium of the cells (the effect is complementary to that of the intracellular compartment). Equation (2.6) illustrates the molar balance of extracellular metabolites in the culture medium. The equation pertains to the three metabolites that cross the cell membrane (m is either glucose, lactate, or glutamine); the index $j(m)$ on the right-hand side (RHS) of the equation depends on the metabolite being transported across the membrane: $j = 1$ for glucose, $j =$

2 for lactate, and $j = 3$ for glutamine. The negative sign in front of the RHS summation operator specifies the direction of metabolite transfer and is required because the entries of the $STOIC$ matrix are written using the intracellular compartment as reference (*i.e.*, any transport that increases the intracellular metabolite amount contributes to a decrease in the amount of the same metabolite in the culture medium).

$$\frac{d\left(V_R \cdot CC_m(t)\right)}{dt} = -\sum_{\forall\, TYP} \left(STOIC_{m,j(m)+N_R} \cdot TRate_{j(m)}^{(TYP)}(t) \cdot N_{total}^{(TYP)}(t) \right) \tag{2.6}$$

2.1.4. Balance equations for gene expression

Gene expression is time-dependent and differentiation-state specific. The first term on the right-hand side (RHS) of equation (2.7), ω_i, corresponds to the base expression of each gene (i) in the undifferentiated MSC state. The second term corresponds to RNA transcription rate activated by the binding of transcription activator $A_{Gi}^{(TYP)}$ to the promoter region of the expressed gene; (the level of) dexamethasone promotes the transcription of *Runx2*, which, in turn, promotes the expression of *osteonectin*. Reference values for RNA transcription rates in humans range between 1000 and 2400 nucleotides per minute [90]; due to the relative sizes of the two genes expressed in terms of number of nucleotides that encode them in the DNA [91,92], the values of the maximum transition rate are different for each of the two genes (parameter $k_{trans,i}$ from Table 2.1). The third term corresponds to the natural decay of intracellular mRNA modelled as a first-order rate; the value of the decay rate constant (k_{decay}) is calculated based on a median value of mRNA half-life of 9 hours [93].

$$\begin{aligned} \frac{\partial G_i^{(TYP)}(t)}{\partial t} = \omega_i + \frac{k_{trans,i} \cdot {A_{Gi}^{(TYP)}}^{n_{trans}}}{{A_{Gi}^{(TYP)}}^{n_{trans}} + {k_{DNA,i}}^{n_{trans}}} - k_{decay} \cdot G_i^{(TYP)}(t) \\ + \frac{\int_{x_{min,G}}^{x_{max,G}} D_{out}^{(TYP-1)}(x,t)\, dx}{N_{total}^{(TYP)}} \cdot \left(G_i^{(TYP)}(t) - G_i^{(TYP-1)}(t) \right) \end{aligned} \tag{2.7}$$

The last RHS term of equation (2.7) accounts for differences in gene expression levels between cells as they change their differentiation state; it is part

of the molar balance equation only for cells at states PRE and MSC; alternatively, its value is null for cells at differentiation state MSC. The integral of the differentiation rate, $D_{out}^{(TYP-1)}$, calculates the rate at which cells are differentiating between states (*i.e.*, between MSC and PRE, or between PRE and OBC); $N_{total}^{(TYP)}$ represents the total number of cells at differentiation state "TYP", as defined in equation (2.13). The intracellular metabolism section discusses this term of the balance equation more extensively.

Mesenchymal stem cells (MSCs) only express *osteonectin* at their basal level and will begin the differentiation process before increasing the relative expression of osteogenic genes. As the reduced model for gene expression shown in (2.7) does not include any parameters to capture this behavior, the value of the activator for the transcription of *osteonectin* is fixed at the initial value of the relative expression of *Runx2* to prevent the model from predicting an immediate increase in *osteonectin* expression: $A_{G,osteonectin}^{(MSC)} = G_{Runx2}^{(MSC)}(t = 0)$ instetad of $A_{G,osteonectin}^{(TYP)} = G_{Runx2}^{(TYP)}(t)$ used elsewhere.

The differentiation agent that activates the expression of *Runx2* (dexamethasone) is also modelled, using two molar balance equations (one for each compartment: intracellular and extracellular). The cross-membrane transport rate of dexamethasone is modelled using the linear transport rate equation (2.8). The membrane permeability $\lambda_{membrane}$ acts as a partial mass transfer coefficient for dexamethasone. The molar balance for the extracellular compartment aggregates the transport rates from all the cells in the culture medium, as shown in equation (2.9).

$$\frac{d}{dt}\left(V_{cell} \cdot Dex_{cell}(t)\right) = \lambda_{membrane} \cdot \left(Dex_{culture}(t) - Dex_{cell}(t)\right) \tag{2.8}$$

$$\frac{d}{dt}\left(V_R \cdot Dex_{culture}(t)\right) = \lambda_{membrane} \cdot \left(Dex_{cell}(t) - Dex_{culture}(t)\right) \cdot \sum_{TYP} N_{total}^{(TYP)}(t) \tag{2.9}$$

2.1.5. Population balance equations for the cellular division cycle and cell differentiation

The cell division cycle is described in terms of its main phases: Gap 0 (G0) and Gap 1 (G1) are lumped into a single phase (phase “G”), DNA synthesis is modelled as a single growth stage (phase “S”), and Gap 2 (G2) and mitosis are also lumped (phase “M”). Phases G0 and G1 were lumped because of the experimental difficulty in distinguishing between them, while phases G2 and mitosis were lumped due to the relatively short duration of mitosis compared to G2 and practicality in managing the complexity of the mathematical model wherever possible. The order of progression through the growth phases used in the mathematical model, G–S–M (Figure 2.2 and Figure 2.4), is a mirror image of the biological succession (gap 1, synthesis, gap 2, and mitosis) [94].

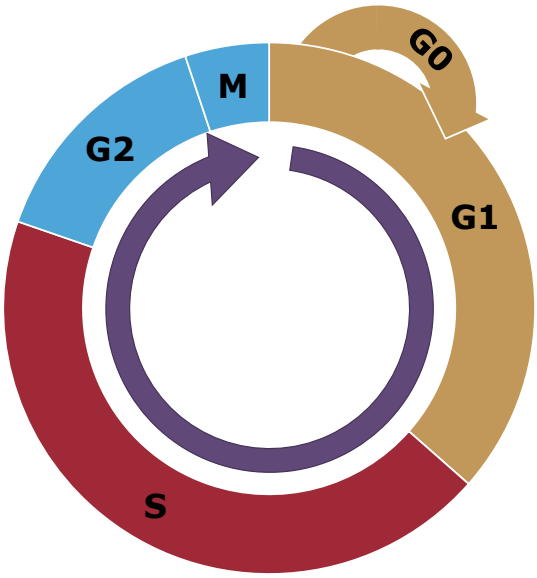

Figure 2.4. Cellular division cycle and its component phases, as represented in the mathematical model

The independent variables are the growth coordinate (x) and time (t). The cells enter each cellular-division-cycle phase at the lowest growth coordinate for that phase (*i.e.*, $x_{min,G}$, $x_{min,S}$, and $x_{min,M}$). As cells traverse each cell cycle phase, the growth coordinate increases, up to the point when they transition to the next phase of the cell cycle. Even though the growth coordinate corresponds to different biochemical components in each cell cycle phase (cyclin E for phase G, DNA content for phase S, and cyclin B for phase M [94]), the mathematical

model uses a singular distribution domain (x) to represent the growth coordinate regardless of cell cycle phase, as the objective of the model is to capture the growth cycle phase traversal behavior (which is conceptually the same for all phases) and ignore the details of the specific cyclins of each phase. Each cell cycle phase functions in the same way for all three differentiation states included in the mathematical model (MSC, PRE, and OBC) since cell cycle phases are not specific to just one cell type and are universally valid for the eukaryote class [94].

Equation (2.10) applies to phase G, while it is traversed by cells undergoing division. Terms on the left-hand side of the equation represent, in order: the temporal derivative of the cell count distribution, progression rate in traversing the current growth phase, death rate, and transition rate. The right-hand side of the equation includes the boundary condition, as well as differentiation rates (cells that become the current type are treated as inflow, while cells that are differentiating further are regarded as outflow). The RHS boundary condition ensures that cells start phase G from the beginning; mathematically, all incoming cells, $T_{G,in}^{(TYP)}(t)$, are added to the cell cycle phase at the lowest phase coordinate, $x_{min,G}$, which is the only value of the (first) argument x at which the Kronecker delta function (δ_K) is equal to 1; δ_K has the value 0 for all other values of x and the inflow $T_{G,in}^{(TYP)}(t)$ does not contribute to the equation. The independent variable x corresponds to the intracellular amount of cyclin E (protein), expressed as a percentage in terms of the highest experimentally determined value, ranging between 0 and 100.

$$\begin{aligned}\frac{\partial N_G^{(TYP)}(x,t)}{\partial t} + \frac{\partial\left[\mu_G^{(TYP)}(x,t)\cdot N_G^{(TYP)}(x,t)\right]}{\partial x} + \theta_G^{(TYP)}(x,t)\cdot N_G^{(TYP)}(x,t) \\ + T_{G,out}^{(TYP)}(x,t)\cdot N_G^{(TYP)}(x,t) \\ = \delta_K\left(x, x_{min,G}\right)\cdot T_{G,in}^{(TYP)}(t) + D_{out}^{(TYP-1)}(x,t) - D_{out}^{(TYP)}(x,t)\end{aligned} \tag{2.10}$$

The equation for the DNA synthesis phase (labeled “S”) follows a similar approach to phase G, keeping only the relevant terms: time derivative of the cell count distribution, phase progression rate, death rate, and the boundary condition (on the RHS). Since the main objective of the cell during phase S is DNA code

duplication [94], neither transition nor differentiation are part of equation (2.11). The independent variable x corresponds to the count of intracellular DNA content and ranges between 1 (copy of DNA) and 2 (copies of DNA code).

$$\frac{\partial N_S^{(TYP)}(x,t)}{\partial t} + \frac{\partial\left[\mu_S^{(TYP)}(x,t) \cdot N_S^{(TYP)}(x,t)\right]}{\partial x} + \theta_S^{(TYP)}(x,t) \cdot N_S^{(TYP)}(x,t) = \delta_K\left(x, x_{min,S}\right) \cdot T_{S,in}^{(TYP)}(t) \tag{2.11}$$

The final phase of the cell division cycle, phase M, has an almost identical behavior with that of phase G, except for cellular differentiation, which does not occur during mitosis, considering that the main objective of the cell during phase M is the preparation for and execution of cellular division. Phase M includes terms for the time derivative of the cell count distribution, phase traversal rate, death rate, transition rate, and RHS boundary condition, as shown in equation (2.12). The independent variable x corresponds to the intracellular amount of cyclin B (protein), expressed as a percentage in terms of the highest experimentally determined value, ranging between 20 and 100; the lowest value ($x_{min,M}$) is not zero because cells start to produce cyclin B even before completing the synthesis phase.

$$\frac{\partial N_M^{(TYP)}(x,t)}{\partial t} + \frac{\partial\left[\mu_M^{(TYP)}(x,t) \cdot N_M^{(TYP)}(x,t)\right]}{\partial x} + \theta_M^{(TYP)}(x,t) \cdot N_M^{(TYP)}(x,t) + T_{M,out}^{(TYP)}(x,t) \cdot N_M^{(TYP)}(x,t) = \delta_K\left(x, x_{min,M}\right) \cdot T_{M,in}^{(TYP)}(t) \tag{2.12}$$

The total cell count of cells at each differentiation state TYP is obtained by summing up the cell counts for each growth phase (only from cells that also have the corresponding differentiation state), as shown in equation (2.13).

$$N_{total}^{(TYP)}(t) = \int_{x_{min,G}}^{x_{max,G}} N_G^{(TYP)}(x,t)\, dx + \int_{x_{min,S}}^{x_{max,S}} N_S^{(TYP)}(x,t)\, dx + \int_{x_{min,M}}^{x_{max,M}} N_M^{(TYP)}(x,t)\, dx \tag{2.13}$$

The duration of phase G is correlated (separately for each differentiation state, TYP) with the production rate of energy cofactors, as per equation (2.14). The production rate of each cofactor (given as the partial temporal derivative) is calculated as per equation (2.1); although they are distinct model entities, the parameters that connect cofactor production to phase G duration are correlated $E_{NADH}^{(TYP)} = 2.5 \cdot E_{ATP}^{(TYP)}$, given that NADH is processed *via* the electron transport chain to produce more ATP [95]. Equation (2.14) was derived considering that a fixed percentage of the energy cofactors generated by the cells are used for cell cycle traversal, for each cell type (TYP). Instead of connecting the energy cofactors with the traversal rate of phase G — variable $\mu_G^{(TYP)}(x,t)$ from equation (2.10) — which partially depends on the choice for the bounds of the phase coordinate domain ($x_{min,G}$ and $x_{max,G}$), energy cofactors were connected with the duration variable, which is independent of the bounds of the phase coordinate domain and its biological significance is easier to grasp. The relationship between the duration of a phase and its traversal rate is given by equation (2.31).

$$duration_G^{(TYP)}(t) = \frac{1}{E_{ATP}^{(TYP)} \cdot \frac{\partial M_{ATP}^{(TYP)}(t)}{\partial t} + E_{NADH}^{(TYP)} \cdot \frac{\partial M_{NADH}^{(TYP)}(t)}{\partial t}} \tag{2.14}$$

Transition rates between growth phases, which are used in the boundary conditions of equations (2.10), (2.11), and (2.12), ensure cell cycle progression by transferring cells from each growth cycle phase to the following one. Equation (2.15) gives the transition rate into phase G: the total rate is aggregated from the phase-coordinate-distributed transition rate from phase M; the number 2 multiplying the integral on the right-hand side accounts for cellular division / duplication during mitosis.

$$T_{G,in}^{(TYP)}(t) = 2 \cdot \int_{x_{min,M}}^{x_{max,M}} T_{M,out}^{(TYP)}(x,t) \cdot N_M^{(TYP)}(x,t)\, dx \tag{2.15}$$

Equation (2.16) shows the transition rate into the DNA synthesis phase (labeled “S”) as the aggregated phase-coordinate-distributed transition rate from phase G.

$$T_{S,in}^{(TYP)}(t) = \int_{x_{min,G}}^{x_{max,G}} T_{G,out}^{(TYP)}(x,t) \cdot N_G^{(TYP)}(x,t)\, dx \tag{2.16}$$

Equation (2.17) presents the transition rate from phase S into phase M. Phase transition is not distributed in this case, because of the requirement that DNA must be properly duplicated before progressing; furthermore, once the DNA content has been copied, the synthesis phase ends, and transition occurs at a single point rather than as a distribution around a mean value.

$$T_{M,in}^{(TYP)}(t) = \mu_S^{(TYP)}(x,t) \cdot N_S^{(TYP)}\left(x_{max,S}, t\right) \tag{2.17}$$

The cell cycle transition rate for phase M follows equation (2.18): cells shift to the subsequent phase (G) in the division cycle around a threshold value of the phase coordinate; this behavior is modeled by means of the normal probability distribution for the transition rate, with phase-specific values for the mean and variance parameters.

$$T_{M,out}^{(TYP)}(x,t) = \frac{\mu_M^{(TYP)}(x,t) \cdot \frac{dP_M(x)}{dx}}{1 - P_M(x)} \tag{2.18}$$

The cell cycle transition rate for phase G is modeled by a more complicated formulation (2.19), which encompasses the possibility for cells to leave phase G either by transitioning to phase S or by differentiating (into type $TYP + 1$). Note that when no differentiation occurs (and the differentiation fraction $f_{diff}^{(TYP)}$ is null) equation (2.19) can be reduced to expression used for phase M given by equation (2.18); when no transition occurs (at unit differentiation fraction), the expression for the transition rate evaluates to zero.

$$T_{G,out}^{(TYP)}(x,t) = \frac{\mu_G^{(TYP)}(x,t) \cdot \left(1 - f_{diff}^{(TYP)}\right) \cdot \frac{dP_G(x)}{dx}}{1 - f_{diff}^{(TYP)} \cdot CPD_G(x) - \left(1 - f_{diff}^{(TYP)}\right) \cdot P_G(x)} \tag{2.19}$$

Cells in phase G also undergo differentiation, at a rate given by equation (2.20). Note that when no differentiation occurs, the expression evaluates to zero, and reaches its maximum value for unit differentiation fraction, $f_{diff}^{(TYP)}$.

$$D_{out}^{(TYP)}(x,t) = \frac{\mu_G^{(TYP)} \cdot f_{diff}^{(TYP)} \cdot \frac{dCPD_G(x)}{dx} \cdot N_G^{(TYP)}(x,t)}{1 - f_{diff}^{(TYP)} \cdot CPD_G(x) - \left(1 - f_{diff}^{(TYP)}\right) \cdot P_G(x)} \tag{2.20}$$

The equations for cell cycle phase transition rates employ the use of phase-coordinate-dependent transition probability functions: $P_G(x)$ for transition from phase G to phase S, and $P_M(x)$ for transition between phase M and phase G. Both functions are defined in terms of the normal cumulative probability function (2.21). Equation (2.22) expresses the cumulative probability of transition for cells traversing phase G, while equation (2.23) conveys the transition probability for phase M.

$$P_{norm}(x,\mu,\sigma) = \frac{\int_{-\infty}^{x} \exp\left(-\frac{1}{2} \cdot \left(\frac{q-\mu}{\sigma}\right)^2\right) dq}{\sigma \cdot \sqrt{2 \cdot \pi}} \tag{2.21}$$

$$P_G(x) = P_{norm}\left(x, x_{threshold,G}, \sigma_G\right) \tag{2.22}$$

$$P_M(x) = P_{norm}\left(x, x_{threshold,M}, \sigma_M\right) \tag{2.23}$$

An additional function is employed to describe the cumulative probability of differentiation during the traversal of phase G by the cells; this function also depends on the phase coordinate and is defined by equation (2.24). The name of this function, CPD, stands for cumulative probability of differentiation.

$$CPD_G(x) = \frac{\int_{x_{min,G}}^{x} 1 - P_G(q)\, dq}{\int_{x_{min,G}}^{x_{max,G}} 1 - P_G(q)\, dq} \tag{2.24}$$

The cumulative probability functions defined by equations (2.22), (2.23) and (2.24) convey the probability of the associated event — transition in the case of P_G and P_M, and differentiation in the case of CPD_G — to have already occurred

at or before the value x of the phase coordinate argument, for each individual cell. At the population level, the same functions carry the meaning of fraction of the cells that leave the cell cycle phase they are currently traversing (either through transition or differentiation) at or before the phase coordinate position specified by the argument x.

The differentiation fraction depends on the relative expression level of the key gene for each cellular differentiation state (2.25). The differentiation fraction of mesenchymal stem cells into pre-osteoblasts (TYP=MSC) is given by the level of the key gene *Runx2* in MSCs, and the differentiation fraction of pre-osteoblasts into osteoblasts (TYP=PRE) is given by the level of *osteonectin* in PRE cells. Osteoblasts do not further differentiate; therefore, their differentiation fraction is zero (2.26).

$$f_{diff}^{(TYP)} = \frac{{G_{key}^{(TYP)}}^{dxp}}{{k_{diff}^{(TYP)}}^{dxp} + {G_{key}^{(TYP)}}^{dxp}} \tag{2.25}$$

$$f_{diff}^{(OBC)} = 0 \tag{2.26}$$

2.1.6. Building the transition function

When using a population balance model, its most important and intricate component is the transition function, which enables the representation of distributed phase-to-phase transition (around a reference or average value), the alternative being transition at a single point, such as in the case of the DNA synthesis phase. Although equations (2.18) and (2.19) have been customized to utilize the (cumulative) normal probability distribution, the methodology presented in this chapter is applicable to any probability distribution.

To arrive at the correct form of the transition function, $T_{\pi,out}(x)$, in terms of the cell cycle phase transition probability, a target scenario having a known population distribution was conceived: at constant inflow (transition) of cells into the current phase, and no cell death, the steady state cell distribution profile should be proportional to the complementary cumulative distribution function (for the probability of transition to the next cell cycle phase) — in other words, the cell

distribution is proportional to the fraction of cells that have not transitioned yet, at every point along the growth coordinate x, as stated by equation (2.27), where $N(x)$ is the steady state cell distribution and $P(x)$ is the cumulative probability of transition as particularized by equation (2.22) or (2.23).

$$N(x) = N(x = x_{min}) \cdot \big(1 - P(x)\big) \tag{2.27}$$

Replacing equation (2.27) in the population balance equation (2.12) and applying the assumptions above, equation (2.28) is obtained. Traversal rate, μ, is obtained by taking a partial derivative of the growth coordinate with respect to time; therefore, replacing the right-hand-side of equation (2.27) in (2.28) leads to equations (2.29); further rearrangement leads to an equivalent form of equation (2.18), which is applicable for modeling transition from phase M.

$$\frac{\partial(\mu \cdot N)}{\partial x} + T_{out} \cdot N = 0 \tag{2.28}$$

$$\mu \cdot \frac{d\big[N(x = x_{min}) \cdot \big(1 - P(x)\big)\big]}{dx} + T_{out} \cdot N(x = x_{min}) \cdot \big(1 - P(x)\big) = 0 \tag{2.29}$$

Deriving the form of the transition function for phase G follows a similar process, with some key differences: the cumulative probability appearing in equation (2.27) carries the meaning of cumulative probability for each cell to leave the current cell cycle phase, whether that happens as a transition to phase S or differentiation into the following cell type as defined by equation (2.30). When recovering the transition function from the equation, the partial derivative in the numerator of equation (2.19) only keeps the contribution of transition, whereas in equation (2.20) only the contribution of differentiation is kept in the numerator.

$$P_{event,G}^{(TYP)}(x) = f_{diff}^{(TYP)} \cdot CPD_G(x) - \Big(1 - f_{diff}^{(TYP)}\Big) \cdot P_G(x) \tag{2.30}$$

This formulation, together with the connection between the growth rate $\mu_{\pi}^{(TYP)}$ and the duration of each phase, shown in equation (2.31), has the advantage of allowing the modeler to set either the duration of the cell cycle

phase or its growth rate. Additionally, this mathematical formulation of the transition function (and differentiation rate) correctly reproduces observed doubling times for cell populations if compared with experimental measurements of steady population growth.

$$duration_{\pi}^{(TYP)} \cdot \mu_{\pi}^{(TYP)} = x_{max,\pi} - x_{min,\pi} \quad (2.31)$$

2.2. Simulation results

This chapter contains the values for the parameters of the mathematical model and three sections for the main results of the model: a sensitivity analysis to identify the most significant parameters of the model, followed by an uncertainty analysis regarding the connection between the rate of intracellular energy cofactor production and the duration of phase G, and a simulation of the base experimental scenario showing that the predictions of the model are accurate and match the available experimental data.

The computer implementation of the mathematical model uses discretized versions of the equations that involve distributed variables. For accurate calculations, the growth coordinate for phases G and M are each discretized into 100 bins, while the growth coordinate of phase S is discretized into only 50 bins (due to its simpler form, compared to that of the other two phases). The number of bins per phase was chosen (in increments of 20 for phases G and M, and steps of 10 for phase S) to match the cell counts that would be observed under steady growth conditions, keeping the relative error under 1% after 5 complete cell cycles.

The level of intracellular and extracellular metabolites, and relative gene expression variables are all vector-valued variables and require no discretization (since they already are discrete values). The model was coded and simulated using the gPROMS modelling environment [96] and is comprised of 743 algebraic and 785 differential equations. The base case takes about 12 seconds to run on a computer with a 4.20GHz Intel® Core™ i7-7700K CPU and 16 GB of RAM. Values for the parameters of the mathematical model are given in Table 2.1.

2.2.1. Parameter estimation

All model parameters shown in Table 2.1 were estimated to fit the experimental data that is shown together with the prediction of the mathematical model in Figure 2.7, Figure 2.8, and Figure 2.10. As a first step, model parameters were estimated in groups, by means of least squares non-linear regression; parameters involved in gene expression were estimated first, followed by metabolism-related parameters; cell cycle parameters related to proliferation and differentiation were estimated last. Then, the most important parameters of the model, which were identified using global sensitivity analysis (chapter 2.2.2), were subjected to a second parameter estimation using the maximum likelihood objective function, as provided by the gPROMS modeling environment; in addition, the confidence intervals were estimated for these parameters are presented in Appendix A.

Table 2.1. Nominal values of model parameters for the process of osteogenic differentiation in well-plate cultures

Parameter	Value	Units	Parameter	Value	Units
$k_{cat,1}$	21.27	day^{-1}	$k_{E,2}^{(PRE)}$	$2 \cdot 10^{-10}$	$L \cdot day^{-1}$
$k_{cat,2}$	22.66	day^{-1}	$k_{E,3}^{(PRE)}$	$4.94 \cdot 10^{-15}$	$L \cdot day^{-1}$
$k_{cat,3}$	2.09	day^{-1}	$k_{E,1}^{(OBC)}$	$1.25 \cdot 10^{-18}$	$L \cdot day^{-1}$
$k_{cat,4}$	19.42	day^{-1}	$k_{E,2}^{(OBC)}$	$2 \cdot 10^{-10}$	$L \cdot day^{-1}$
$k_{cat,5}$	563.43	day^{-1}	$k_{E,3}^{(OBC)}$	$1.59 \cdot 10^{-17}$	$L \cdot day^{-1}$
$k_{cat,6}$	1081.33	day^{-1}	$k_{T,1}$	1000	$pmol \cdot L^{-1}$
$k_{cat,7}$	1334.65	day^{-1}	$k_{T,3}$	1000	$pmol \cdot L^{-1}$
$k_{cat,8}$	1541.34	day^{-1}	$k_{trans,Runx2}$	42.2497	day^{-1}
$k_{cat,9}$	446.09	day^{-1}	$k_{trans,osteonectin}$	600	day^{-1}
k_{decay}	1.85	day^{-1}	$k_{diff}^{(MSC)}$	0.19	
$k_{DNA,Runx2}$	117.0355		$k_{diff}^{(MSC)}$	35	
$k_{DNA,osteonectin}$	0.3953		$E_{ATP}^{(MSC)}$	400	L/pmol
$k_{E,1}^{(MSC)}$	$5.25 \cdot 10^{-18}$	$L \cdot day^{-1}$	$E_{ATP}^{(PRE)}$	80	L/pmol
$k_{E,2}^{(MSC)}$	$2 \cdot 10^{-10}$	$L \cdot day^{-1}$	$\lambda_{membrane}$	$1.5 \cdot 10^{-12}$	day^{-1}
$k_{E,3}^{(MSC)}$	$1.47 \cdot 10^{-18}$	$L \cdot day^{-1}$	ω_{Runx2}	0.2775	day^{-1}
$k_{E,1}^{(PRE)}$	$8.42 \cdot 10^{-17}$	$L \cdot day^{-1}$	$\omega_{osteonectin}$	46.2497	day^{-1}

Table 2.2 shows the parameters of the model that are fixed throughout the simulation and are not subject to global sensitivity analysis (and their nominal values).

Table 2.2. Parameters that are fixed throughout the simulation and are not subject to global sensitivity analysis

Parameter	Value	Units	Parameter	Value	Units
$x_{min,G}$	0		$x_{max,G}$	100	
$x_{min,S}$	1		$x_{max,S}$	2	
$x_{min,M}$	20		$x_{max,M}$	100	
$x_{threshold,G}$	70		$x_{threshold,M}$	76	
n_{trans}	15		dxp	20	
V_{cell}	$3.5 \cdot 10^{-12}$	L	$\theta_{\pi}^{(TYP)}$	$2 \cdot 10^{-5}$	day^{-1}
V_R	55	mL	$k_{T,2}$	1000	pmol/L
			$E_{ATP}^{(OBC)}$	3	L/pmol

2.2.2. Global sensitivity analysis

Global sensitivity analysis (GSA) was performed on the computer implementation of the mathematical model to identify the parameters (if any) that significantly influence the output of the model due to uncertainty in their nominal values. The analysis involves 2 responses (model outputs) and 32 factors (model parameters). The uncertainty interval for each GSA factor ranges between 50% and 150% of the nominal value of the corresponding parameter. The sets of parameter values used for the analysis were produced using the Sobol sequence [81], as implemented by the MATLAB function `sobolset` [82]. Next, simulation data were gathered by means of repeated gPROMS [96] simulations, with one simulation per set of values sampled form the parameter space. The model outputs subjected to the analysis are the total number of cells (of all types) and the (total) number of osteoblasts, sampled at 3.5-day intervals (every half-week) for the first three weeks of the differentiation process: 6 values for each response variable, for a total of 12 outputs. The sensitivity indices for all 12 responses were computed using the random sampling high-dimensional model representation (RS-HDMR) software package [79].

The factors (parameters) with the highest sensitivity index values are listed in Table 2.3; while each factor has 6 associated sensitivity index values (one per time point), the table lists only the largest one. These parameters are either related to cellular differentiation via gene expression, or to cell proliferation via intracellular metabolism. Gene expression is significantly impacted by parameters such as mRNA decay rate (k_{decay}), DNA binding constants ($k_{DNA,Runx2}$ and $k_{DNA,osteonectin}$), base expression rate of *Runx2* in MSCs (ω_{Runx2}),

and gene-level threshold for cellular differentiation ($k_{diff}^{(MSC)}$ and $k_{diff}^{(PRE)}$). The strongest influence on intracellular metabolism is held by parameters such as glucose uptake rate by MSC ($E_{ATP}^{(MSC)}$) and PRE ($E_{ATP}^{(PRE)}$) cells, and reaction rate constant for the enzymatic transformation of pyruvate into lactate ($k_{cat,2}$). Figure 2.5 synthesizes the results of the GSA.

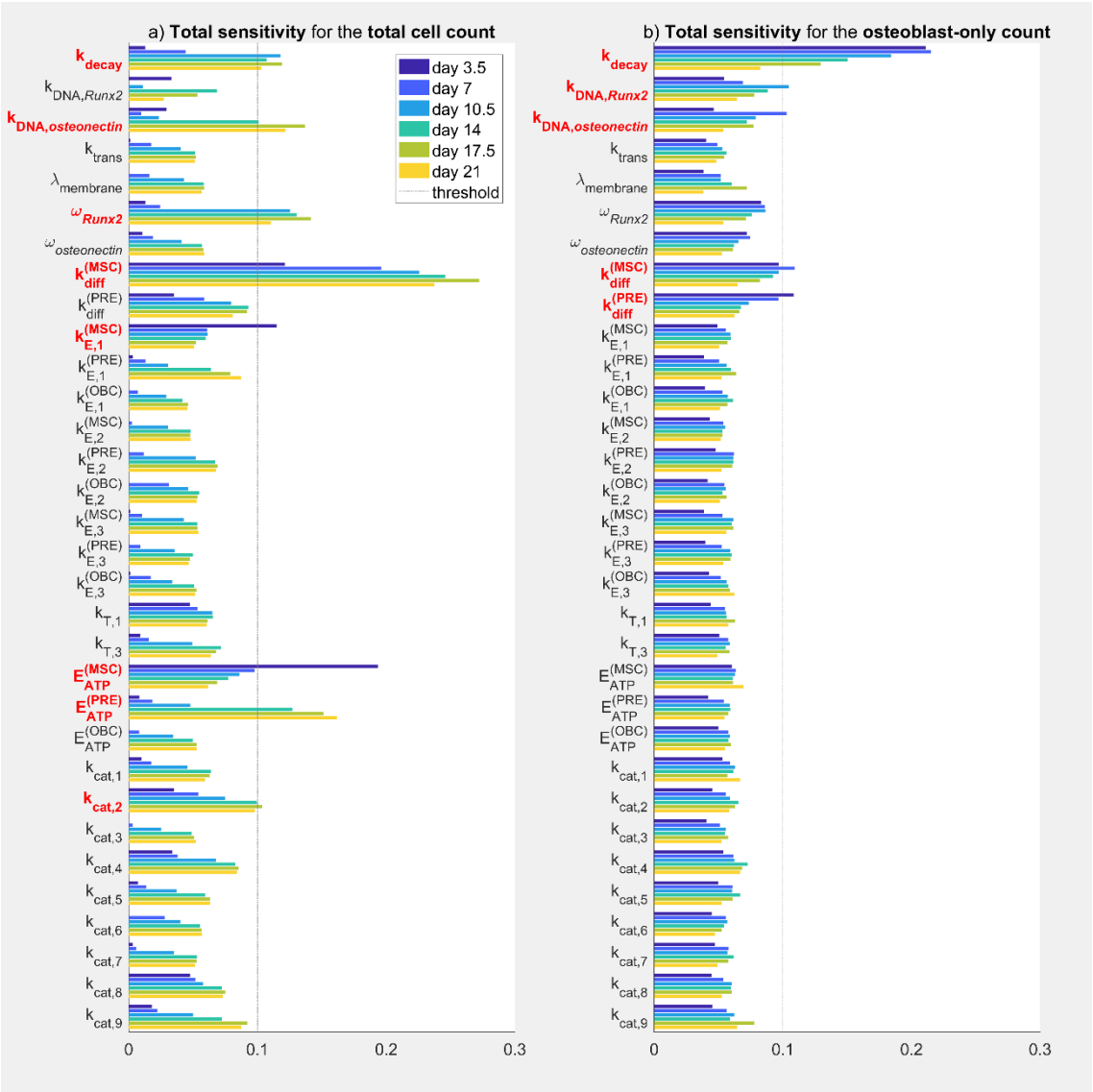

Figure 2.5. Global sensitivity analysis results.
Parameters with total sensitivity indices larger that the threshold (> 0.1, dashed line) are indicated in bold red font and are deemed significant for the respective model output (a: total cell count, or b: osteoblast-only count) [85]

Table 2.3. Significant parameters of the mathematical model, as identified using global sensitivity analysis; values below the threshold (0.1) are grayed out and values above 150% of the threshold are written in bold text

Factor, i	Total sensitivity index, TSI_i	
	Output 1: total cell count	Output 2: osteoblast count
k_{decay}	0.119	**0.215**
$k_{DNA,Runx2}$	0.069	0.105
$k_{DNA,osteonectin}$	0.137	0.103
ω_{Runx2}	0.142	0.087
$k_{diff}^{(MSC)}$	**0.272**	0.109
$k_{diff}^{(PRE)}$	0.093	0.108
$k_{E,1}^{(MSC)}$	0.115	0.060
$E_{ATP}^{(MSC)}$	**0.194**	0.069
$E_{ATP}^{(PRE)}$	**0.162**	0.059
$k_{cat,2}$	0.104	0.066

Sensitivity index values plotted in Figure 2.5 are the final values calculated by the analysis, and are based on 1,729,172 evaluations of the model, each using different sets of values for the 32 parameters. Convergence plots for the global sensitivity analysis are presented in Appendix B.

2.2.3. Effects of cell cycle duration of the metabolism and differentiation of UCB MSCs

The mathematical model was used to assess the effect of cell cycle duration on the temporal profiles of key variables, such as the average concentration of intracellular metabolites (for each cell type) and the levels of relative gene expression of the total cell population. This analysis was performed *in silico*, using the mathematical model presented in this chapter, whose prediction is compared to experimental data in chapter 2.2.4. The values for the two varied parameters range between (approximately) 0.1 and 10 times their nominal value: $E_{ATP}^{(MSC)}$ ranged between 40 and 4000, and $E_{ATP}^{(PRE)}$ ranged between 8 and 800. 51 logarithmically distributed values were used for each of the parameters, for a total of 2601 simulations.

Similar qualitative behavior is observed for all metabolites covered by the mathematical model (Figure 2.6a-h). A faster cellular division cycle traversal rate for mesenchymal stem cells (higher value of the $E_{ATP}^{(MSC)}$ model parameter), delays

the intracellular metabolic activity shift corresponding to the differentiation of MSCs into PREs (see Figure 2.6), and the delay is more pronounced when pre-osteoblasts have a low growth rate (low $E_{ATP}^{(PRE)}$, corresponding to a higher Gap 0/Gap 1 phase duration). Specifically, when using the nominal value of $E_{ATP}^{(MSC)}$, differentiation is delayed by approximately two days (from day 8 to day 10) if $E_{ATP}^{(PRE)}$ is below its nominal value. For higher values of $E_{ATP}^{(MSC)}$ (and low $E_{ATP}^{(PRE)}$), the onset of differentiation is further delayed until about day 12.

While all metabolite concentrations exhibit a similar fluctuation pattern (response) within the examined time frame, the importance of glycolytic activity is different from that of the TCA cycle throughout the differentiation process, with the TCA cycle accounting for roughly 87% of the total amount of energy produced by the cells during the 21-day differentiation process, and glycolysis accounting for the remaining 13%.

Cell cycle dynamics do not affect the onset of *Runx2* expression, which always occurs between days 6 and 7 (not shown in Figure 2.6). Interestingly, an increase in growth rates (or a decrease of cell cycle duration) for either MSCs or pre-osteoblasts leads to a delay in the expression of *osteonectin* (Figure 2.6i), suggesting the existence of an inherent tradeoff between proliferation and differentiation. Although this tradeoff can be explained by the limited availability of energy resources in the cell (allowing either one or the other to occur), the analysis presented in this chapter (Figure 2.6) shows that the tradeoff exists even when the two behaviors do not compete for the energy resources of the cell.

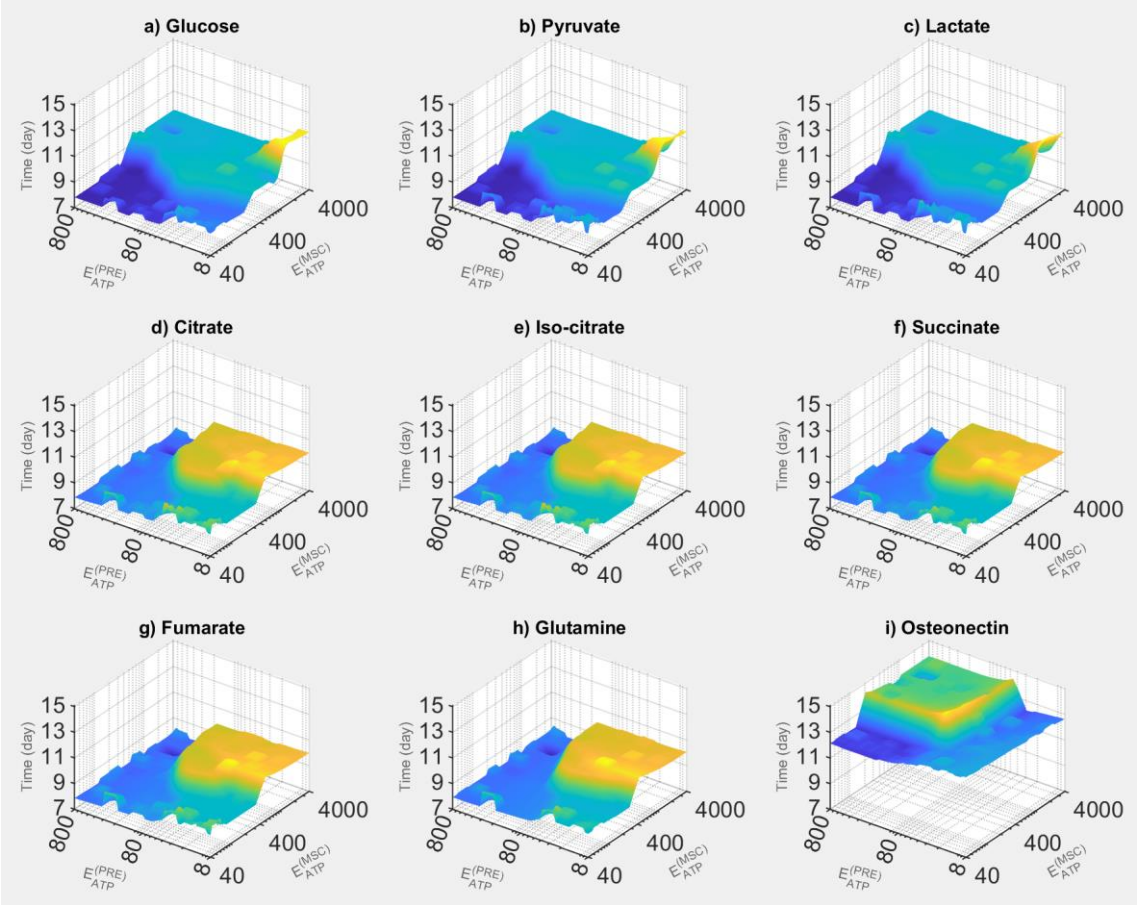

Figure 2.6. Impact of cell growth parameters of mesenchymal stem cells ($E_{ATP}^{(MSC)}$, on the x-axis) and pre-osteoblasts ($E_{ATP}^{(PRE)}$, on the y-axis) on the differentiation onset time (z-axis), expressed as the time point at which differentiation-specific changes occur for the examined variables (*i.e.*, average intracellular metabolite concentrations and relative gene expression levels): a) glucose, b) pyruvate, c) lactate, d) citrate, e) iso-citrate, f) succinate, g) fumarate, h) glutamine, and i) *osteonectin*. [85]

2.2.4. Population balance modeling incorporating metabolism and genetic switches, deconvoluted heterogeneity of differentiating populations

The proposed mathematical model — encompassing equations (2.1)-(2.6) for metabolism, (2.7)-(2.9) for gene expression, and (2.10)-(2.26) for cell proliferation and differentiation — accurately captures the experimental measurements for the activity of glycolysis, TCA cycle and glutaminolysis throughout the entire differentiation process. *In-silico* simulation results indicate that intracellular levels of all described metabolites follow a similar trend from day 0 to day 21 of differentiation (Figure 2.7). Starting at a basal level between day 0 and day 5, the model shows a sharp concentration increase for all metabolites (solid black lines), reaching a maximum value around day 11, before

decreasing steadily until day 21. These results replicate the general trend observed in the experimental data (diamond symbols with vertical error bars), showing a global increase in the activity of glycolysis, TCA cycle and glutaminolysis between day 6 and day 11, followed by reduced activity of the same pathways at the final stages of differentiation.

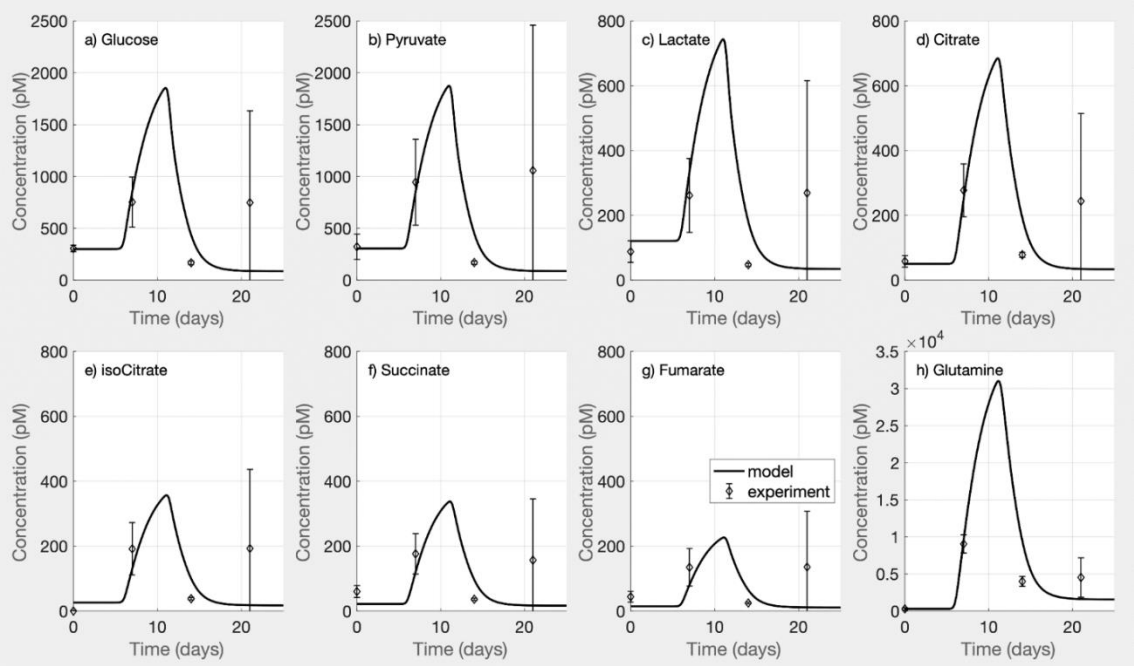

Figure 2.7. Average intracellular metabolite concentrations during the osteogenic differentiation process of mesenchymal stem cells: a) glucose, b) pyruvate, c) lactate, d) citrate, e) iso-citrate, f) succinate, g) fumarate, and h) glutamine. Comparison between the experimental values (diamond symbols with vertical error bars) and the prediction of the mathematical model (solid black lines) [85]

The concentration levels at day 21 were not attributed to a distinct phenotype because of their high variance (the difference between measurements at day 7 and day 21 is not statistically significant), which could be the result of contamination or some irregularity in the experimental protocol. Furthermore, the differences between the metabolic phenotypes of the cells at day 14 and day 21 are small [44], indicating that osteoblasts (OBC) are the terminal phenotype when using the given experimental protocol. Experimental data for gene expression also support the claim that the cell populations at day 14 and day 21 are related, but have different characteristics compared with day 7 populations; experimental measurements and their statistical significance are presented in Appendix C.

When the parameters of the mathematical model were calibrated based on experimental data, equal importance was assigned to all timepoints. The initial condition for intracellular metabolism sets the corresponding concentration variables to their steady state values (for mesenchymal stem cells), which are visibly different from their experimental counterparts at day 0 for some of the metabolites (Figure 2.7). This outcome is expected and reasonable, as parameter values estimated using regression techniques result in the model prediction fitting some of the experimental datapoints better than others, including those at day 0. The same discrepancy between experimental and predicted values at day 0 occurs for gene expression (Figure 2.8).

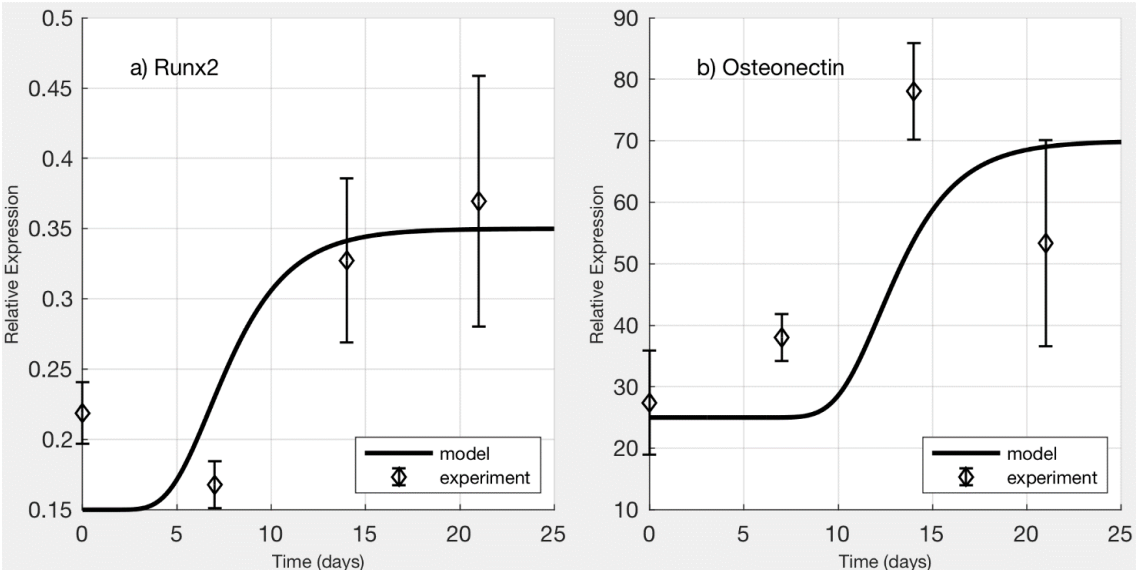

Figure 2.8. Average gene expression levels during the osteogenic differentiation process of mesenchymal stem cells: a) Runx2, and b) osteonectin. Comparison between experimental data (black diamond symbols with vertical error bars) and the prediction of the mathematical model (solid black lines) [85]

The mRNA levels of *Runx2* and *osteonectin* are used to define early and late osteogenic differentiation (respectively), and, subsequently, the mesenchymal stem, pre-osteoblast, and osteoblast stages (Figure 2.8). Activation patterns are successfully captured for both genes, showing that *Runx2* levels increase early during the differentiation period (beginning at day 3) and reach a plateau after day 15 (Figure 2.8a); *osteonectin* levels rise later in the differentiation process, starting with day 9 and plateau toward the end of the process, after day 20 (Figure 2.8b).

Gene expression controls differentiation rates, *i.e.*, the term $D_{out}^{(TYP)}(x,t)$ from equation (2.10), which depends on the differentiation fraction calculated as per equation (2.25); the variable $f_{diff}^{(TYP)}$ is the only link between gene expression and the cell cycle (and osteogenic differentiation) in the mathematical model. Figure 2.9 shows the calculated differentiation fractions for MSC and PRE cells, as they change throughout the osteogenic differentiation process.

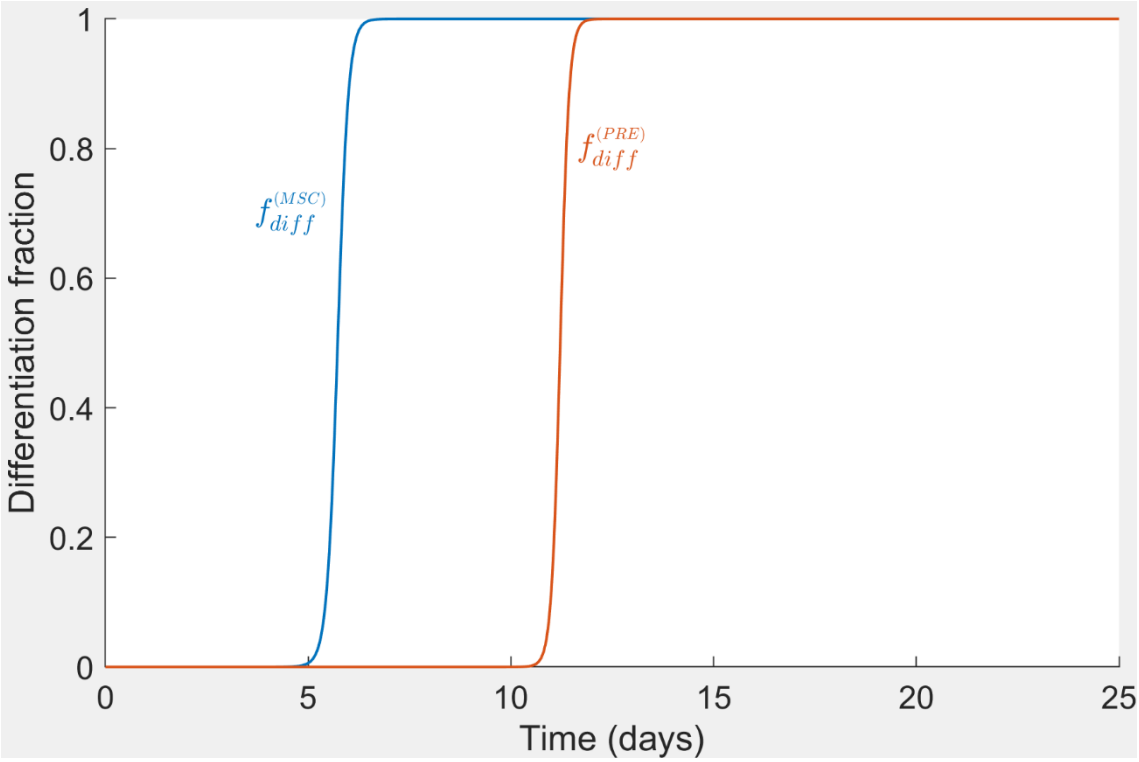

Figure 2.9. Differentiation fraction throughout the osteogenic differentiation process, calculated as per equation (2.25)

Population dynamics were captured throughout the osteogenic differentiation process, achieving deconvolution of population heterogeneity (Figure 2.10). The total population count increase at a steady growth rate during the first week of differentiation; the total population numbers increase sharply between day 7 and day 14, reaching a plateau after day 15 at approximately 4-times higher cell count compared with the initial undifferentiated count. The detailed description of the cell distribution (between the differentiation states and cell cycle phases) is virtually impossible to reproduce experimentally because of associated technical challenges, financial constraints, or both. Therefore, only some of the results of the mathematical model are compared with the available experimental data: the total cell count. Simulation results show that the population

of undifferentiated mesenchymal stem cells (solid blue line) starts to decline at day 6, when osteoprogenitors first appear. The previously non-existent pre-osteoblast population (dashed orange line) rises at the same timepoint (day 6) until approximately day 12, when the terminally differentiated osteoblasts emerge (dash-dotted yellow line). The pre-osteoblast count decreases after day 12 because of their terminal differentiation to osteoblasts, while the number of osteoblasts rises until reaching a plateau after day 19, when their count virtually equals the total population.

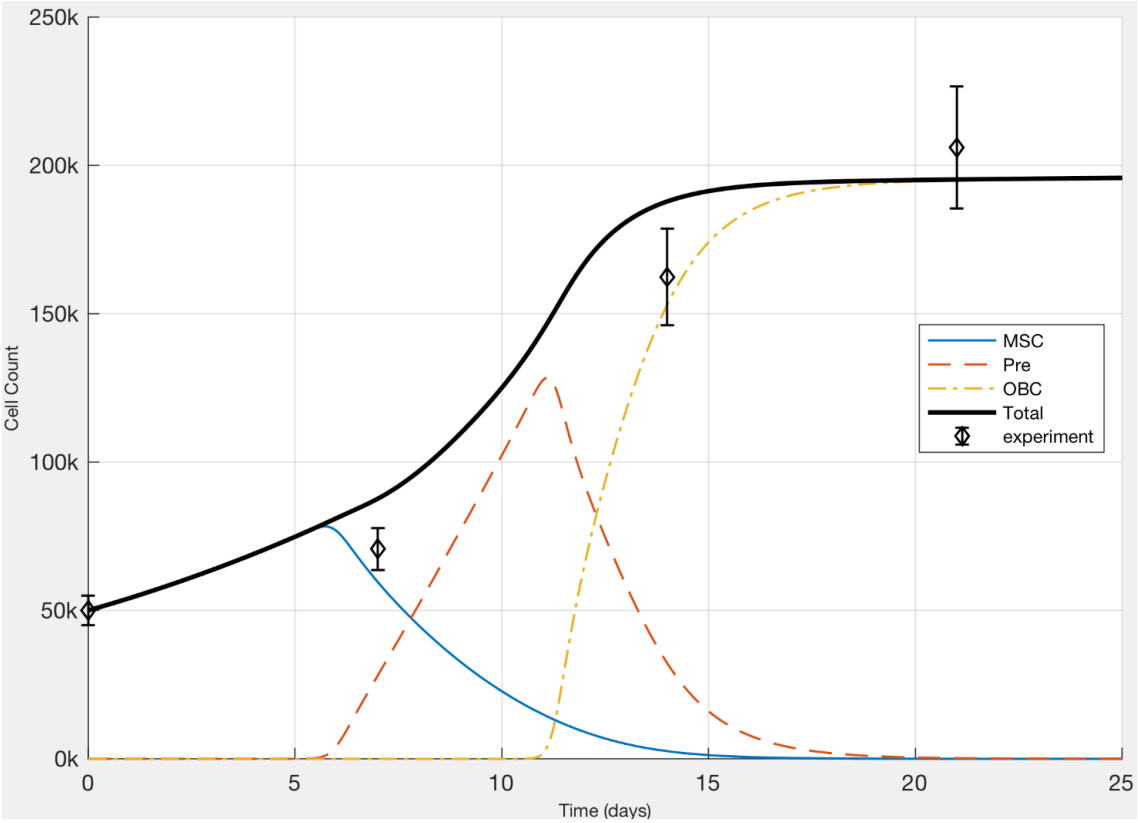

Figure 2.10. Partial and total cell counts during the osteogenic differentiation process of mesenchymal stem cells. Comparison between experimental measurements (black diamond symbols with vertical error bars) and the prediction of the mathematical model for the total cell count (solid black line). Partial cell counts are represented as follows: solid blue line for MSC count, orange dashed line for PRE count, and yellow dash-dotted line for OBC count. [85]

Herein, the first comprehensive population balance model of osteogenic differentiation has been presented, incorporating a description of cell cycle dynamics, intracellular metabolism, and gene expression. *In-silico* results showed that cell cycle dynamics play a significant role in the timing of the process of osteogenic differentiation of mesenchymal stem cells and confirmed that the expression of differentiation genes plays a crucial role in the process of

osteogenesis. Most importantly, the proposed mathematical model captures the heterogeneity of cell populations during osteogenic differentiation, reproducing the experimentally observed cell culture behavior over the course of osteogenesis (Figure 2.7 to Figure 2.10).

Stem cell culture kinetics have been previously modelled, including cell death and cell differentiation, assigning cells to compartments [97] based on their differentiation state. Herein modelling of the differentiation has been performed with higher fidelity and level of detail at every step of the modelling process. The population balance equation enables the quantification of individual population numbers (*i.e.*, for each cellular differentiation state: MSC, PRE, or OBC) as well as cell cycle heterogeneity. Differentiation is not merely described by the model, but also located precisely during the G1 phase of the division cell cycle (phase G in the mathematical model formulation). The ability to untangle the heterogeneity of mesenchymal stem cell cultures during osteogenic differentiation *in silico* provides a unique capability that is not achievable with conventional *in-vitro* methods [85]. Accounting for such heterogeneity and linking it to gene expression and metabolism can lead to culture optimization for high quality osteogenic differentiation for bone tissue engineering purposes. The model can potentially point toward the targeted optimization of culture parameters related to extracellular metabolism leading to high quality osteogenic differentiation. To achieve targeted culture optimization mathematical modelling should be combined with *in-vitro* experimentation. Such culture optimization may be achieved with the use of large scale (*e.g.*, genome scale) metabolic models. However, the implementation of such models is technically challenging and complicated since these models rely on the existence of an objective to guide intracellular activity and stem cell differentiation demands the use of multiple objective functions to account for multiple competing cell behaviors throughout the differentiation process. Compared with genome-scale models, the metabolic model described herein is computationally faster, since it monitors a lower number of metabolites; it also requires fewer measurements, only for the metabolites that are included in the mathematical model; while this mathematical model provides results for fewer metabolites (only 8 metabolites involved in glycolysis, oxidative phosphorylation, and glutaminolysis) it captures pathways

that were shown to be significant [98–101] for the osteogenic differentiation of mesenchymal stem cells.

Population balance models have been previously used to describe stem cell cultures. Wu *et al.* [102] used population balance equations to describe the size of cell aggregates cultured in spinner flasks. In this work, population balance has been utilized in a different manner, modelling cell cycle heterogeneity as an uneven distribution of the cells between and within cell cycle phases. The mathematical model described herein considers cellular metabolism directly linked to cell proliferation, in contrast to Wu *et al.* who modelled oxygen transport as the limiting factor for stem cell proliferation. Bartolini *et al.* [103] used population balance equations to describe the cell division cycle and study the proliferation of stem cells in suspension bioreactors with a special focus on bioreactor dynamics and operation, rather than intracellular gene and metabolic activity. A similar population balance approach has been utilized to study cell cycle phase-specific chemical treatment of leukemia [104] describing the effect of cell cycle heterogeneity on healthy and leukemic subpopulations subjected to chemotherapy. Similar to Münzer *et al.* [105], the mathematical model presented in this chapter provides a detailed description of cell cycle heterogeneity. However, this model focuses on the regulation of stem cell differentiation by gene expression and provides a more accurate description of cellular metabolism by utilizing intracellular metabolic reactions instead of extracellular metabolite measurements which may not accurately represent intracellular metabolic network activity [106,107].

Stem cells proliferate slower during differentiation [108], directing their energy through other metabolic pathways than those required for optimal (maximum) growth. *In-silico* exploration by repeated computer simulations affords comprehensive evaluation of cell proliferation with relation to metabolism by linking cellular growth rate to the rate of energy production. Simulation results for parameter sweeps around their nominal value show that shorter cell cycle duration results in delayed differentiation, even though the two cellular functions (proliferation and differentiation) do not directly compete in terms of energy demand (in the mathematical model). This result suggests that, under the constraint of a limited time span one may have to choose between obtaining

either a higher number of less differentiated cells or a lower number of more differentiated cells. This effect can be explained by the fact that cell cycle duration is strongly correlated with the duration of the G0/G1 phase; consequently, shorter cell cycle times are translated to reduced time spent by cells in the G0/G1 phase and a narrower time-window when differentiation can occur. Even though short cell cycle times delay the differentiation process, all the characteristic metabolic and genetic changes that are observed when using the nominal values of the parameters still occur as part of the differentiation process, but they do so later. These changes include an increase in metabolic activity during the differentiation period, followed by a decrease (in metabolic activity) toward the end of differentiation, as well as an increase in the relative gene expression of *Runx2* followed by a rise in *osteonectin* levels, as an indication of successful progression of osteogenesis [109].

Global parameter sensitivity analysis was performed by simultaneously varying the values of all the parameters in a space ranging from 50% to 150% around their nominal values. Interestingly, analysis results show that the parameters that have the highest total sensitivity indices are directly involved in osteogenic gene expression, even though the mathematical connection between the model outputs (*i.e.*, cell counts) and genetics first traverses the metabolic reaction rates and intracellular metabolite concentrations and is only indirectly linked with gene expression. This result is mathematically justified if we acknowledge that in a significant proportion of simulations the cells do not differentiate at all for certain choices for the parameter sets. In other words, while the impact of the metabolic parameters on the growth rates for individual cell types is bound at roughly 50% around the nominal value, the values of the gene-related parameters can completely change the prediction and outcome of the model, increasing their significance value as calculated by the global analysis technique and demanding the precise determination of the values of these parameters from carefully designed experiments. This type of result requires a detailed model of the gene expression during the differentiation process. Other published models of differentiation describe in less detail the expression of genes related to osteogenesis. While this chapter showcases an unstructured and segregated stem cell mathematical model to capture the cell-cycle culture

heterogeneity, Vozzi *et al.* [110] used a structured and unsegregated cell model in their study of the lifespan and senescent behavior of stem cells. Thalheim *et al.* [111] employed a 3D computational model to study stem cell competition in intestinal crypts involving phenomena from multiple scales, akin to this work. However, there are fundamental differences in the two approaches: since the intestinal crypts only contain a small number of (stem) cells (typically 5–15), they were able to model each cell individually, which would be impractical for the large cell counts that occur in osteogenic differentiation experiments (more than 50000 per well plate). The model by Chen *et al.* [112] described cell population counts using two ordinary differential equations, one for each type of cell (MSCs and chondrocytes). While their model also described MSC differentiation, they focused on the effect of the transforming growth factor beta (TGF-β) on the chondrogenic differentiation of mesenchymal stem cells, while the current chapter presents the results of a mathematical model that encompasses cell cycle dynamics, intracellular metabolism, and genetics, as well as the connections between them. Finally, Renardy *et al.* [113] investigated the stability of regenerating tissues in terms of cell fraction by type and population recovery rate, looking for the conditions (parameter values) necessary for the tissues to maintain normal function.

This chapter introduced a novel mathematical model built from first principles, whose key contributions lie in the form of the transition function being used by phases G and M, and in the integration of intracellular metabolism and gene expression (for a vital subset of metabolites and genes) with cell growth and osteogenic differentiation, while at the same time capturing the heterogeneity of the cellular division cycle (both between and within cell cycle phases).

Chapter 3. Mathematical modeling of the osteogenic differentiation of mesenchymal stem cells in a rotating-wall bioreactor

This chapter presents a mathematical model for the osteogenic differentiation of alginate-gelatin-bead-encapsulated umbilical cord blood mesenchymal stem cells in a rotating wall bioreactor. To describe osteogenic differentiation in detail, the model encompasses phenomena at multiple scales, from intracellular energy metabolism and gene expression to cell cycle and differentiation state population level heterogeneity, to bead level nutrient and waste mass transport phenomena as well as bioreactor-level mass balances. The model is constructed around a population balance core and provides a framework for culture and reactor process optimization to build upon. The work showcased in this chapter contributes to the scientific literature the novelty of the multi-scale approach applied to stem cell cultures, with a highly detailed description at the single cell and cell population scales, integrating intermediary (alginate-gelatin bead) and macroscopic (reactor) scale phenomena into the model.

The structure of the chapter begins with a section containing the description of the physical and biological phenomena being modelled (intracellular metabolism, gene expression, cell division and differentiation, and extracellular metabolite transport). The following section presents the method for solving the mathematical model by discretizing distributed variables that are part of integral, partial differential and algebraic equations (IPDAEs). Next, the main results of the chapter (rotating-wall bioreactor) are unveiled and compared with the results from the previous chapter describing the osteogenic differentiation of mesenchymal stem cells in well plate cultures. Following the results, the findings of this chapter are discussed and contrasted with other relevant publications. Finally, the validity of the mathematical model is assessed by investigating its predictions under various circumstances corresponding to meaningful biological scenarios.

3.1. Mathematical model formulation

The osteogenic differentiation of MSCs was carried out in a 55 mL perfusion rotating wall bioreactor that allowed fresh culture medium to be continuously fed into the reactor while removing existing spent medium from the reactor at the same time; the cells were encapsulated in alginate-gelatin beads throughout the differentiation process. Oxygen was supplied to the culture medium via semipermeable tubing before entering the reactor and a gas-permeable membrane acting as the outer surface of the reactor [114,115]. The cells are encapsulated within alginate-gelatin beads [116], which have been optimized for stem cell expansion and osteogenic differentiation [117]. In formulating the mathematical model for the MSC osteogenic differentiation process, phenomena at the cell, bead, and reactor level were described and interlinked.

The mathematical model is built around a population balance core that is very similar to the one used in the previous chapter. This was a natural choice, since the model in this chapter builds upon the innovation from the previous chapter, and the same cell line is being used. Thus, the description of the intracellular landscape matches the one presented in Figure 2.1, and the differentiation sequence follows the diagram from Figure 2.2. The set of intracellular metabolites and genes has been kept unchanged (Figure 2.3), but the definition of the cell distribution variable has been updated to a cell density distribution, which is better suited for the three-dimensional structure of the alginate-gelatin bead. The description of the cell division cycle in terms of its component phases is the same as shown in the previous chapter (Figure 2.4).

Cells no longer interact with the (liquid) culture medium directly. Instead, the alginate-gelatin bead that they are encapsulated within plays the role of the extracellular environment. The extracellular alginate-gelatin bead volume uses separate molar balance equations to keep track of metabolite transport by molecular diffusion, as well as cross-membrane transport performed by the cells. This osteogenic differentiation process was carried out in a rotating wall bioreactor, where the encapsulated cells were free to move as the outer walls of the reactor kept rotating. Metabolite transport occurs at the reactor scale between

the bulk culture medium and the alginate-gelatin beads as well as inside the beads and is described through rigorous mass balance equations.

In summary, the mathematical model encompasses and interconnects phenomena at the cellular, bead, and bioreactor scales; it captures intracellular metabolism, gene expression, and spatial and cell cycle heterogeneity for each of the three differentiation states, throughout the osteogenic differentiation process.

3.1.1. Assumptions

All assumptions listed in the chapter titled “Mathematical modeling of the osteogenic differentiation of mesenchymal stem cells in well-plate culture” are applicable to the model presented in this chapter. Additionally, the assumptions below also apply.

- The flow of the culture medium inside the rotating-wall bioreactor corresponds to perfect mixing conditions during the osteogenic differentiation process.
- All alginate-gelatin beads in the rotating-wall bioreactor are identical, in terms of their geometry, size, as well as metabolic, genetic, and cellular density distribution within the bead volume. Bead-to-bead variability is considered negligible by the mathematical model.

3.1.2. Balance equations for intracellular metabolism

The concentration levels of intracellular metabolites vary with cell type, radial position (in the alginate-gelatin bead), and time. The mechanism regulating the intracellular metabolism of the cells should not depend on the details of the experimental setup utilized to culture them. Therefore, intracellular metabolism uses equations that are built on those in the previous chapter, modified to account for the location of the cells within the alginate-gelatin bead.

Thus, the molar balance for intracellular metabolites is given by equation (3.1), whose right-hand side terms represent, in order: the contribution of incoming cells that may have different intracellular metabolic activity levels when differentiating into the current type, net intracellular metabolite generation rate,

and net cross-membrane transfer. The previous chapter of this thesis provides a more detailed explanation of each term of the intracellular molar balance equation.

$$\frac{\partial M_m^{(TYP)}(r,t)}{\partial t} = \frac{\int_{x_{min,G}}^{x_{max,G}} D_{out}^{(TYP-1)}(r,x,t)\,dx}{N_{total}^{(TYP)}(r,t)} \cdot \left(M_m^{(TYP)}(r,t) - M_m^{(TYP-1)}(r,t)\right) + \sum_{i=1}^{N_R}\left(STOIC_{m,i} \cdot RRate_i^{(TYP)}(r,t)\right) + \sum_{j=1}^{N_T}\left(STOIC_{m,j+N_R} \cdot \frac{TRate_j^{(TYP)}(r,t)}{V_{cell}}\right) \quad (3.1)$$

The intracellular reaction rate has a first-order linear dependence on the concentration of the corresponding reactant as shown in equation (3.2). $C_{R_i}(r,t)$ refers to the concentration of the reactant for intracellular metabolic reaction number i and can be identified from the stoichiometric matrix (2.2) by looking at the column pertaining to reaction i and choosing the only row for which the coefficient is negative (*i.e.*, the reactant); the leftmost column gives the name of the metabolite playing the role of the reactant for reaction i.

$$RRate_i^{(TYP)}(r,t) = k_{cat,i} \cdot C_{R_i}(r,t) \quad (3.2)$$

Cross-membrane transport rates are calculated using equation (3.3), which corresponds to product-inhibited enzymatic transport and assumes that the amount of transporter enzyme found in the cell membrane is constant for each of the three cell types (MSC, PRE, and OBC) but different for each cell type.

$$TRate_i^{(TYP)}(r,t) = \frac{k_{E,i}^{(TYP)} \cdot C_{M_i,out}(r,t) \cdot k_{T,i}}{k_{T,i} + M_{T_i}^{(TYP)}(r,t)} \quad (3.3)$$

3.1.3. Balance equations for gene expression

Intracellular expression of gene mRNA depends on time, differentiation state, and position of the cell within the alginate-gelatin bead. The molar balance equation (3.4) expresses the accumulation rate of gene-specific mRNA in terms

of base expression of each gene i in the undifferentiated MSC state, transcription rate of the gene from its corresponding location within the DNA of the cell, natural decay of intracellular mRNA; the last term on the right-hand side of the equation accounts for differences in gene expression levels between cells as they change their differentiation state.

$$\frac{\partial G_i^{(TYP)}(r,t)}{\partial t} = \omega_i + \frac{k_{trans,i} \cdot {A_{Gi}^{(TYP)}}^{n_{trans}}}{{A_{Gi}^{(TYP)}}^{n_{trans}} + {k_{DNA,i}}^{n_{trans}}} - k_{decay} \cdot G_i^{(TYP)}(r,t) + \frac{\int_{x_{min,G}}^{x_{max,G}} D_{out}^{(TYP-1)}(r,x,t)\, dx}{N_{total}^{(TYP)}(r,t)} \cdot \left(G_i^{(TYP)}(r,t) - G_i^{(TYP-1)}(r,t)\right) \tag{3.4}$$

The molar balance for the intracellular concentration of dexamethasone (the osteogenic differentiation agent being used in the experiments supporting this work [85]) is given by equation (3.5), which relates the accumulation rate of dexamethasone inside the cell to its rate of transfer through the cell membrane. The molar balances for dexamethasone in the alginate-gelatin bead and culture medium compartments are given in another chapter below.

$$\frac{d}{dt}\left(V_{cell} \cdot Dex_{cell}(r,t)\right) = \lambda_{membrane} \cdot \left(Dex_{bead}(r,t) - Dex_{cell}(r,t)\right) \tag{3.5}$$

3.1.4. Population balance equations for the cellular division cycle and cell differentiation

Similar to chapter 2.1.5, the cell division cycle is described in terms of the main growth stages: phase G lumps Gap 0 and Gap 1, phase S models DNA synthesis, and phase M lumps Gap 2 and mitosis. The order of progression through cell division cycle used in the mathematical model, G–S–M, matches the biological succession (gap 1, synthesis, gap 2, and mitosis). The independent variables are the position of the cell within the alginate-gelatin bead (r), the phase growth coordinate (x), and time (t). The model ignores the specific cyclins that characterize each cell cycle phase and abstracts that notion into a shared distribution domain (*i.e.*, the growth coordinate).

Each cell cycle phase functions in the same way for each of the three modelled differentiation states (MSC, PRE, and OBC) since cell cycle phases are not specific to any one cell type and are generally applicable to the eukaryote class. Equation (3.6) describes the location- and time-dependent density distribution over the growth coordinate of cells as they traverse cell cycle phase G. The terms on the left-hand side of the equation represent, in order: time derivative of the cell density distribution, progress rate in traversing the current growth phase, death rate, and transition rate (to the next cell cycle stage: phase S). The right-hand side (RHS) of the equation contains the boundary condition and differentiation rates. The RHS boundary condition ensures that cells start each growth phase from the beginning (all incoming cells are added to the cell cycle phase at the lowest phase coordinate, where the Kronecker delta function is equal to 1). The two differentiation terms account for the contribution of differentiation to the number of cells of the current type: cells that become the current type are counted as inflow, and cells that are differentiating further are regarded as outflow.

$$\frac{\partial N_G^{(TYP)}(r,x,t)}{\partial t} + \frac{\partial\left[\mu_G^{(TYP)}(r,x,t)\cdot N_G^{(TYP)}(r,x,t)\right]}{\partial x} + \theta_G^{(TYP)}(r,x,t)\cdot \\ \cdot N_G^{(TYP)}(r,x,t) + T_{G,out}^{(TYP)}(r,x,t)\cdot N_G^{(TYP)}(r,x,t) \\ = \delta_K\left(x, x_{min,G}\right)\cdot T_{G,in}^{(TYP)}(r,t) + D_{out}^{(TYP-1)}(r,x,t) - D_{out}^{(TYP)}(r,x,t) \tag{3.6}$$

The equation for the DNA synthesis phase (labelled “S”) follows a similar approach to phase G, keeping only the relevant terms. Since the main objective of the cell during phase S is DNA code duplication, neither transition nor differentiation are part of equation (3.7).

$$\frac{\partial N_S^{(TYP)}(r,x,t)}{\partial t} + \frac{\partial\left[\mu_S^{(TYP)}(r,x,t)\cdot N_S^{(TYP)}(r,x,t)\right]}{\partial x} + \theta_S^{(TYP)}(r,x,t)\cdot \\ \cdot N_S^{(TYP)}(r,x,t) = \delta_K\left(x, x_{min,S}\right)\cdot T_{S,in}^{(TYP)}(r,t) \tag{3.7}$$

The final phase of the cell division cycle (labelled “M”) includes terms for the temporal derivative of the cell density distribution, phase traversal rate, death rate, transition rate on the left-hand side, and the boundary condition on the right-hand side (3.8). Considering that the main objective of the cell during mitosis is cellular division, differentiation is excluded from the list of cellular behaviors exhibited by cells while traversing phase M.

$$\begin{aligned}\frac{\partial N_M^{(TYP)}(r,x,t)}{\partial t} + \frac{\partial\left[\mu_M^{(TYP)}(r,x,t)\cdot N_M^{(TYP)}(r,x,t)\right]}{\partial x} + \theta_M^{(TYP)}(r,x,t)\cdot \\ \cdot N_M^{(TYP)}(r,x,t) + T_{M,out}^{(TYP)}(r,x,t)\cdot N_M^{(TYP)}(r,x,t) \\ = \delta_K\left(x, x_{min,M}\right)\cdot T_{M,in}^{(TYP)}(r,t)\end{aligned} \tag{3.8}$$

For each differentiation state (denoted by the superscript “TYP”), the total (position and time dependent) cell density is obtained by summing the total densities for each growth phase (only from cells that are at the corresponding differentiation state), as shown in equation (3.9).

$$\begin{aligned}N_{total}^{(TYP)}(r,t) = \int_{x_{min,G}}^{x_{max,G}} N_G^{(TYP)}(r,x,t)\,dx + \int_{x_{min,S}}^{x_{max,S}} N_S^{(TYP)}(r,x,t)\,dx \\ + \int_{x_{min,M}}^{x_{max,M}} N_M^{(TYP)}(r,x,t)\,dx\end{aligned} \tag{3.9}$$

Equation (3.10) shows the approach for the calculation of the total cell count per alginate-gelatin bead, by integrating the density of the cells over the bead volume. The right-hand-side of the equation shows the calculation method being used under the assumptions stated in this chapter (*i.e.*, spherical symmetry of the beads).

$$\iiint_{V_{bead}} \left(\sum_{TYP} N_{total}^{(TYP)}(r,t)\right) dV = \int_0^{R_{bead}} \left(\sum_{TYP} N_{total}^{(TYP)}(r,t)\right)\cdot 4\pi r^2\,dr \tag{3.10}$$

The duration of phase G is correlated with the production rate of energy cofactors (3.11), separately for each differentiation state TYP. The production rates for the cofactors (the two partial derivatives from the equation below) are calculated as per equation (3.1); although they are distinct model entities, the parameters connecting cofactor production rates to the duration of phase G are interdependent $E_{NADH}^{(TYP)} = 2.5 \cdot E_{ATP}^{(TYP)}$, since the electron transport chain processes NADH to produce more ATP [95].

$$duration_G^{(TYP)}(r,t) = \frac{1}{E_{ATP}^{(TYP)} \cdot \frac{\partial M_{ATP}^{(TYP)}(r,t)}{\partial t} + E_{NADH}^{(TYP)} \cdot \frac{\partial M_{NADH}^{(TYP)}(r,t)}{\partial t}} \tag{3.11}$$

The transition rates between growth phases, which are used in the boundary conditions on the right-hand side of equations (3.6), (3.7) and (3.8), transfer cells from each growth phase to the following one, thus ensuring cell cycle phase progression. Equation (3.12) gives the transition rate into phase G; the number 2 multiplying the integral on the right-hand side of the equation accounts for cell duplication during mitosis.

$$T_{G,in}^{(TYP)}(r,t) = 2 \cdot \int_{x_{min,M}}^{x_{max,M}} T_{M,out}^{(TYP)}(r,x,t) \cdot N_M^{(TYP)}(r,x,t)\, dx \tag{3.12}$$

Equation (3.13) gives the transition rate of cells from phase G into the DNA synthesis phase.

$$T_{S,in}^{(TYP)}(r,t) = \int_{x_{min,G}}^{x_{max,G}} T_{G,out}^{(TYP)}(r,x,t) \cdot N_G^{(TYP)}(r,x,t)\, dx \tag{3.13}$$

Equation (3.14) gives the transition rate from phase S into phase M. Due to the requirement that DNA be properly duplicated before progressing into the following phase, the transition rate is no longer distributed over the phase coordinate around a mean value and occurs at a single point (labelled $x_{max,S}$) instead.

$$T_{M,in}^{(TYP)}(r,t) = \mu_S^{(TYP)}(r,x,t) \cdot N_S^{(TYP)}\left(r, x_{max,S}, t\right) \tag{3.14}$$

Cells leave phase M to divide and transition into phase G at a rate given by equation (3.15). The transition rate is distributed over the phase coordinate (as well as position within the alginate-gelatin bead, r, and time, t) and depends on the growth rate of the cells traversing phase M, as well as the cumulative probability of transition at the current growth coordinate. Since the phase growth coordinate setup is identical to the one used for the well plate culture in the previous chapter, the expression for the cumulative transition probability is given by equation (2.23).

$$T_{M,out}^{(TYP)}(r,x,t) = \frac{\mu_M^{(TYP)}(r,x,t) \cdot \frac{dP_M(x)}{dx}}{1 - P_M(x)} \tag{3.15}$$

The rate for transition between phase G and phase S uses the more complicated formulation (3.16), which accounts for the possibility for cells to leave phase G either by transitioning into phase S or by differentiating into a more specialized cell type. Note that the equation for the transition rate reduces to the expression used for phase M (equation (3.15) valid for transition in the absence of differentiation) when the differentiation fraction ($f_{diff}^{(TYP)}$) is null, and becomes zero when the differentiation reaches the (maximum) value 1. The expression for the cumulative probability of transition $P_G(x)$ is given by equation (2.22).

$$T_{G,out}^{(TYP)}(r,x,t) = \frac{\mu_G^{(TYP)}(r,x,t) \cdot \left(1 - f_{diff}^{(TYP)}(r,t)\right) \cdot \frac{dP_G(x)}{dx}}{1 - f_{diff}^{(TYP)} \cdot CPD_G(x) - \left(1 - f_{diff}^{(TYP)}(r,t)\right) \cdot P_G(x)} \tag{3.16}$$

Cell may also undergo differentiation while traversing phase G, at a rate given by equation (3.17). Note that when the differentiation fraction is zero, the differentiation rate is also null, and the derivative of the differentiation rate with respect to the growth coordinate is positive, reaching the maximum value (for the differentiation rate) when the differentiation fraction is also at its maximum value

of 1. The function for the cumulative probability of differentiation, $CPD_G(x)$, is calculated as per equation (2.24).

$$D_{out}^{(TYP)}(r,x,t) = \frac{\mu_G^{(TYP)}(r,x,t) \cdot f_{diff}^{(TYP)}(r,t) \cdot \frac{dCPD_G(x)}{dx} \cdot N_G^{(TYP)}(r,x,t)}{1 - f_{diff}^{(TYP)} \cdot CPD_G(x) - \left(1 - f_{diff}^{(TYP)}\right) \cdot P_G(x)} \quad (3.17)$$

The value of the differentiation fraction depends on the position of the cells within the alginate-gelatin bead and is expressed in terms of the relative expression of its key gene and a single differentiation parameter (*i.e.*, $k_{diff}^{(TYP)}$), as per equation (3.18). The key gene for mesenchymal stem cells (TYP=MSC) is *Runx2*, while the key gene for pre-osteoblasts (TYP=PRE) is *osteonectin*. Osteoblasts (TYP=OBC) do not further differentiate, as per equation (3.19).

$$f_{diff}^{(TYP)}(r,t) = \frac{{G_{key}^{(TYP)}}^{dxp}}{{k_{diff}^{(TYP)}}^{dxp} + {G_{key}^{(TYP)}}^{dxp}} \quad (3.18)$$

$$f_{diff}^{(OBC)}(r,t) = 0 \quad (3.19)$$

3.1.5. Mass balance at the alginate-gelatin bead and bioreactor scales

Diffusive transport through the spherical alginate-gelatin bead is modeled through the molar balance equation (3.20) for the three extracellular metabolites (glucose, lactate, and glutamine) and the differentiation agent (dexamethasone). The accumulation of metabolite in the alginate-gelatin bead is expressed by the partial derivative on the left-hand side; the two terms on the right-hand side of the equation are the negative divergence of the molar flux (accounts for diffusive transport of metabolite within the bead) and the net rate of generation for metabolite m (accounts for uptake or release of metabolites by the cells *via* cross-membrane transportation). The mathematical formulation utilizes identical beads with 1.15 mm radius, in agreement with the experimental technique that produced them [115,118], neglecting bead size distribution.

$$\frac{\partial C_m(r,t)}{\partial t} = -\nabla \cdot \overrightarrow{F_m(r,t)} + RV_m(r,t) \tag{3.20}$$

Under the assumption of spherical symmetry, the divergence term in equation (3.20) can be written explicitly as a partial derivative in the radial direction. Equation (3.21) is obtained by substituting the divergence term in equation (3.20) with the corresponding partial derivative; although the two equations are equivalent under the working assumptions, equation (3.21) is more useful for numerical model formulation, as the partial derivative can be readily replaced by a finite difference or encapsulated in a finite element discretization scheme.

$$\frac{\partial C_m(r,t)}{\partial t} = -\frac{1}{r^2} \cdot \frac{\partial}{\partial r}\left(r^2 \cdot F_{m,r}(r,t)\right) + RV_m(r,t) \tag{3.21}$$

The constitutive equation for the diffusive molar flux density of metabolite m is given by equation (3.22), which is also known as Fick's first law of diffusion. Under the assumption of spherical symmetry, the concentration gradient is equal to the partial derivative of the concentration in the radial direction, as per equation (3.23), which is the variant implemented by the computational counterpart to the mathematical model.

$$\overrightarrow{F_m(r,t)} = -\mathcal{D}_m \cdot \nabla C_m(r,t) \tag{3.22}$$

$$F_{m,r}(r,t) = -\mathcal{D}_m \cdot \frac{\partial C_m(r,t)}{\partial r} \tag{3.23}$$

Each of the molar balance equations is accompanied by corresponding boundary conditions: the molar flux density through the center of the spherical bead is null, due to symmetry (3.24); molar fluxes through the outer surface of the bead are calculated using mass transfer equation (3.25) whose partial mass transfer coefficient $k_{bead,m}$ is based on a dimensionless correlation. Although the mathematical model uses the full form of mass transfer correlation equation (3.26) [119] (as cited by [120]), the flow velocity corresponds to a very low Reynolds number ($Re < 10^{-3}$), and the Sherwood number (Sh) is practically

equal to 2. The perfused culture medium replenishes the main metabolites (glucose and glutamine) and removes lactate from the bioreactor without meaningfully affecting their transfer rate between the alginate-gelatin bead and the culture medium in the bulk of the liquid surrounding the beads.

$$F_{m,r}(0,t) = 0 \tag{3.24}$$

$$F_m(R_{bead},t) = k_{bead,m} \cdot \left(C_m(R_{bead},t) - CC_m(t)\right) \tag{3.25}$$

$$\frac{k_{bead,m} \cdot R_{bead}}{\mathcal{D}_m} = Sh_m = 2 + 0.6 \cdot Re^{1/2} \cdot {Sc_m}^{1/3} \tag{3.26}$$

The volumetric reaction term appearing in equations (3.20) and (3.21) is defined by equation (3.27). Each extracellular metabolite m is paired with its own transport rate i as follows: glucose is transported with rate 1, lactate with rate 2, and glutamine with rate 3. The negative sign at the beginning of the equation accounts for the fact that the values of the transport rates ($TRate_i^{(TYP)}$) correspond to their intracellular effect and not their effect on the bead metabolite levels: *e.g.*, the glucose transport rate is positive (for the cell) but has the effect of reducing the concentration of glucose locally in the alginate-gelatin bead. The measurement units on the right-hand side (molar flowrate in $pmol/day$, and cell density in L^{-1}) combine to form the correct unit on the right-hand side (reaction rate in $pmol \cdot day^{-1} \cdot L^{-1}$).

$$RV_m(r,t) = -\sum_{TYP} TRate_i^{(TYP)}(r,t) \cdot N_{total}^{(TYP)}(r,t) \tag{3.27}$$

Because the rate cross-membrane transport of dexamethasone is modelled differently than the transport of metabolites, the corresponding reaction rate term is adapted to the specifics of dexamethasone transport, as per equation (3.28).

$$RV_{Dex}(r,t) = \lambda_{membrane} \cdot \left(Dex_{cell}(r,t) - Dex_{bead}(r,t)\right) \cdot N_{total}^{(TYP)}(r,t) \tag{3.28}$$

Finally, the molar balance equations for mass transport inside the alginate gelatin bead are accompanied by initial conditions for each variable: the concentration of metabolites is considered the same as in the culture medium, whereas concentration of dexamethasone starts at zero.

Metabolite levels in the culture medium are modelled using equation (3.29), which accounts for metabolite transport between the culture medium and alginate-gelatin beads, as well as flow in and out of the reactor. The reactor scale molar balance equation (3.29) is valid for the three extracellular metabolites (glucose, lactate, and glutamine) and the differentiation agent (dexamethasone).

$$\frac{d\left(V_R \cdot CC_m(t)\right)}{dt} = F_{m,r}(R_{bead}, t) \cdot \left(4 \cdot \pi \cdot {R_{bead}}^2\right) \cdot N_{bead} + F_{IN} \cdot \left(C_{IN,m} - CC_m(t)\right) \tag{3.29}$$

3.2. Solution methodology

The computer implementation of the mathematical model uses discretized versions of the equations for distributed variables. For accurate calculations, phases G and M are each discretized into 100 bins, phase S is discretized into 50 bins, and the alginate-gelatin bead into 16 spherical shells, similar to chapter 2.2. The complete implementation consists of 12,563 ordinary differential equations, which are solved using the `ode15s` routine provided by MATLAB [121]. The average solution time is about one hour on a computer with a 4.20GHz Intel® Core™ i7-7700K CPU and 16 GB of RAM. Although the more popular `ode45` MATLAB routine typically produces a (slightly) more accurate solution than `ode15s`, the latter was employed to solve the mathematical formulation of the problem, because the stiff system of ordinary differential equations presented herein requires prohibitively more time to solve using `ode45`, necessitating more than two weeks (of computational time) to calculate the solution of the model up to day 10 of the simulation for the osteogenic differentiation process.

All distributed variables are discretized (over the phase growth coordinate, x, and the radial position in the alginate-gelatin bead, r) before

running the simulation and each of the continuous partial differential equations becomes multiple discrete ordinary differential equations, with time as the unique independent variable. The radial domain is discretized by the index j, ranging from 1 to 16, while the growth coordinate is discretized by the index i, ranging from 1 to 100 for phases G and M and from 1 to 50 for phase S. In the equations below, the index j corresponds to radial position $j \cdot \Delta r$, where Δr is the results of dividing the bead radius by the number of spherical shells (16 in this case); the index i corresponds to growth coordinate $x_{min} + i \cdot \Delta x$, where Δx is found by dividing the total span of the growth phase ($x_{max} - x_{min}$) by the number of bins used to discretize the particular cell cycle phase.

The discretization of equation (3.6) — which describes cells as they progress through phase G of the cell division cycle — is presented in two parts: equation (3.30) is valid for $i = 1$ and includes the boundary condition specifying the location at which cells enter the cycle phase, while equation (3.31) is valid for $i \geq 2$ and describes phase traversal. Each $N_G^{(TYP)}(r, x, t)$ distributed variable is turned into 1600 time-dependent $N_{G,j,i}^{(TYP)}(t)$ variables per differentiation state TYP.

$$\frac{dN_{G,j,1}^{(TYP)}(t)}{dt} + \frac{\mu_{G,j}^{(TYP)}(t) \cdot \left[N_{G,j,1}^{(TYP)}(t) - 0\right]}{\Delta x} + \theta_G^{(TYP)}(t) \cdot N_{G,j,1}^{(TYP)}(t) + T_{Gout,j,1}^{(TYP)}(t) \cdot N_{G,j,1}^{(TYP)}(t) = D_{out,j,1}^{(TYP-1)}(t) - D_{out,j,1}^{(TYP)}(t) + T_{Gin,j}^{(TYP)}(t) \tag{3.30}$$

$$\frac{dN_{G,j,i}^{(TYP)}(t)}{dt} + \frac{\mu_{G,j}^{(TYP)}(t) \cdot \left[N_{G,j,i}^{(TYP)}(t) - N_{G,j,i-1}^{(TYP)}(t)\right]}{\Delta x} + \theta_G^{(TYP)}(t) \cdot N_{G,j,i}^{(TYP)}(t) + T_{Gout,j,i}^{(TYP)}(t) \cdot N_{G,j,i}^{(TYP)}(t) = D_{out,j,i}^{(TYP-1)}(t) - D_{out,j,i}^{(TYP)}(t) \tag{3.31}$$

The population balance equations for phases S and M are discretized in an analogous manner, producing an additional 2400 equations per differentiation state. Note that in the computer implementation, the growth rate $\mu_{G,j\cdot\Delta r}^{(TYP)}(t)$ and death rate $\theta_G^{(TYP)}(t)$ are no longer dependent on the cell cycle phase coordinate as the available experimental data were insufficient to support any conceivable

hypothesis over any other; an alternative way to express this choice is that these distributed variables are uniform.

Discretization of the alginate gelatin bead variables was constructed such that the concentration and molar fluxes are staggered along the radial direction. Partial derivatives in the radial direction have been replaced by first order finite differences, which have second order accuracy due to staggering. Thus, the discretized version of the molar balance equation (3.21) for extracellular metabolites inside the alginate-gelatin bead is given by equations (3.32) valid inside the innermost shell (which is a sphere of radius Δr) for $j = 1$ and (3.33) valid at every other discretized radial position where $2 \leq j \leq 16$. Equations (3.32) and (3.33) are written in their shortest form, simplifying factors of Δr where possible.

$$\frac{dC_{m,1}(t)}{dt} = -4 \cdot \frac{F_{m,1}(t)}{\Delta r} + RV_{m,1}(t) \tag{3.32}$$

$$\frac{dC_{m,j}(t)}{dt} = -\frac{1}{(j-0.5)^2} \cdot \frac{j^2 \cdot F_{m,j}(t) - (j-1)^2 \cdot F_{m,j-1}(t)}{\Delta r} + RV_{m,j}(t) \tag{3.33}$$

Equation (3.34) describes the discretized radial component of the molar flux vector whose expression is given by equation (3.23) and applies to all interior points in the bead, except for the bead surface ($2 \leq j < 16$).

$$F_{m,j}(t) = -\mathcal{D}_m \cdot \frac{C_{m,j+1}(t) - C_{m,j}(t)}{\Delta r} \tag{3.34}$$

The boundary condition for the surface flux defined by equation (3.25) remains valid, equation (3.35) explicitly replaces the surface concentration by the outermost available value.

$$F_{m,16}(t) = k_{bead,m} \cdot \left(C_{m,16}(t) - CC_m(t)\right) \tag{3.35}$$

3.2.1. Parameter estimation

Most parameters of the mathematical model presented in this chapter were calibrated based on experimental data. Their values were estimated based on experimental measurements for well-plate cultures and are identical to those used in the mathematical model presented in Chapter 2. The only parameters that were estimated for the bioreactor model presented in this chapter are the diffusion coefficients involved in extracellular diffusive mass transport within the hydrogel bead in the radial direction.

3.2.1.1. Diffusion coefficients for mass transport

To enable the calculation of diffusive molar fluxes and the solution of equation (3.22), (3.23), or (3.34), the values of the diffusion coefficients for each extracellular metabolite, $\mathcal{D}_m$, must be known first. These coefficients' values are available from published literature for glucose and glutamine [122], but not for lactate and dexamethasone. The missing coefficient values were estimated using the Wilke-Chang correlation [123] shown in equation (3.36), where ϕ_S is the association factor for the solvent, M_S is the molar mass of the solvent, T is the absolute temperature, η_S is the viscosity of the solvent, and V_m is the molar volume of the metabolite m at its normal boiling temperature. If values for the above parameters are not available from published literature, they may be estimated using specific methods. Values for the properties of the solvent (alginate-gelatin bead) were considered equal to those for water (given the similar transport behavior of the two materials). The values of the diffusion coefficients used by the mathematical model are listed in Table 3.1.

$$\mathcal{D}_m = \frac{7.4 \cdot 10^{-8} \cdot \sqrt{\phi_S \cdot M_S} \cdot T}{\eta_S \cdot {V_m}^{0.6}} \tag{3.36}$$

Table 3.1. Diffusion coefficient values used by the mathematical model

Parameter	**Value** [122]	**Parameter**	**Value**
$\mathcal{D}_{Glucose}$	$6.7 \cdot 10^{-6}$ cm²/s	$\mathcal{D}_{Lactate}$	$9.9 \cdot 10^{-6}$ cm²/s
$\mathcal{D}_{Glutamine}$	$7.6 \cdot 10^{-6}$ cm²/s	$\mathcal{D}_{Dexamethasone}$	$4.0 \cdot 10^{-7}$ cm²/s

3.3. Simulation results

The mathematical model — consisting of equations (3.1)-(3.3) for intracellular metabolism, (3.4)-(3.5) for gene expression, (3.6)-(3.19) for cell proliferation and differentiation, (3.20)-(3.29) for bead and reactor scale mass transport — was solved for a time frame of 21 days (equal to the duration of the osteogenic differential experiment) using the ode15s differential and algebraic equation solver available in the MATLAB computing environment [121]. Simulation results include the time profiles of intracellular (Figure 3.1) and extracellular (Figure 3.2) metabolites, gene expression (Figure 3.3), cell counts (Figure 3.4), and radial profile of cell density at the end of the differentiation period (Figure 3.5). Results presented in Figure 3.1, Figure 3.3, and Figure 3.4 were plotted against model predictions and experimental measurements from well-plate cultures (using data presented in Chapter 2). A global sensitivity aiming to assess the significance of the diffusive mass transport coefficients was also performed; sensitivity indices yielded by the analysis are presented in Figure 3.6.

3.3.1. Metabolism

Intracellular metabolite levels start at concentrations specific to mesenchymal stem cells (MSC) and maintain a flat profile until the cells start to differentiate into pre-osteoblasts (PRE), between day 6 and day 7, as shown in Figure 3.1. Next, metabolite concentration increases simultaneously with the fraction of pre osteoblasts (shown in Figure 3.4a), reaching a maximum value between day 9 (*e.g.*, for glutamine) and day 12 (*e.g.*, for glucose). Finally, as cells differentiate further, metabolite levels decrease and settle at osteoblast-specific levels, around day 17.

Compared to the well-plate culture scenario (presented in Chapter 2), in alginate-gelatin bead encapsulated cells (“bioreactor”), metabolites involved in glycolysis and anaerobic catabolism (glucose, pyruvate, and lactate; Figure 3.1a-c) attain peak values later, and the peaks are lower. This effect is produced by the composition of two factors: (1) the plots present concentration averages (over differentiation state and location within the alginate gelatin bead), and cells located closer to the center of the bead experience lower concentrations of glucose in their environment, resulting in lower intracellular levels and

diminished glycolytic activity; (2) the proportion of cells at distinct differentiation states varies with position in the alginate-gelatin bead, with cells that are located closer to the center of the bead entering each of the last two differentiation states (PRE and OBC) later than cells closer to the outer surface of the bead, thus distributing the peak over a larger time frame and flattening it; this, in turn, is caused by a corresponding delay in gene expression (Figure 3.3).

Glutaminolysis (Figure 3.1h) activity is strongly affected by the same trend as glycolysis. In addition, the cells uptake a large portion of the available glutamine in the environment (presented in Figure 3.2), making it impossible to maintain high levels of intracellular glutamine between day 9 and day 16.

With both glycolysis and glutaminolysis registering reduced activity compared with well-plate culture, the metabolites in the TCA cycle show corresponding concentration declines between day 9 and day 12 (citrate, iso-citrate, succinate, and fumarate; Figure 3.1d-g), particularly while pre-osteoblasts (PRE) remain the predominant differentiation state (Figure 3.4a). As more cells terminally differentiate into osteoblasts (OBC), metabolic activity decreases, in agreement with experimental measurements [44], and culture medium metabolite concentrations return to higher values (presented in Figure 3.2).

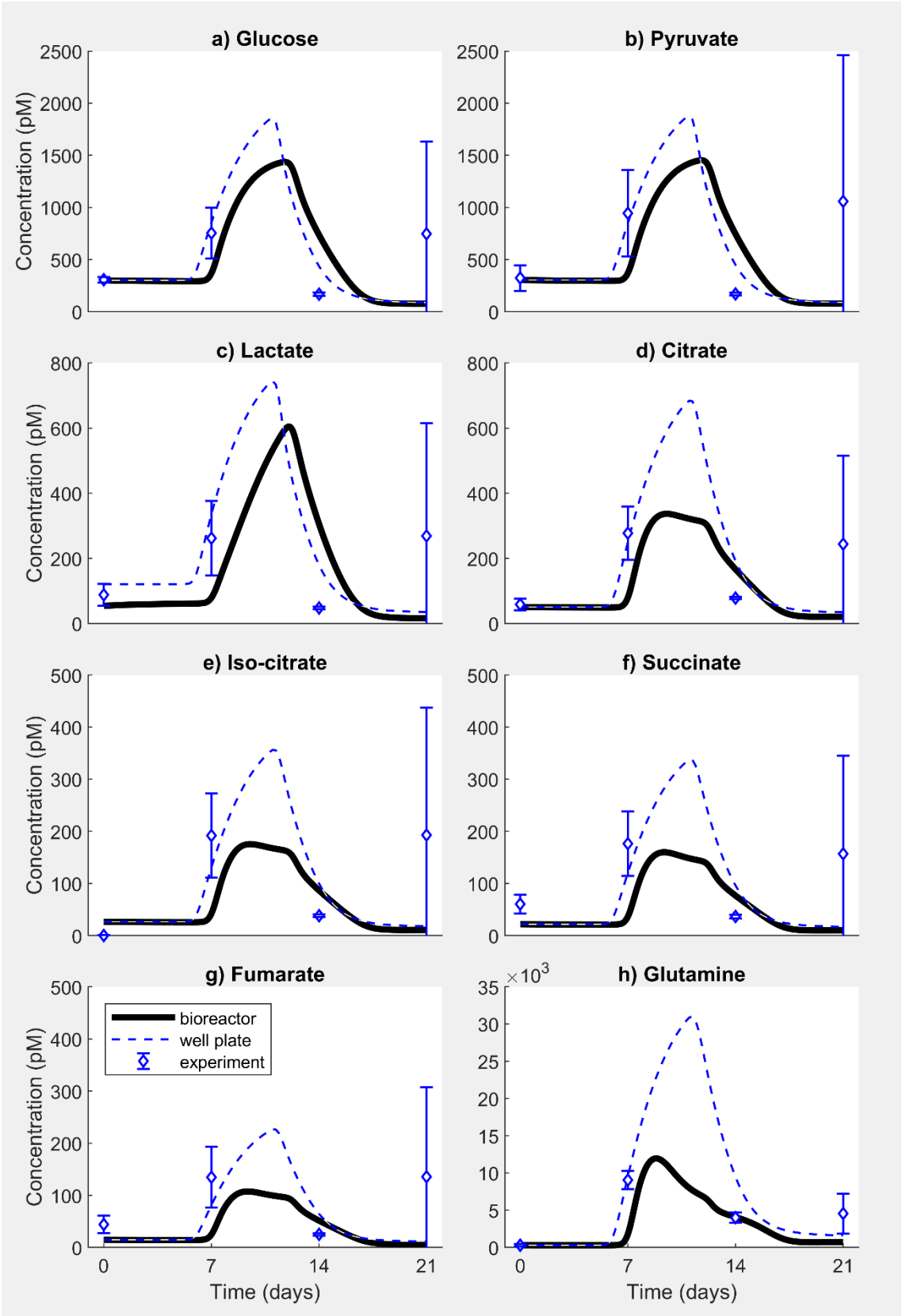

Figure 3.1. Average intracellular metabolite levels during osteogenic differentiation of MSCs; comparison between rotating wall bioreactor (thick solid black line), well plate culture (thin dashed blue line), and experimental data for well plates (blue diamonds for experimental values and vertical blue lines for standard deviation)

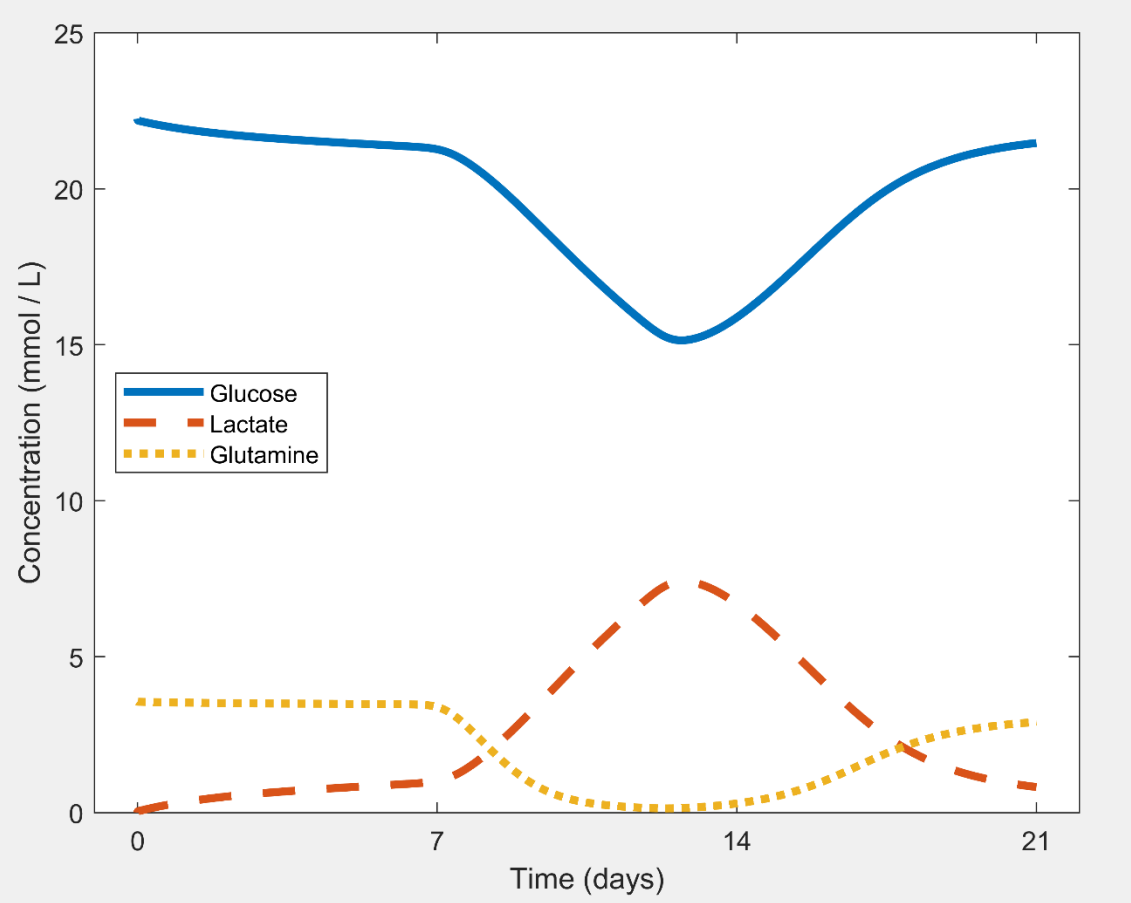

Figure 3.2. Culture medium metabolite levels during osteogenic differentiation of MSCs

3.3.2. Gene expression

Gene expression results are reported as average values (over cell differentiation state and location inside the alginate gelatin bead). Profiles of the average gene expression values (Figure 3.3) show an increase in *Runx2* activity around day 5 denoting the differentiation of MSCs into pre-osteoblasts, followed by an increase in *osteonectin* expression around day 11, corresponding to the formation of osteoblast cells from pre-osteoblasts.

For both genes considered in this study, their activation in alginate-gelatin bead encapsulated cells is slightly delayed (by about 1 day) compared to well plate cultures (Figure 3.3). The observed delay is correlated with a similar outcome for dexamethasone concentration as it diffuses from the culture medium inward through the hydrogel bead.

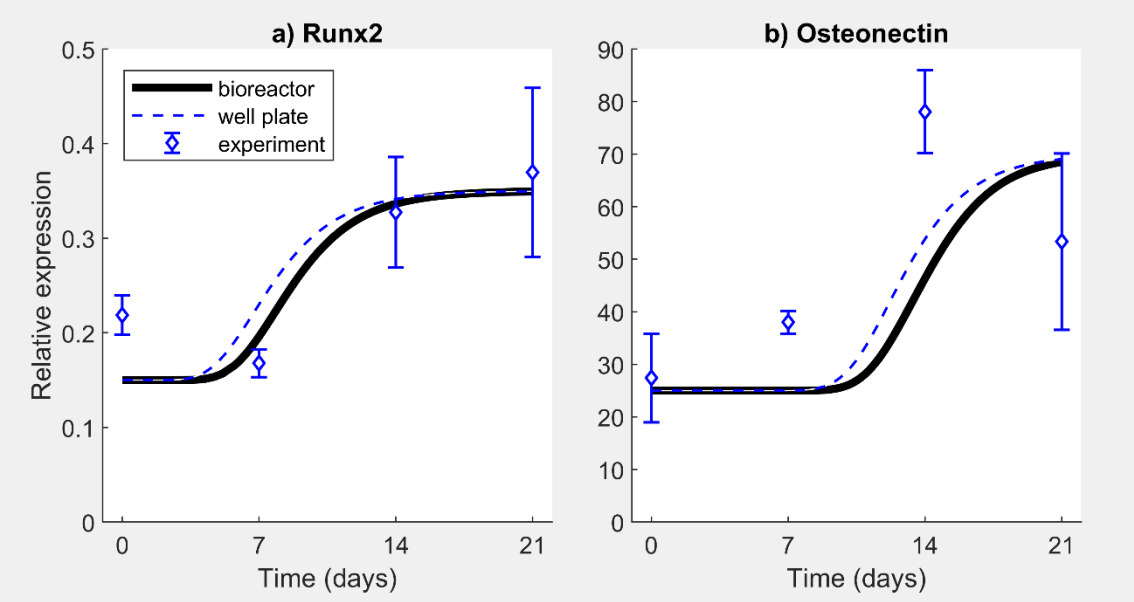

Figure 3.3. Average relative expression of genes during osteogenic differentiation of MSCs; comparison between rotating wall bioreactor (thick solid black line), well-plate culture (thin dashed blue line), and experimental data for well plates (blue diamonds for experimental values and vertical blue lines for standard deviation)

3.3.3. Cell counts and density distribution

Figure 3.4a shows the cell count evolution during the simulation. The number of mesenchymal stem cells (MSCs) increases until about day 7, which marks the beginning of differentiation into pre-osteoblasts (PRE); next, the number of pre-osteoblasts increases gradually until about day 11, when differentiation into osteoblasts (OBC) exceeds cellular division for pre-osteoblasts. Finally, the osteoblast count increases gradually as they become the predominant cellular differentiation state after day 18. The total cell count shows a moderate rate of growth for MSCs, an accelerated rate during the pre-osteoblast peak, and a low expansion rate for osteoblasts.

Figure 3.4b compares the total cell count per bead for alginate-gelatin bead encapsulated cells with the total cell count per well plate (for static well plate cultured cells). The cell count is visibly lower for encapsulated cells, due to lower concentrations of intracellular metabolites toward the center of the alginate-gelatin bead, which correlates with lowered energy production rate and lower cellular division rate. It is important to note that the model presented in this chapter uses cell density, not cell count as part of the mathematical description. The total cell numbers plotted in Figure 3.4 (thick black line) are the total cell count per alginate-gelatin bead and were calculated as described by equation

(3.10). Even though Figure 3.4b suggests that well-plate cultures (dashed blue line labeled “reference”) produce more cells that bead-encapsulated ones, the entire culture volume should also be considered instead of just a single bead. When comparing the two bioprocesses, the rotating wall bioreactor exhibits a cellular density (expressed as the number of cells per culture volume unit) about four hundred times larger than the well plate culture.

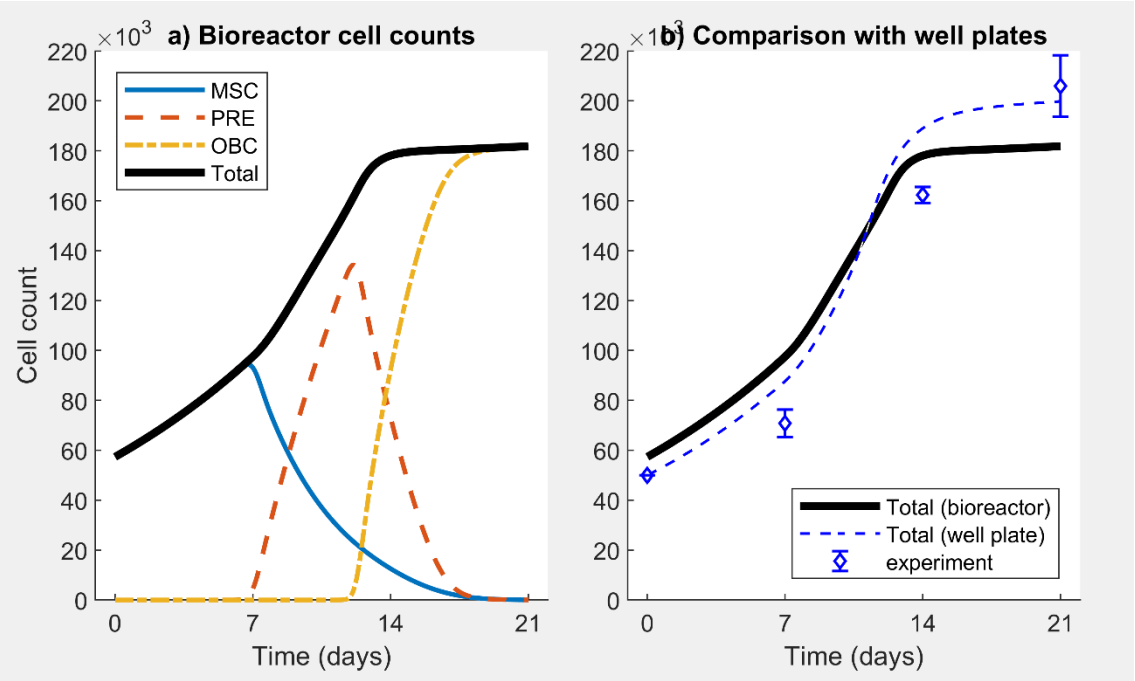

Figure 3.4. Averaged cell counts during osteogenic differentiation of MSCs; a) total cell count (thick black line) and partial counts for each differentiation state (thin colored lines); b) comparison between total cell counts for the rotating wall bioreactor (thick solid black line), well plate culture (thin dashed blue line), and experimental well plate data (blue diamonds for experimental values and vertical bars for standard deviation)

The similar trends observed for the two processes (in Figure 3.1, Figure 3.3, and Figure 3.4) can be justified on the basis of similar extracellular conditions for the two processes: while the perfusion flowrate through the rotating wall bioreactor ensured that culture medium was continuously being replenished, culture medium exchange was performed manually for the well plate culture every 2–3 days, to prevent the accumulation of toxic waste products such as lactate.

A consequence of encapsulating cells in alginate gelatin beads (or other materials) is that cells at the center of the bead will generally experience more severe environmental conditions — *i.e.*, lower nutrient concentrations and higher waste levels. Figure 3.5 shows the radial profile of the cellular density in the bead

at the end of the differentiation process (day 21); in this case, the cell density is about 2.5% lower in the center than at the outer surface (for 2.3 mm diameter beads).

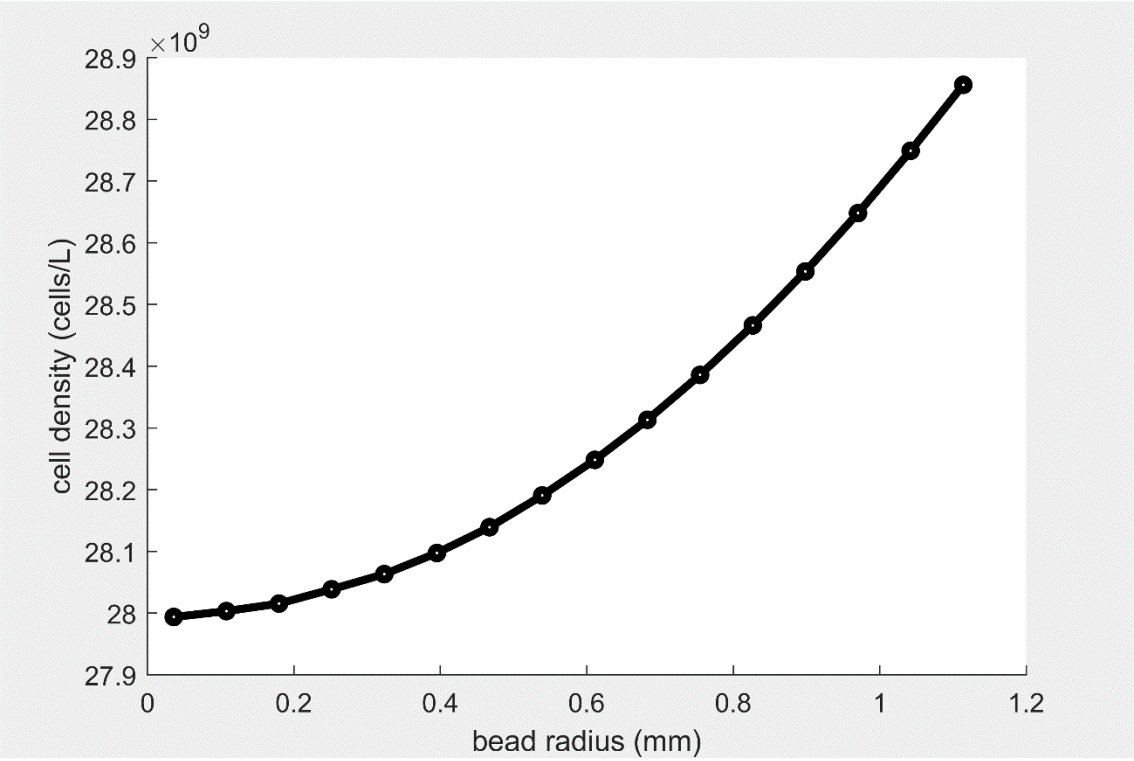

Figure 3.5. Calculated radial cell density distribution in the alginate gelatin bead at day 21

3.3.4. Sensitivity analysis

Total sensitivity indices were computed for 13 factors and two main responses (total cell count per alginate gelatin bead, and osteoblast fraction) evaluated at days 7, 14, and 21 of the differentiation process. The factors include the 10 parameters that were deemed significant by the global sensitivity analysis shown in chapter 2.2.2, whose values were allowed to vary between 50% and 150% of their nominal value, and the diffusion coefficients for glucose, lactate, and glutamine, whose values were allowed to vary between 10% and 150% — the larger relative deviation towards lower values was allowed considering that an overestimation of the diffusion coefficients is more dangerous for the cultured cells, whereas an underestimation would mean that conditions in the bioreactor are milder than considered by the model. A total of 14000 simulations were performed to complete the sensitivity analysis (see 0 for convergence plots).

Within the uncertainty of the thirteen parameters that were selected for the global sensitivity analysis, none have sensitivity index values above the 0.1 significance threshold for the response of the total cell count at the end of the process (Figure 3.6a).

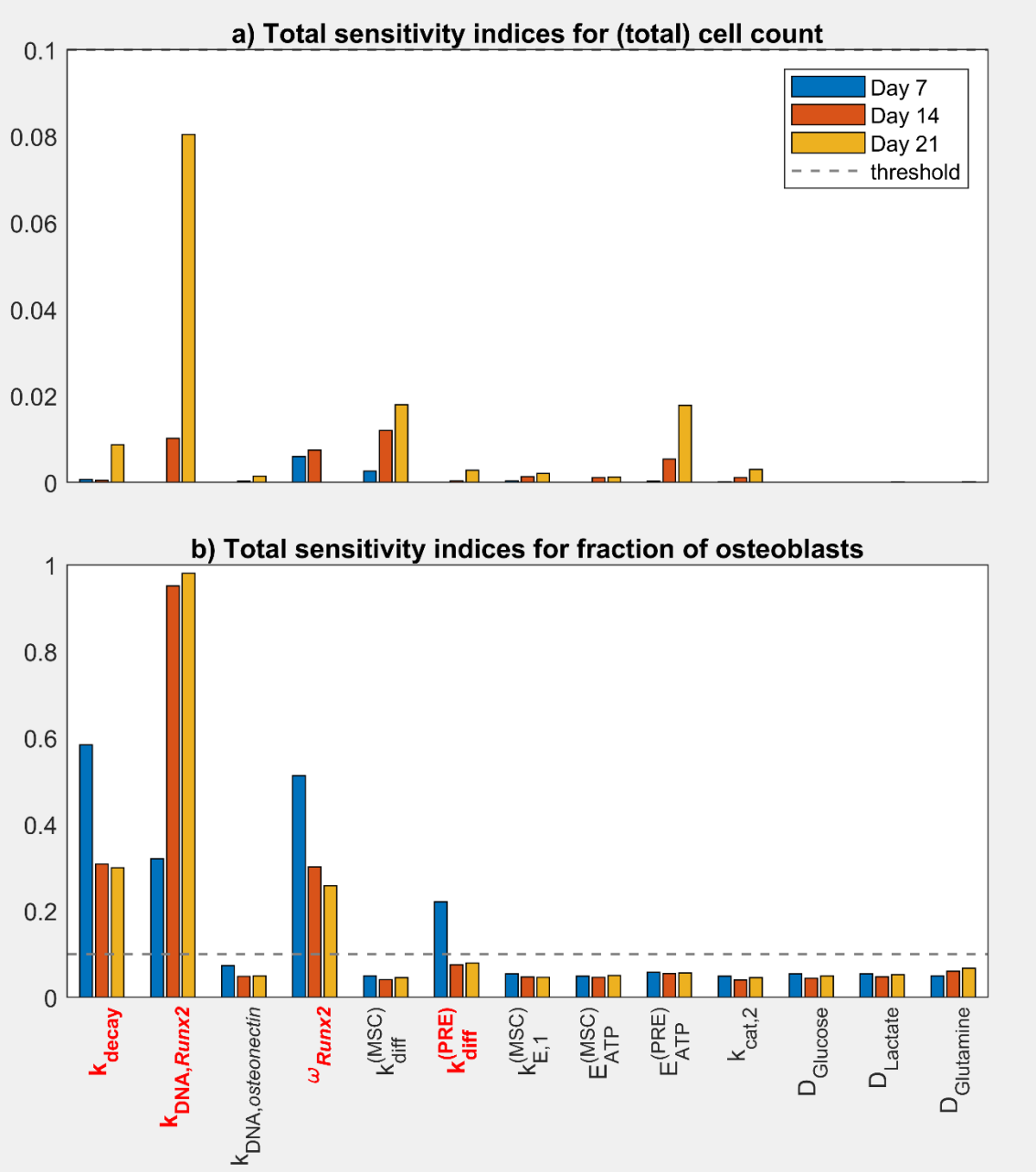

Figure 3.6. Global sensitivity analysis results: sensitivity indices for (a) total cell count and (b) osteoblasts fraction — names of factors with total sensitivity indices above the 0.1 threshold are indicated with bold red font

Four of the total sensitivity indices for the response of osteoblast fraction exceed the significance threshold (RNA decay rate, DNA binding constant for the activation of the *Runx2* gene, base expression of *Runx2* in mesenchymal stem

cells, and differentiation constant controlling the specialization of PRE cells into OBC), indicating that the uncertainty in these parameters' values propagate into the variance of the observed values for the osteoblast fraction response (Figure 3.6b).

Note that all diffusivity parameters ($\mathcal{D}_{Glucose}$, $\mathcal{D}_{Lactate}$, and $\mathcal{D}_{Glutamine}$) have total index values below the threshold, indicating that the uncertainty in their values does not significantly impact the variance of the mathematical model's prediction.

3.3.5. Discussion

Other mathematical models for culture dynamics of stem cells including cell death and differentiation phenomena have been published in the scientific literature; Chen *et al.* have described cell differentiation by assigning each (differentiation) state a separate compartment in the mathematical model [42]. Herein, each of the differentiation states are also allocated different compartments, but the model describes stem cell dynamics with greatly increased detail and accuracy at every step of the differentiation process. The use of population balance equations enables the quantification of cell population densities (or counts) as well as the distribution (heterogeneity) of those populations among the cell cycle phases and spatially within the alginate-gelatin beads. Cell differentiation is not only described by the mathematical model, but it is also precisely located within phase G (Gap 1) of the cell cycle [85,89]. The mathematical model of MSC osteogenic differentiation provides a detailed description of the underlying biological phenomena and advances the possibility of obtaining high-quality engineered bone tissue through culture optimization. Achieving such a feat solely by *in-vitro* experimentation entails relatively slow progress at high costs. On the other hand, the mathematical model is potentially useless without practical confirmation and at least some amount of experimentation is required for informing and supporting modeling decisions, refining parameter values, and validating the mathematical model before rendering it ready for clinical application.

Population balance models (PBM) have previously been used in mathematical models for stem cell cultures. Wu *et al.* used a PBM to describe

cell aggregation in spinner flask cultures [55]. This work utilizes PBMs differently and employs them for a detailed description of cell cycle phase heterogeneity, enhanced by differentiation state and spatial heterogeneity; in this work metabolism and cell growth are linked directly, whereas Wu *et al.* focused on the transport of oxygen as the limiting factor for stem cell expansion. Bartolini *et al.* used a PBM for the proliferation of stem cells in suspension reactors [56], but were focused on bioreactor operation and dynamics, whereas this work emphasizes intracellular metabolism and gene expression, and differentiation and mass transport inside alginate-gelatin beads. The two PBMs also differ in the choice of the independent distribution variable: Bartolini *et al.* distributed the cell cycle over the mass of the cells, whereas this work distributes each cell cycle phase over a cell-cycle-phase-specific cyclin, or DNA. The PBM used in this work has similar features to that used for modeling cell-cycle-phase-specific chemical leukemia treatment [54], and for cell-cycle-phase-specific antibody production rates [124] but differs from both referenced works by including intracellular metabolism, gene expression, cell differentiation, and bead and reactor level mass transport.

Global sensitivity analysis was performed on a subset of the parameters of the model; the newly introduced diffusivity parameters were analyzed together with the 10 most significant parameters that were identified in the well plate culture scenario (see Figure 3.6). The most significant parameters are still the ones related to gene expression: RNA decay rate, DNA binding interaction, and differentiation constants. While the newly added parameters were not deemed significant by the global sensitivity analysis, it is possible that this result is valid only for alginate-gelatin beads up to a certain size, above which diffusion transport limitations affect the outcome of the process. The radius of the beads themselves was not part of the sensitivity analysis, because the experimental technique produced beads with a narrow size distribution [114]; furthermore, even larger deviations (± 10%) from the nominal 2.3 mm bead diameter did not produce significant changes in the predictions of the model. By experimentation with running additional simulations, it was found that a bead diameter of about 4.5 mm leads to a large decrease in cell counts. The threshold is probably lower in practice, as the model in its current form does not properly account for potentially

increased death rates among the cells closer to the center of the bead caused by a combination of toxic lactate concentrations and hypoxia. This suggests the existence of an optimal bead radius for alginate-gelatin beads used in the osteogenic differentiation of MSCs, with a bead size that balances the potential benefit of using larger beads (enables the use of higher flowrates and recirculation of a fraction of the culture medium) and the drawbacks (higher cell mortality).

3.4. Mathematical model validity assessment

The mathematical model presented herein has a high degree of complexity and sophistication, which provides copious opportunity for conceptual mistakes to slip in. Although the model was examined carefully — both in the formulation of its equations and using global sensitivity analysis — several computer simulations were designed and performed to confirm the qualitative behavioral validity of the mathematical model with respect to several physical variables. In all case studies detailed below, the model output is biologically correct.

The mathematical model presented in this chapter does not include a description of oxygen transport, nor its contribution to intracellular metabolism. Although an experimental analysis showed that cells were not affected by hypoxia under the investigated culture conditions and the results presented herein have been confirmed experimentally [115], some of the *in-silico* results presented below (such as high initial cell density or the use of larger alginate-gelatin beads) might not fully capture the severity of the environmental conditions that would be experienced by their biological counterpart (*e.g.*, hypoxia).

3.4.1. Model response to initial cell density variations

Since the aim of the experimental procedure, which is represented by the mathematical model in this chapter, is to generate osteoblasts that can be used to treat bone defects in clinical settings, it is crucial to have sufficient suitable cells for an effective treatment. Since cell count is directly proportional to cell density (expressed as count of cells per unit volume, in units of cells per liter), this variable is of great practical importance.

Cell density at the end of the osteogenic differentiation process (day 21) is one of the outputs of the model, but the result of the calculation depends on the initial value of this variable, corresponding to the cell density in the alginate-gelatin bead when the beads are formed. Since this variable can be adjusted experimentally, it is meaningful to assess the effects of adjusting it.

The initial cell density has been labeled ρ_0 in this chapter. Apart from the base value of 9 billion cells per liter, the simulation was repeated for two other values, at about half and double the base cell density (4, and 20 billion cells per liter, respectively).

Regarding the potential effects of changing the cell density, when the number of cells increases within a finite volume, they should uptake nutrients at a higher rate, leading to a lower nutrient concentration level in their environment, i.e., the alginate-gelatin bead. In turn, this would hinder the ability of the cells to absorb nutrients from the environment, causing a decrease in intracellular metabolite concentrations levels (compared with a baseline level). In contrast, when the number of cells is lower, they should uptake fewer nutrients, deplete their resources slower, and would exhibit higher intracellular metabolite concentration levels. Figure 3.7 confirms these predictions for all modelled intracellular metabolites.

The effect of changing the initial cell density on the culture medium compartment (the bulk liquid in the reactor, Figure 3.8) is analogous to the intracellular picture: larger densities are correlated with higher total uptake rates and result in lower metabolite levels overall for glucose and glutamine. Culture medium lactate responds in the opposite manner, as higher intracellular metabolism (achievable for lower cell density values) leads to increased lactate production, which consequently increases extracellular lactate concentration.

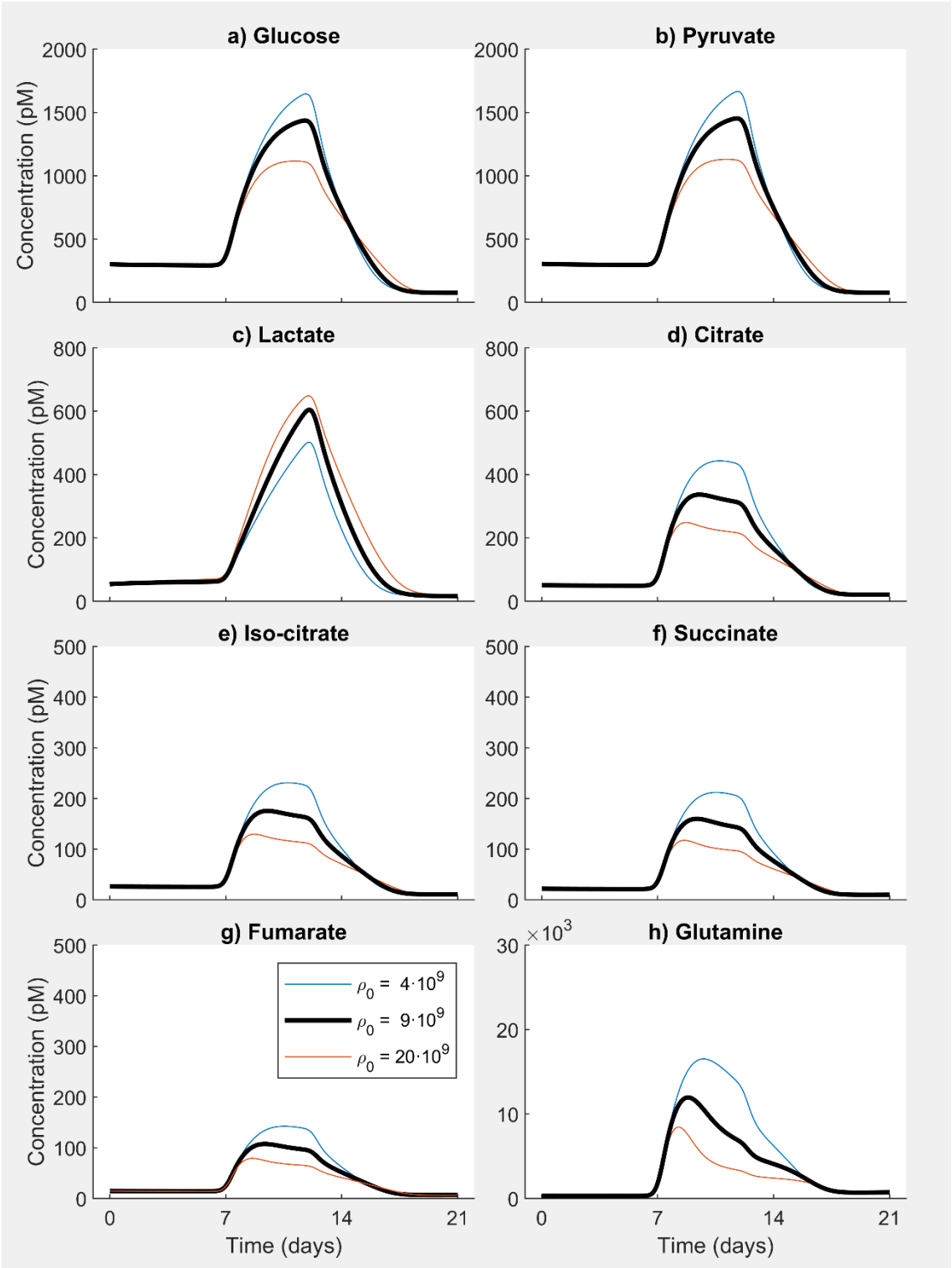

Figure 3.7. The response of intracellular metabolism to initial cell density (ρ_0) variations

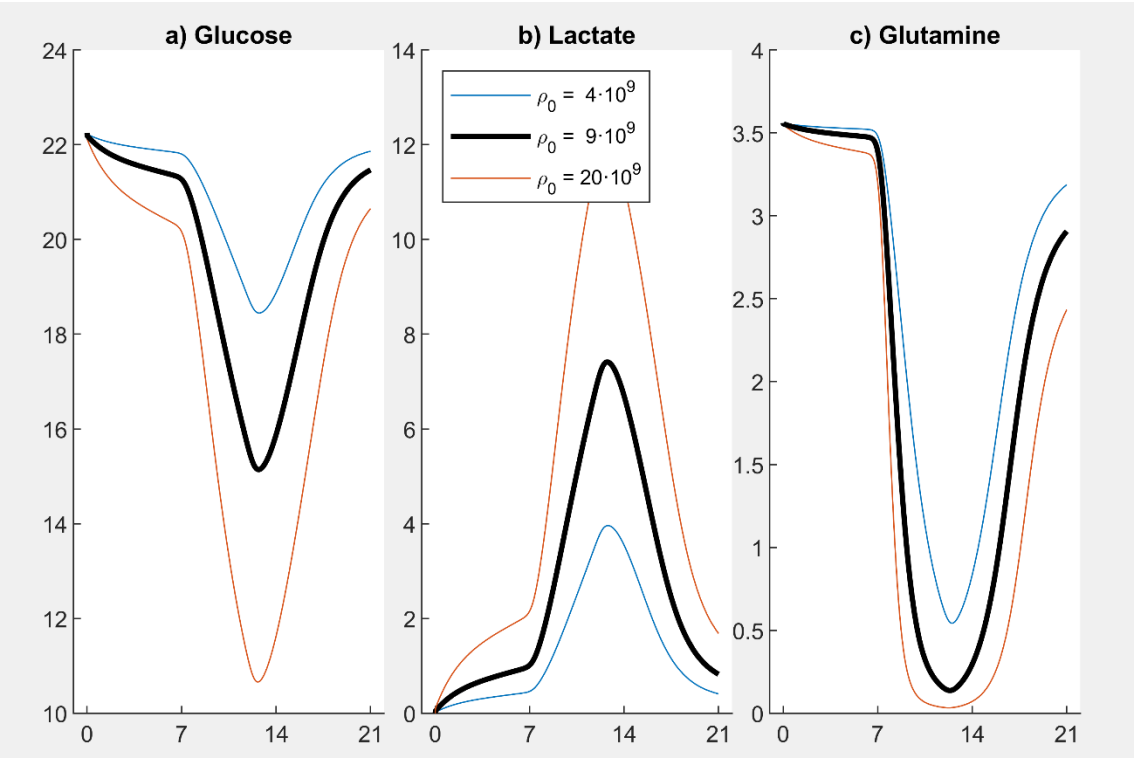

Figure 3.8. The response of extracellular (bulk liquid) metabolite levels to initial cell density variations

The effects of initial cell density on gene expression are negligible (Figure 3.9), since metabolism and gene expression are disjoint behaviors, with the latter being strongly connected only with the differentiation agent (dexamethasone) that initiates the osteogenic differentiation sequence.

Except for situations where higher cell densities cause cell death by locally depleting the nutrients in the environment, increasing the (initial) cell density should always lead to higher cell counts. The predictions of the mathematical model agree with this result (Figure 3.10).

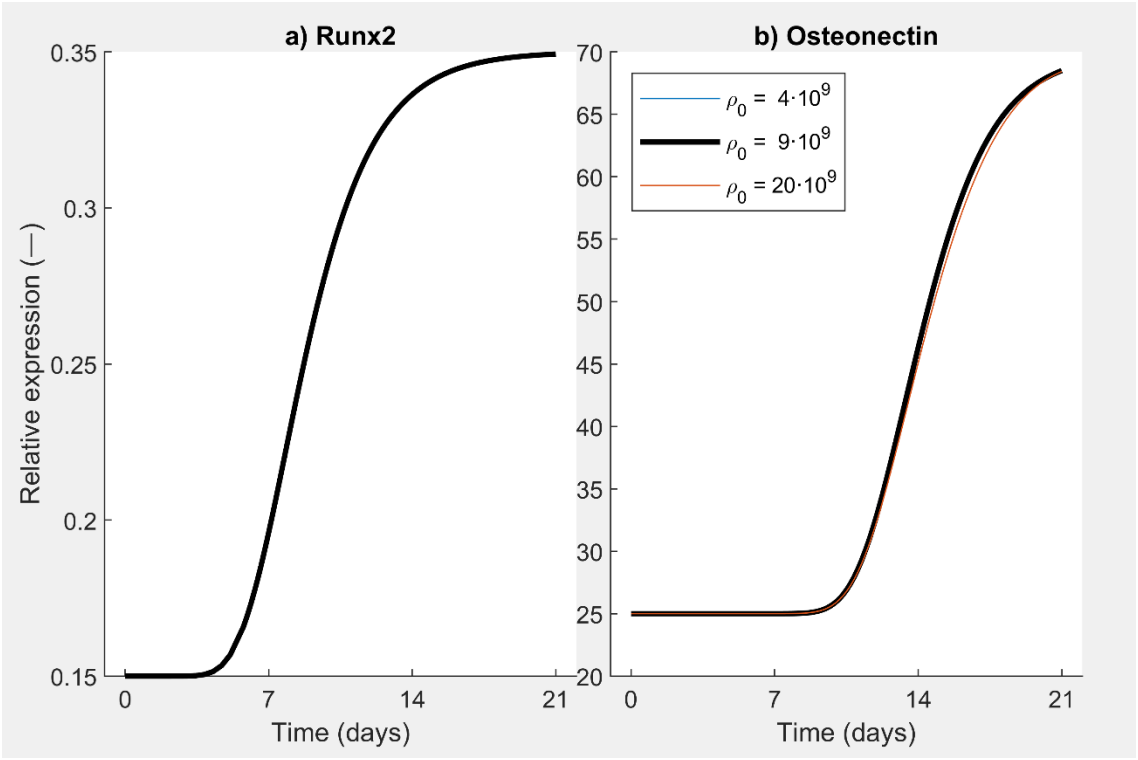

Figure 3.9. The response of relative gene expression to initial cell density (ρ_0) variations

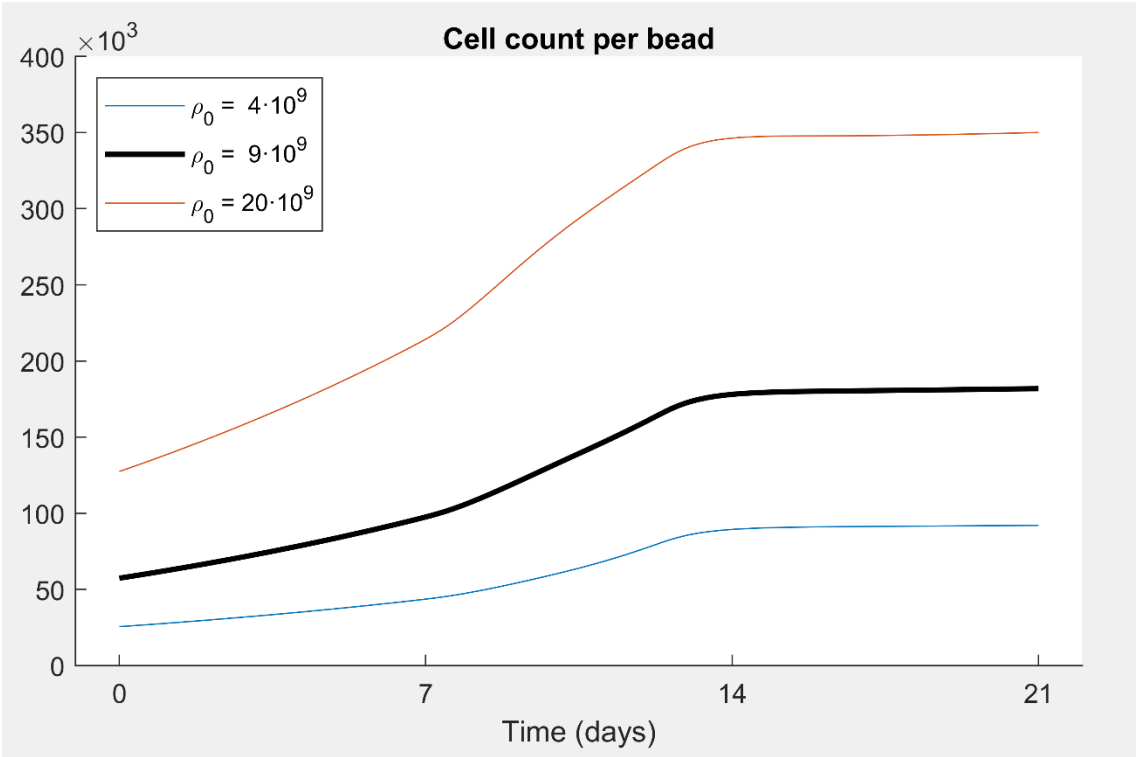

Figure 3.10. The response of total cell population per alginate-gelatin bead to initial cell density (ρ_0) variations

Figure 3.11 conveys the effect of changing the initial cell density on the final (day 21) cell density. The resulting radial cell density profiles agree with

expectations: lower initial cell density leads to lower final density. Furthermore, at higher cell density, the total nutrient uptake rate grows, causing cells that are closer to the center of the alginate-gelatin bead to experience more severe conditions compared to those closer to the outer surface of the bead (as the cells remove nutrients as they traverse the bead radius). In conclusion, higher cell densities accentuate the percentual difference between the surface and the center of the bead.

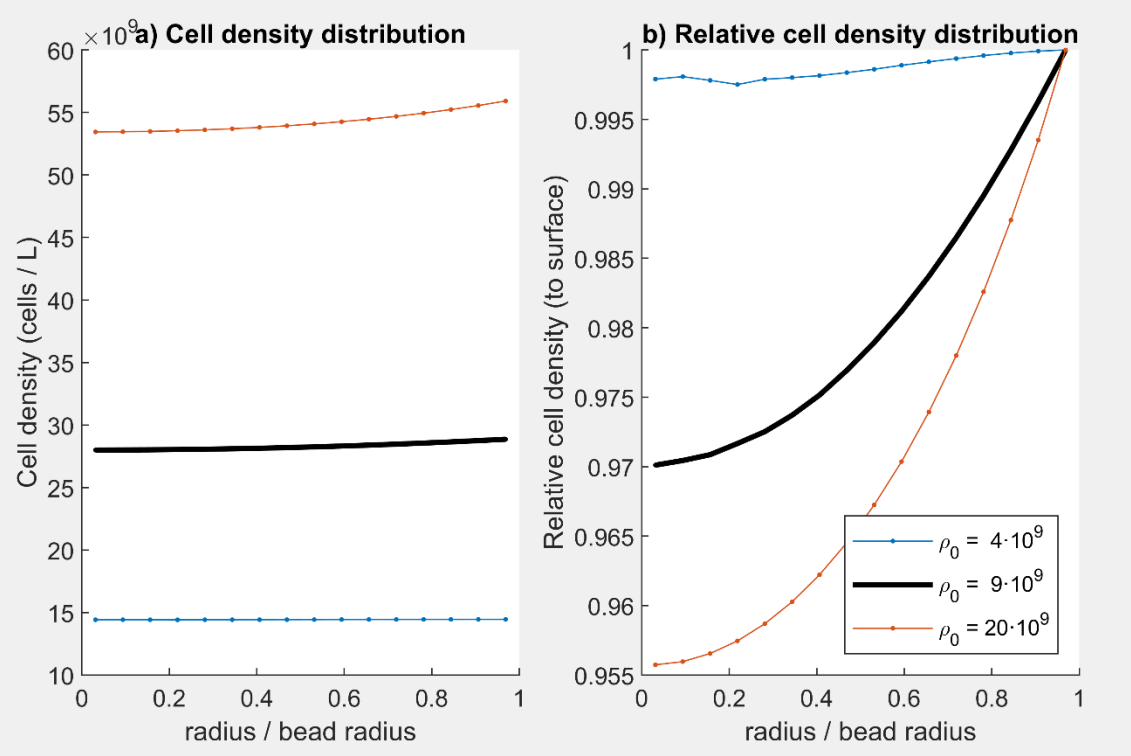

Figure 3.11. The response of the radial cell density distribution at day 21 to initial cell density (ρ_0) variations

These *in-silico* results suggest that an initial cell density of twenty billion cells per liter would improve the final cell count (Figure 3.10) without affecting the quality of the produced cells, as evaluated by their gene expression (Figure 3.9). However, while the outcome is still qualitatively correct, it might not be quantitatively accurate: (a) the death rate of cells could be higher than the estimated value at high waste concentrations; (b) although there is no direct connection between the selected metabolic pathways and the two genes, it is possible that an indirect link could become more active under those conditions. Furthermore, while the mathematical model does prohibit cell densities that are mathematically infeasible (*i.e.*, when the total volume of the cells exceeds the

available local space inside the alginate-gelatin bead), it does not quantify the effect of cell density on the transport of extracellular metabolites (*i.e.*, the values of the diffusion coefficients for metabolites are kept constant, irrespective of the cell density).

3.4.2. Model response to nutrient concentration variations

Intracellular metabolism is an essential component of the mathematical model (because it controls the proliferation rate of the cells) as well as one of the elements of novelty contributed by the work presented in this thesis. Although intracellular metabolite concentration levels are controlled by molar balance equations (and model parameters), their dynamics are also dependent on extracellular conditions.

In addition to the base case scenario (where the culture medium was prepared using a solution with 25 mmol/L glucose and 4 mmol/L glutamine), simulations for two other scenarios were investigated: with lower concentrations of nutrients (15 mmol/L glucose and 2 mmol/L glutamine) and with higher nutrient concentrations (30 mmol/L glucose and 6 mmol/L glutamine). The effects of nutrient concentration on intracellular and extracellular metabolism, gene expression, cell counts, and radial cell density distribution within the alginate-gelatin bead are presented in the figures below; the numbers (expressed in mmol/L) in the legend associate each result (line plot) with its corresponding scenario (Glc stands for glucose, and Glu stands for glutamine).

When changing both the glucose and glutamine concentrations in the culture medium, the reaction of the intracellular metabolism of the cells is predictable and reasonable: higher extracellular levels cause intracellular levels to rise as a result (Figure 3.12).

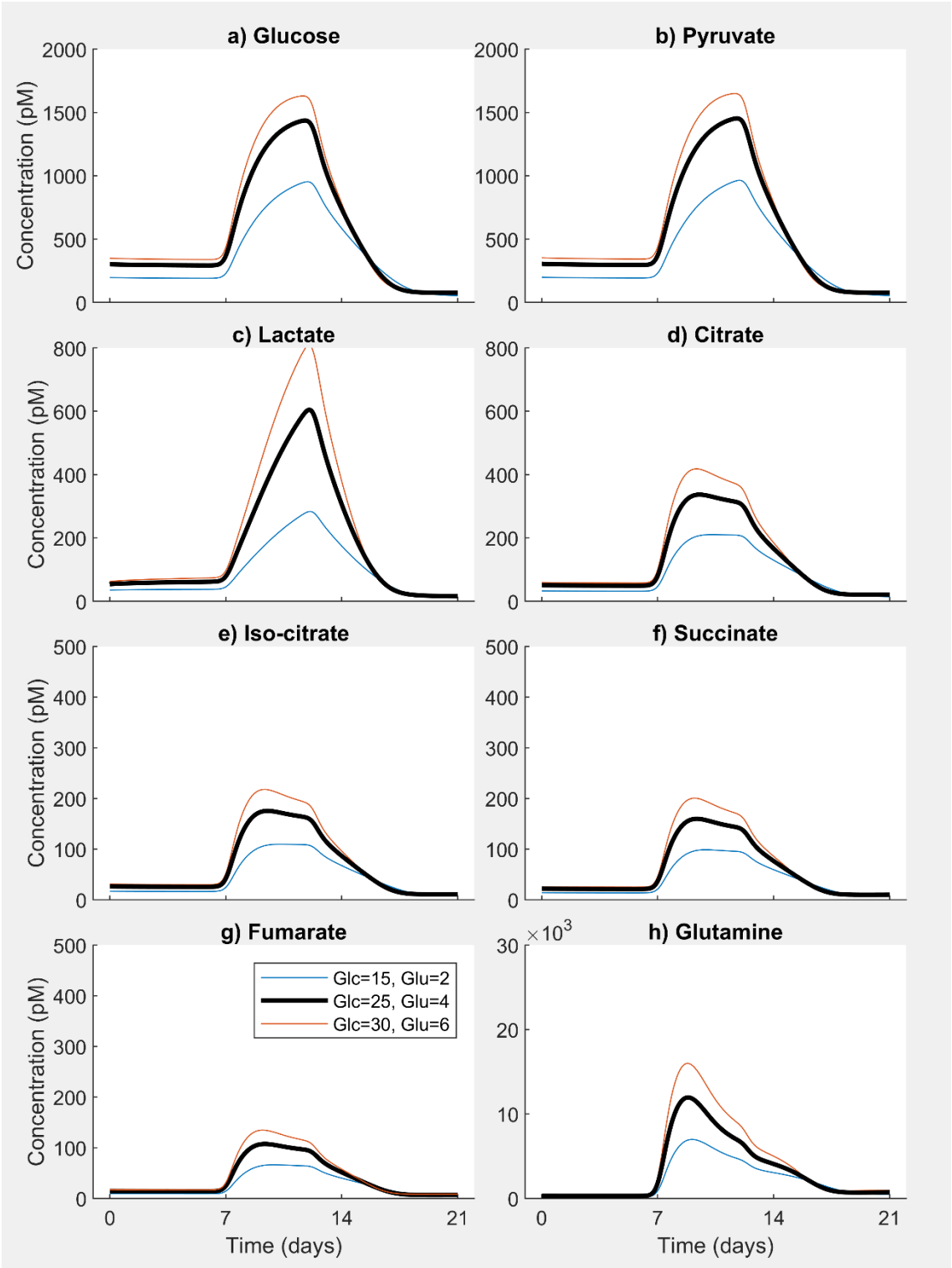

Figure 3.12. Response of intracellular metabolism to variations in nutrient concentration in the culture medium

Extracellular metabolite concentration levels follow similar trends to the base case scenario but are affected by their initial values; the general trend is preserved, and the entire temporal profile rises and lowers depending on the initial concentration (Figure 3.13). The production rate of lactate indirectly

depends on the concentrations of the two nutrients: when lower concentrations are used, intracellular reaction rates and metabolic levels are reduced, leading to overall decreased lactate levels in the culture medium.

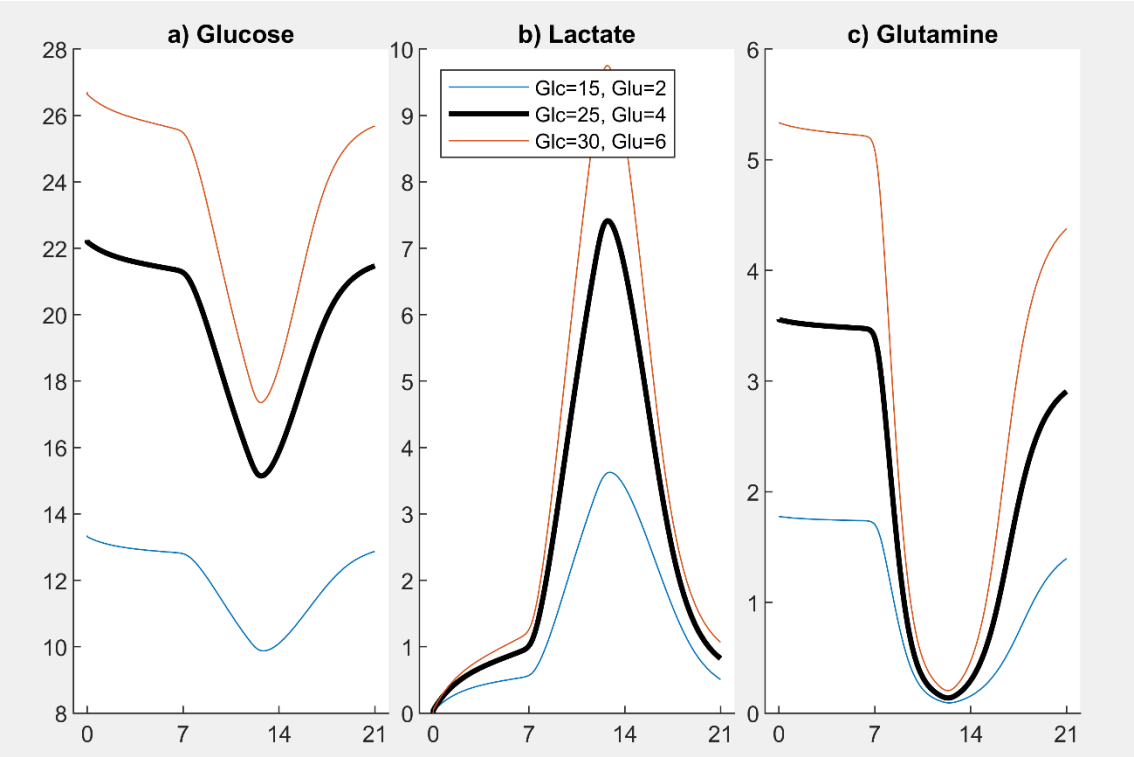

Figure 3.13. The response of extracellular (bulk liquid) metabolite levels to variations in nutrient concentration in the culture medium

Gene expression is largely unaffected by changes in extracellular metabolite concentration (Figure 3.14). The slight delay in *osteonectin* expression is correlated with longer cell cycle duration, which results in a marginally higher percentage of mesenchymal stem cells in the culture, lowering the average values (since they only express *osteonectin* at a basal level).

Figure 3.15 shows the temporal evolution of the total cell count (per alginate-gelatin bead). As expected, an environment rich in nutrients leads to a higher cell count at the end of the process.

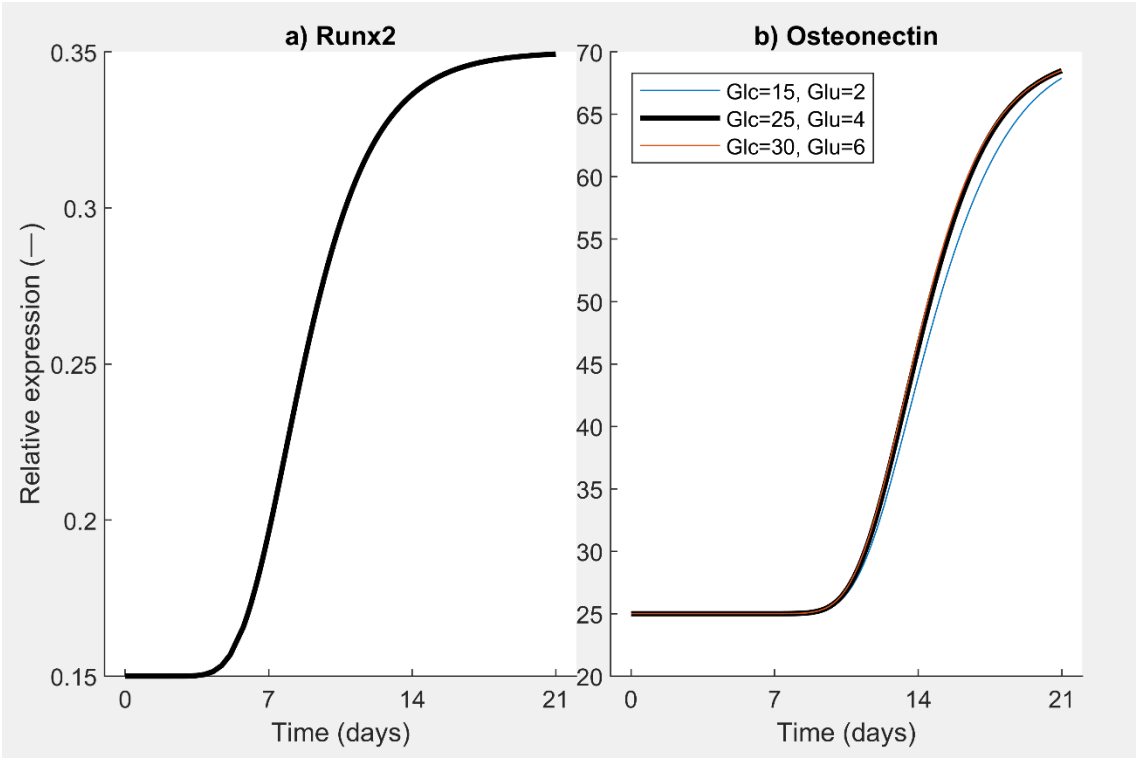

Figure 3.14. The response of relative gene expression to variations in nutrient concentration in the culture medium

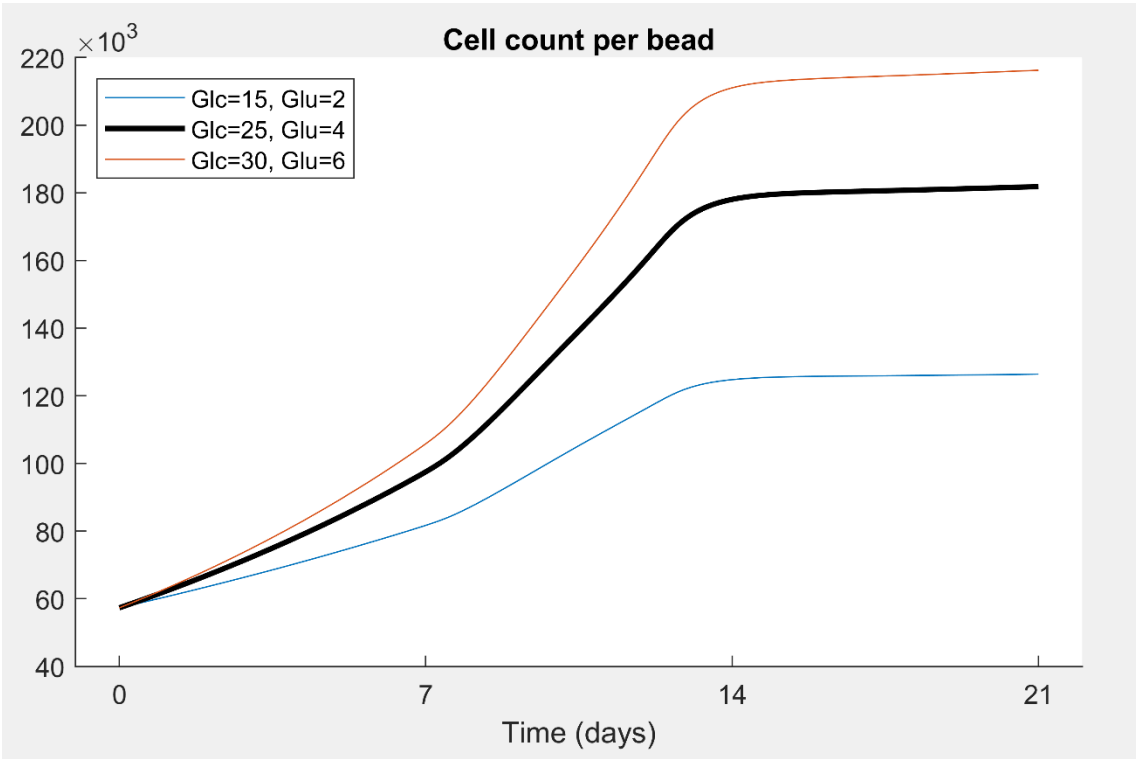

Figure 3.15. The response of total cell population per alginate-gelatin bead to variations in nutrient concentration in the culture medium

The total cell count (shown in Figure 3.15) is directly proportional to the total cell density (shown in Figure 3.16). By analogy with the total cell count

outcome, decreasing the level of nutrients in the culture medium lowers cell density. Nevertheless, when cell density is higher inside the alginate-gelatin bead, it is also less uniform (*i.e.*, the difference in cell density between the center of the bead and the outer surface is highest at high cell density, which is favored by increased nutrient levels in the culture medium).

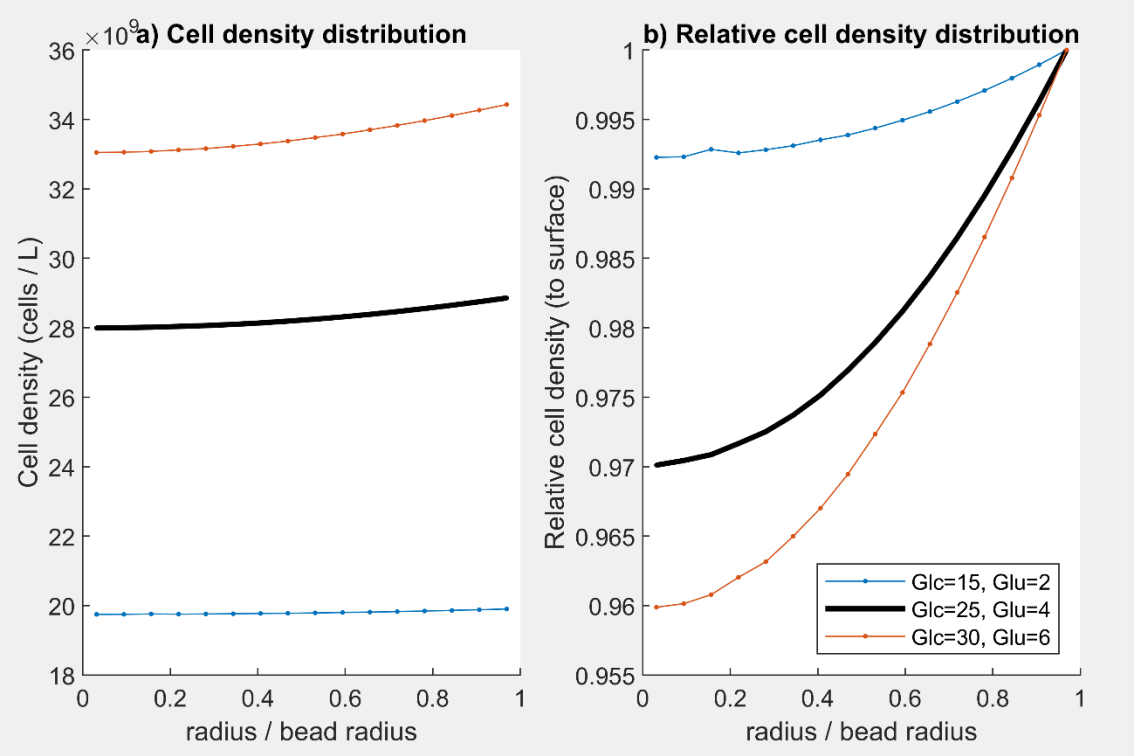

Figure 3.16. The response of the radial cell density distribution at day 21 to variations in nutrient concentration in the culture medium

The predominant effect of increasing the nutrient concentration being fed to the rotating wall bioreactor is higher cell proliferation, with minor differences in phenotype (intracellular metabolism and gene expression are largely unaffected at day 21 of the differentiation process). These results suggest that using a higher nutrient concentration is preferrable. However, the availability of a concentrated culture medium mixture might be limited and, crucially, the purpose of cellular differentiation is to transform the mesenchymal stem cells into osteoblasts that can be used in clinical applications. If a higher cell count is desirable, it is likely to be more useful to obtain the required cell count in the previous experimental stage (*i.e.*, mesenchymal stem cell expansion).

3.4.3. Model response to increasing lactate concentrations in the culture medium

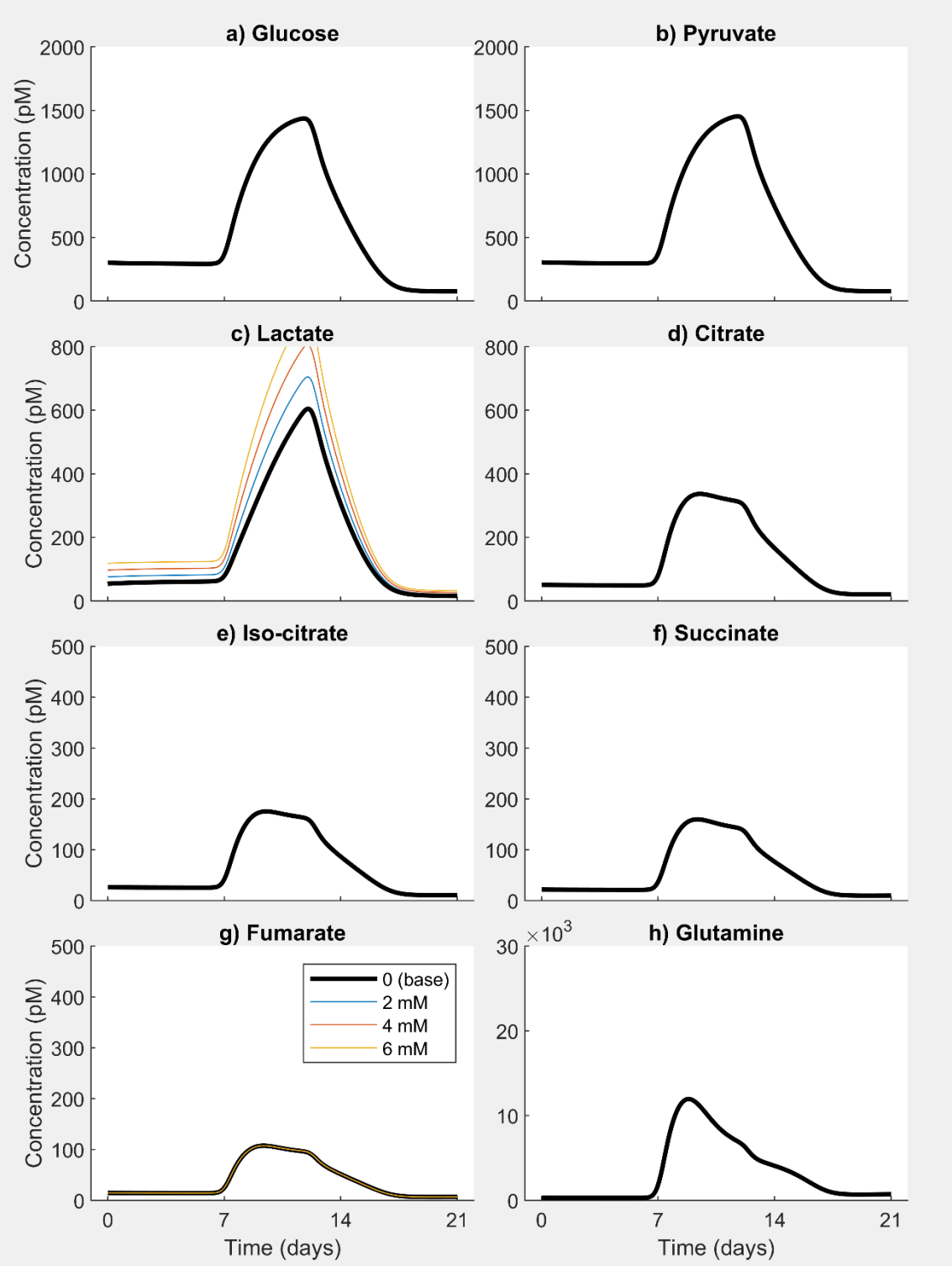

Figure 3.17. Response of intracellular metabolism to variations in lactate concentration in the culture medium

The regular culture medium fed to the bioreactor does not contain lactate, because it is one of the waste products of the process. Three additional scenarios

have been investigated, with progressively larger lactate concentrations in increments of 2 mmol/L. When lactate is more concentrated in the extracellular compartment, its evacuation from the cell is hindered and the concentration of intracellular lactate rises (Figure 3.17c). All other intracellular metabolites are not influenced by extracellular lactate levels. Although the expected biological response includes changes in the levels of other metabolites, the mathematical model cannot accurately replicate this result using the small subset of metabolites that it incorporates, and the mathematically reasonable prediction is likely not biologically accurate for the other 7 metabolites (Figure 3.17, subplots a, b, d-h).

Extracellular lactate concentration levels also rise the more lactate is fed into the reactor as part of the culture medium, leaving glucose and glutamine levels unaffected (Figure 3.18).

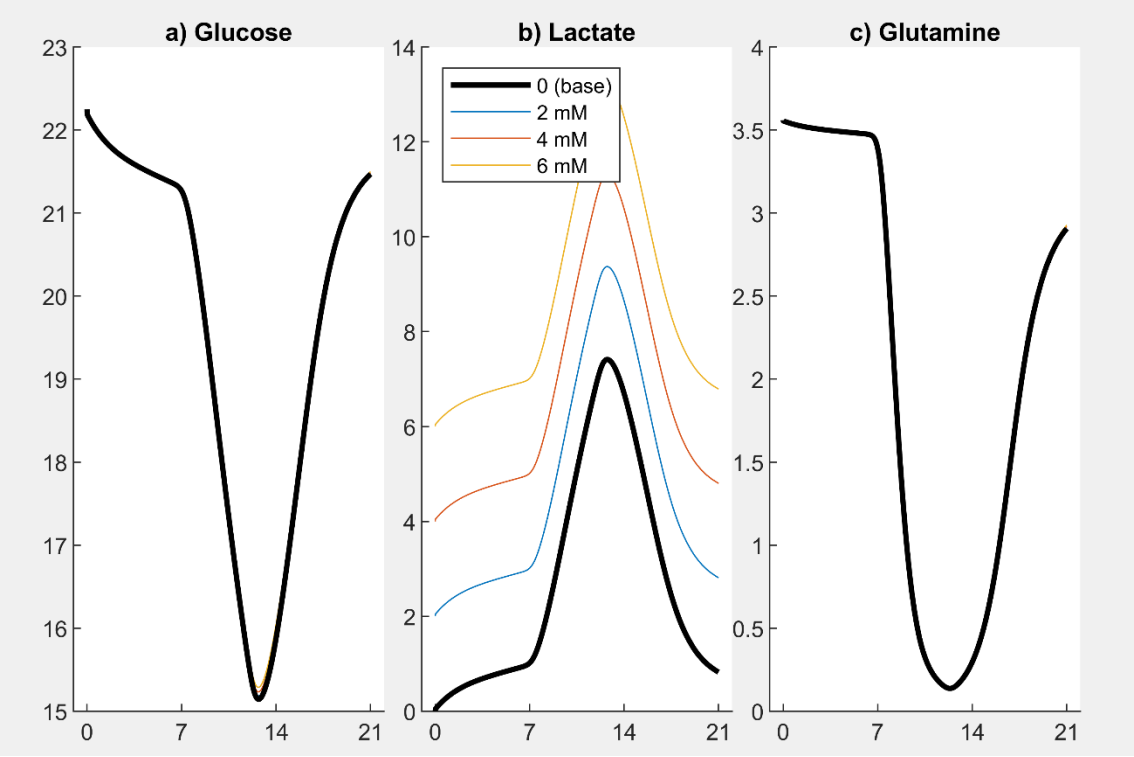

Figure 3.18. Response of extracellular (bulk liquid) metabolite levels to variations in lactate concentration in the culture medium

Gene expression is not affected by the increase in extracellular lactate (Figure 3.19).

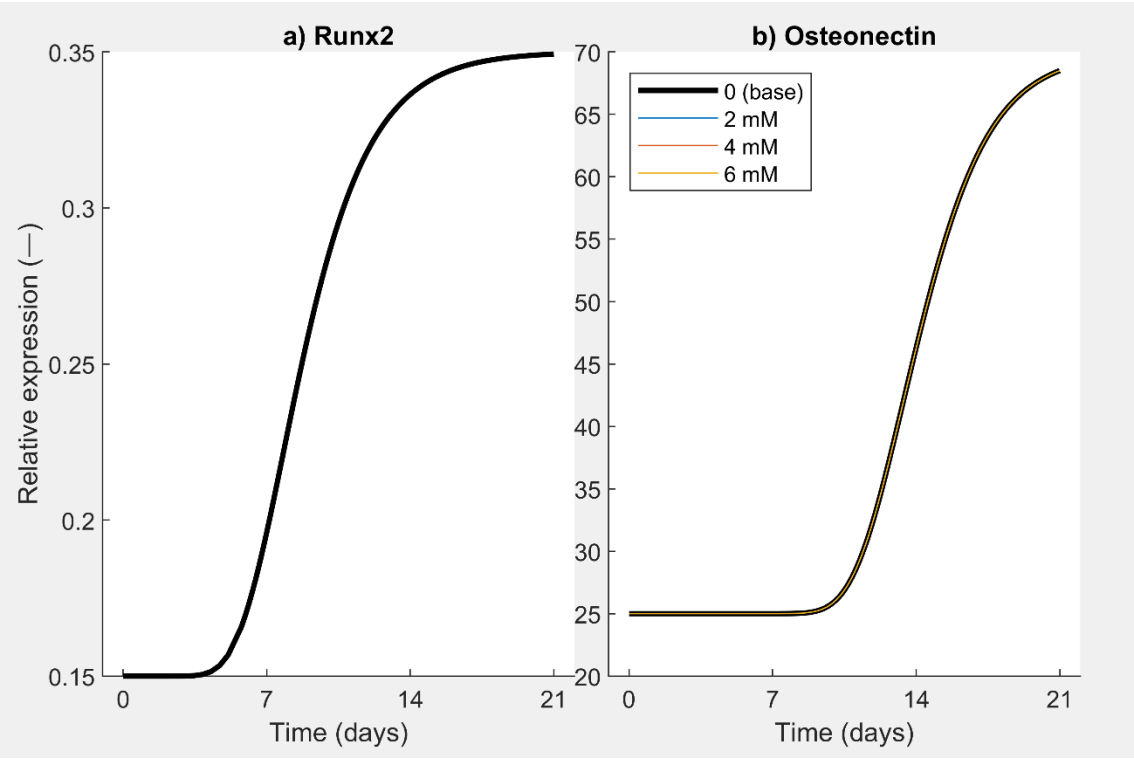

Figure 3.19. Response of relative gene expression to variations in lactate concentration in the culture medium

The total cell count is slightly reduced when using culture medium contaminated with lactate (Figure 3.20).

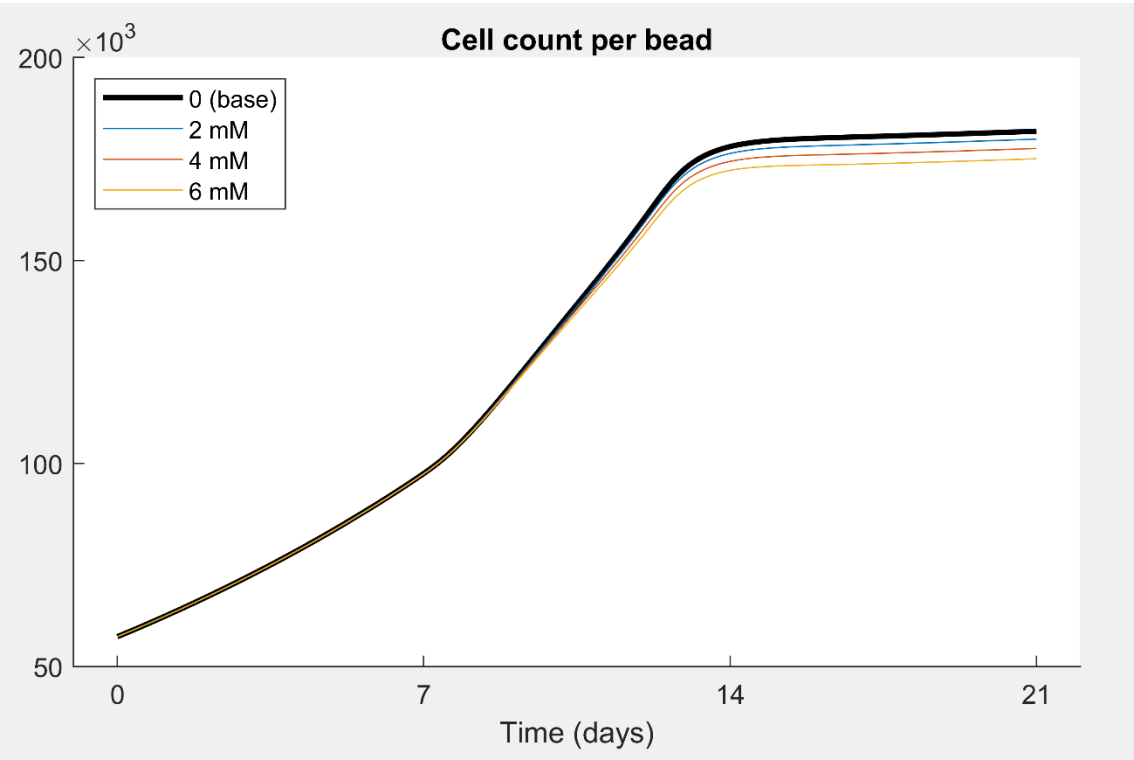

Figure 3.20. Response of total cell population per alginate-gelatin bead to variations in lactate concentration in the culture medium

The cell density in the alginate-gelatin bead is also reduced (Figure 3.21a), but the relative radial cell density profile is largely unchanged (Figure 3.21b).

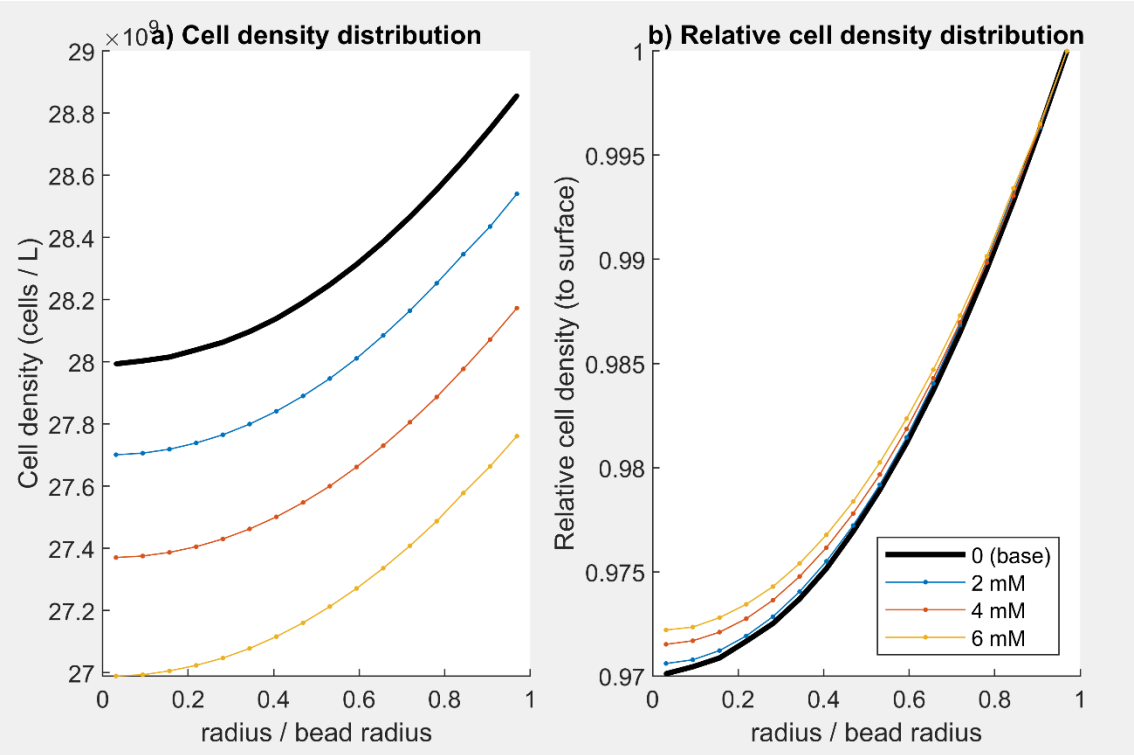

Figure 3.21. Response of the radial cell density distribution at day 21 to variations in lactate concentration in the culture medium

The analysis suggests that extracellular lactate has little effect on the outcome of the osteogenic differentiation process of mesenchymal stem cells. The validity of the result depends on the accuracy of the death-related parameters of the model. Although the parameters were estimated based on experimental data, those data do not carry enough information about cell death, given that the experimental objective was to culture — and not kill — the cells. While qualitatively correct, the prediction of the mathematical model about the impact of extracellular lactate on the outcome of the osteogenic differentiation, should seek experimental confirmation before attempting to replicate the results in clinically relevant settings.

3.4.4. Model response to dexamethasone concentration variations

Dexamethasone fulfills a key role in the osteogenic differentiation process of mesenchymal stem cells: it is the differentiation agent that triggers the chain of genetic and metabolic changes transforming MSCs into osteoblasts. Apart from the base case simulation (where the concentration of dexamethasone in the culture medium is 100 nmol/L), four additional scenarios were simulated where the concentration of dexamethasone in the culture medium inlet were 80, 90, 110, and 120 nmol/L.

Intracellular metabolism (Figure 3.22) remains at basal MSC levels when the concentration of dexamethasone is reduced to 80 nmol/L. When dexamethasone concentration is increased to 90 nmol/L, intracellular metabolism does shift towards the pre-osteoblast (PRE) phenotype, but the shift is considerably delayed and flattened over a longer period, with the peak values for each intracellular metabolite occurring about 7–10 days later than in the base case. When using higher concentrations of dexamethasone in the culture medium, the metabolic changes occur sooner and over a shorter duration, with the effect being more pronounced for the highest concentration (at 120 nmol/L).

The effect on the extracellular metabolite concentration levels (Figure 3.23) is complementary to the intracellular picture: the trends suggest the existence of a single cell type when the concentration of dexamethasone is 80 nmol/L, and shows the typical extreme (largest for lactate, and smallest for glucose and glutamine) value that corresponds to peak intracellular metabolic activity and cross-membrane transport. The profile is delayed and stretched over a longer duration when the concentration of dexamethasone is 90 nmol/L. The larger 110 and 120 nmol/L concentrations have the opposite effect: the largest changes occur sooner and over a shorter timespan than in the base case. The timepoints corresponding to the largest changes are synchronized between the intracellular (Figure 3.22) and extracellular (Figure 3.23) compartments.

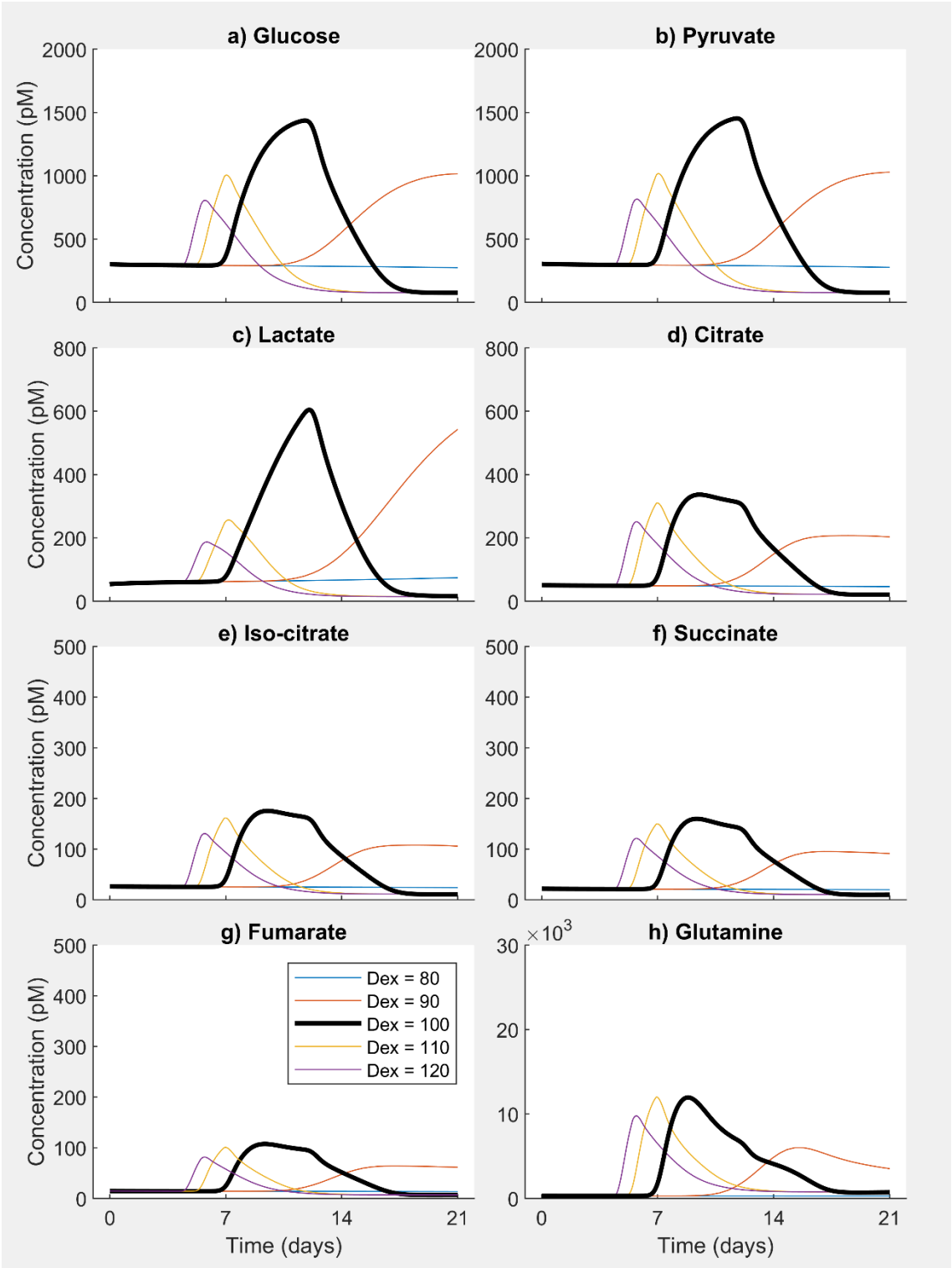

Figure 3.22. Response of intracellular metabolism to variations in dexamethasone concentration in the culture medium

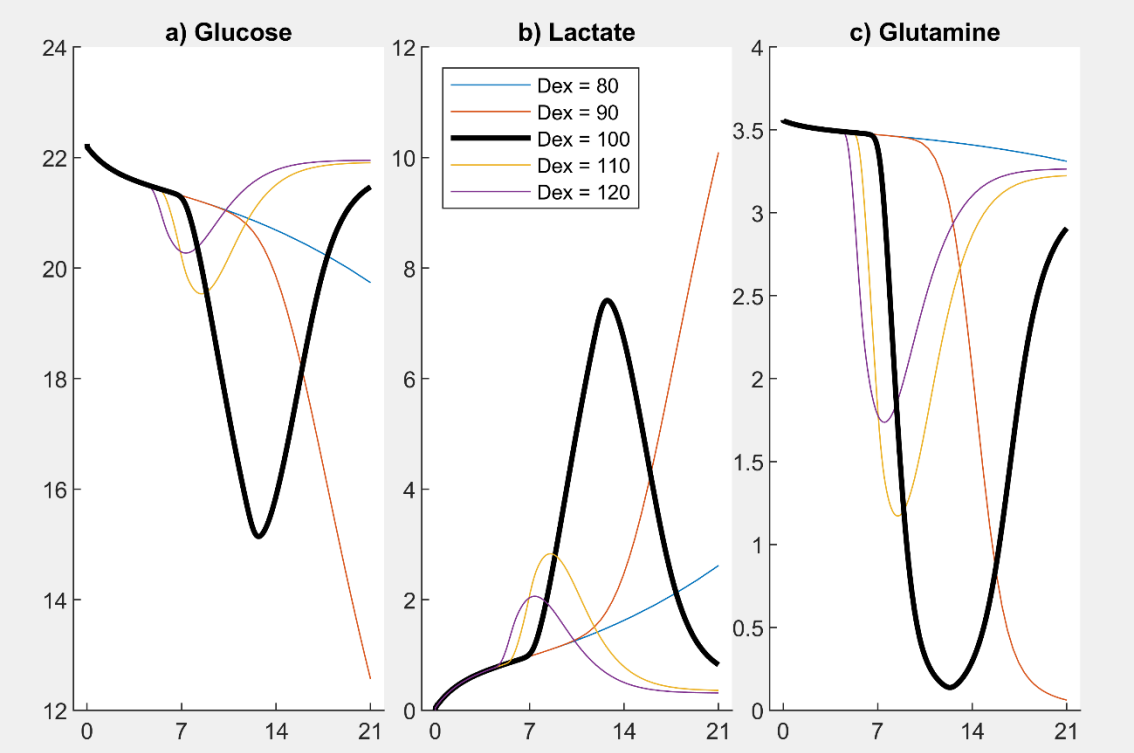

Figure 3.23. Response of extracellular (bulk liquid) metabolite levels to variations in dexamethasone concentration in the culture medium

Figure 3.24 shows the response of gene expression in these scenarios, which is drastically reduced for the dexamethasone deficient scenarios, with no significant increase in *osteonectin* expression, an important marker of osteogenesis (which is incomplete in this case). On the other hand, when using culture medium richer in dexamethasone differentiation agent, the cells overexpress (compared to the base case) the two modelled genes, whose relative expression is 5–10 times larger than in the base case scenario.

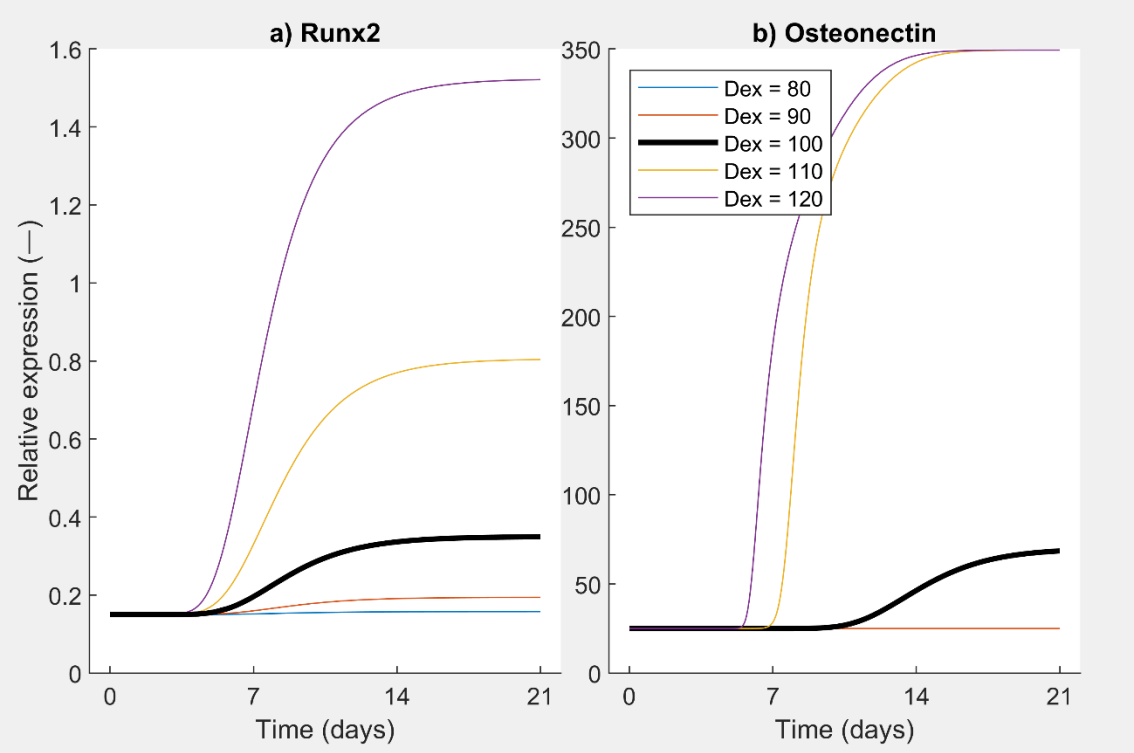

Figure 3.24. Response of relative gene expression to variations in dexamethasone concentration in the culture medium

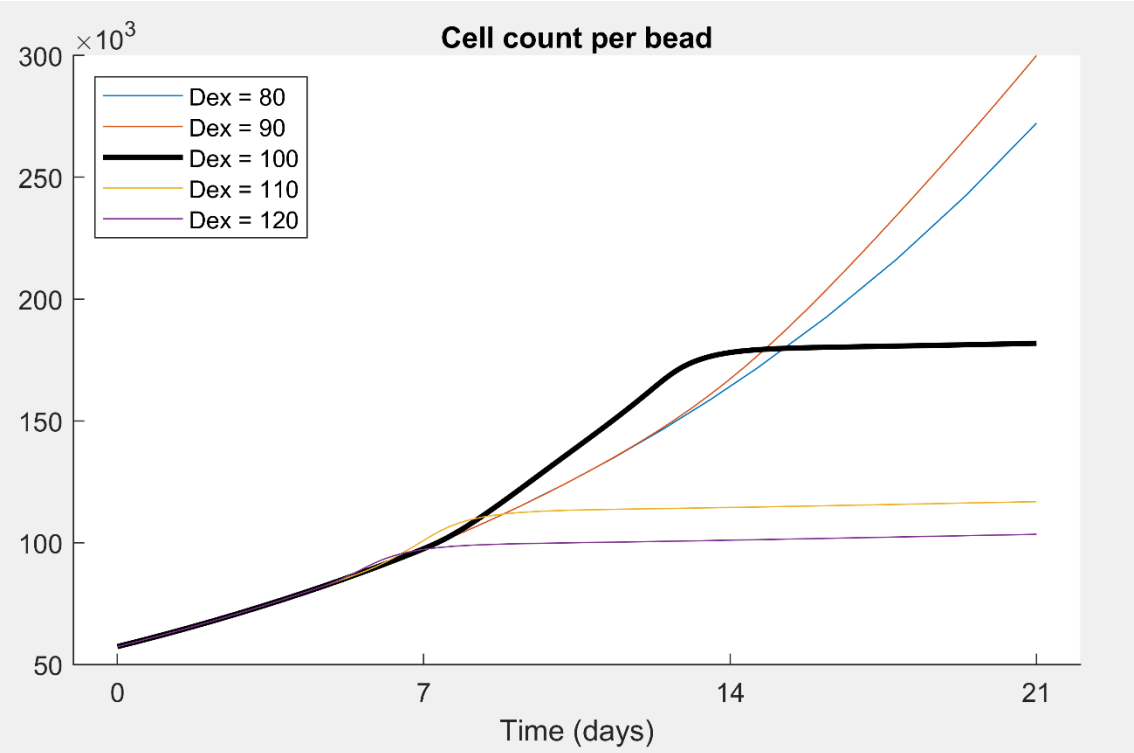

Figure 3.25. Response of total cell population per alginate-gelatin bead to variations in dexamethasone concentration in the culture medium

Cell count plots (Figure 3.25) show that in the presence of reduced dexamethasone concentration the cells continue to expand steadily. In contrast,

when using larger concentrations of dexamethasone, the cell count stagnates and settles at lower values, indicating that cells have terminally differentiated into osteoblasts (which have generally larger cell cycle duration and lower growth rate compared to mesenchymal stem cells and pre-osteoblasts).

Cell densities inside the alginate-gelatin bead at day 21 (Figure 3.26a) are correlated with the total cell count (*i.e.*, higher cell count corresponds to higher cell density). Figure 3.26b shows the relative cell density at day 21 in the alginate-gelatin bead. In the base case, cell density is lower near the center of the bead, because the cells uptake nutrients as they are transported by molecular diffusion, resulting in lower extracellular metabolite concentrations closer to the center, reduced intracellular metabolic activity and lower growth rates and cell density. This effect is qualitatively the same when the concentration of dexamethasone is 80 nmol/L but reduced in intensity since mesenchymal stem cells uptake less nutrients from their environment compared to pre-osteoblasts. The same effect (lower cell density near the center of the bead) is observed when the concentration of dexamethasone is increased to 90 nmol/L; its intensity is even higher than in the base case, because both the count and percentage of pre-osteoblasts in the bead are higher than in the base case, and pre-osteoblasts uptake more nutrients than mesenchymal stem cells. When using larger concentrations of dexamethasone than in the base case, cell density is highest in the center of the alginate-gelatin bead, because the transport of dexamethasone through the bead requires a finite amount of time and the cells closer to the center of the bead experience an environment with lower dexamethasone concentrations compared to the cells closer to the outer surface. Therefore, cells neared to the center of the bead will express genes at a slower pace and will differentiate later than those that are closer to the outer surface, spending more time as mesenchymal stem cells or pre-osteoblasts, during which they proliferate more than the cells at the surface, thus increasing their density faster, despite facing lower nutrient concentrations and higher waste (lactate) levels than cells at the outer bead surface.

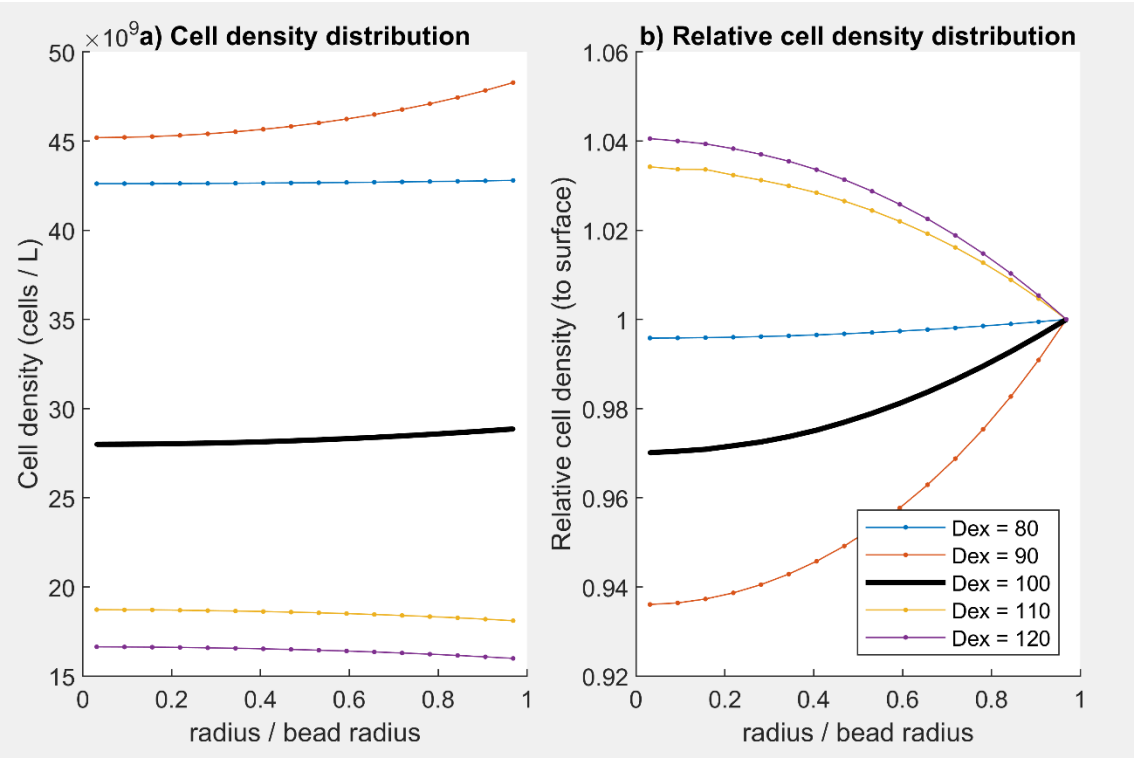

Figure 3.26. Response of the radial cell density distribution at day 21 to variations in dexamethasone concentration in the culture medium

The mathematical model correctly predicts that higher dexamethasone concentrations aid in the process of osteogenic differentiation of mesenchymal stem cells. Although qualitatively meaningful, these results may not quantitatively represent the biological outcome, as some of the parameters of the model may be inaccurate due to insufficient information in the experimental data used to estimate them. Furthermore, cells may experience gene inactivation at higher concentrations of dexamethasone, which the mathematical model does not account for in its current form.

3.4.5. Model response to alginate-gelatin bead diameter variations

The size of the alginate-gelatin bead can be controlled by changing the proportion of the ingredients or the size and shape of the nozzle that aids in the formation of the droplets (before they are immersed in solution where they become viscous gelatinous beads). This chapter presents the impact of changing the radius of the alginate-gelatin bead by 30% in both directions. The legends of the figures below show the diameter of the beads, labeled “d”.

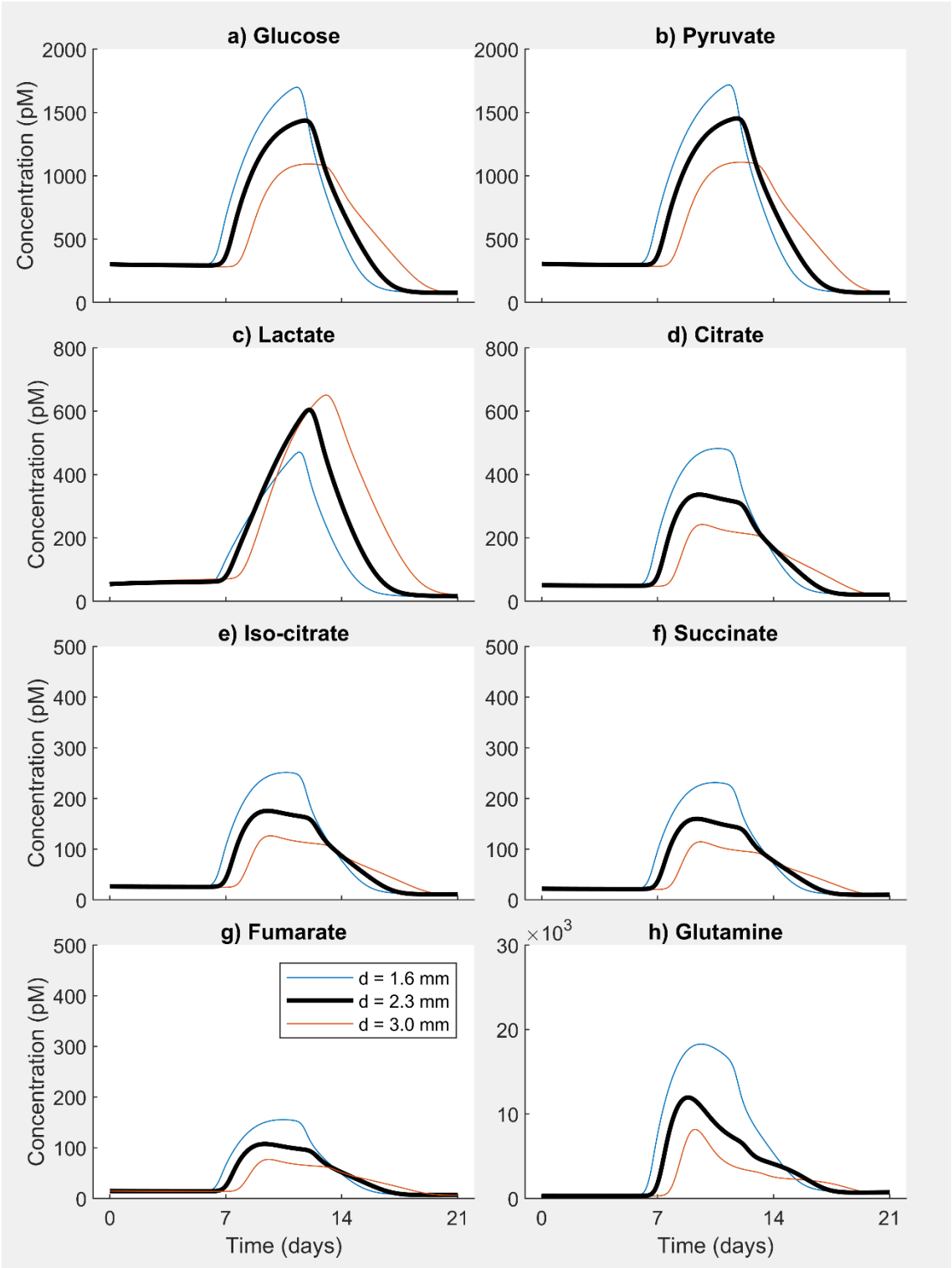

Figure 3.27. Response of intracellular metabolism to variations in alginate-gelatin bead diameter

The main disadvantage of having a larger bead is caused by mass transport limitations, which lessen the amount of nutrients that are available to cells deeper in the bead (closer to the center). The lack of nutrients then lowers

cross-membrane transport rates and intracellular metabolite concentration levels (Figure 3.27).

Furthermore, larger beads have proportionally higher cell counts (at the same cell density), making the nutrient uptake and waste generation more intense, which exacerbates the effect not only on the intracellular compartment, but on the extracellular one as well (Figure 3.28).

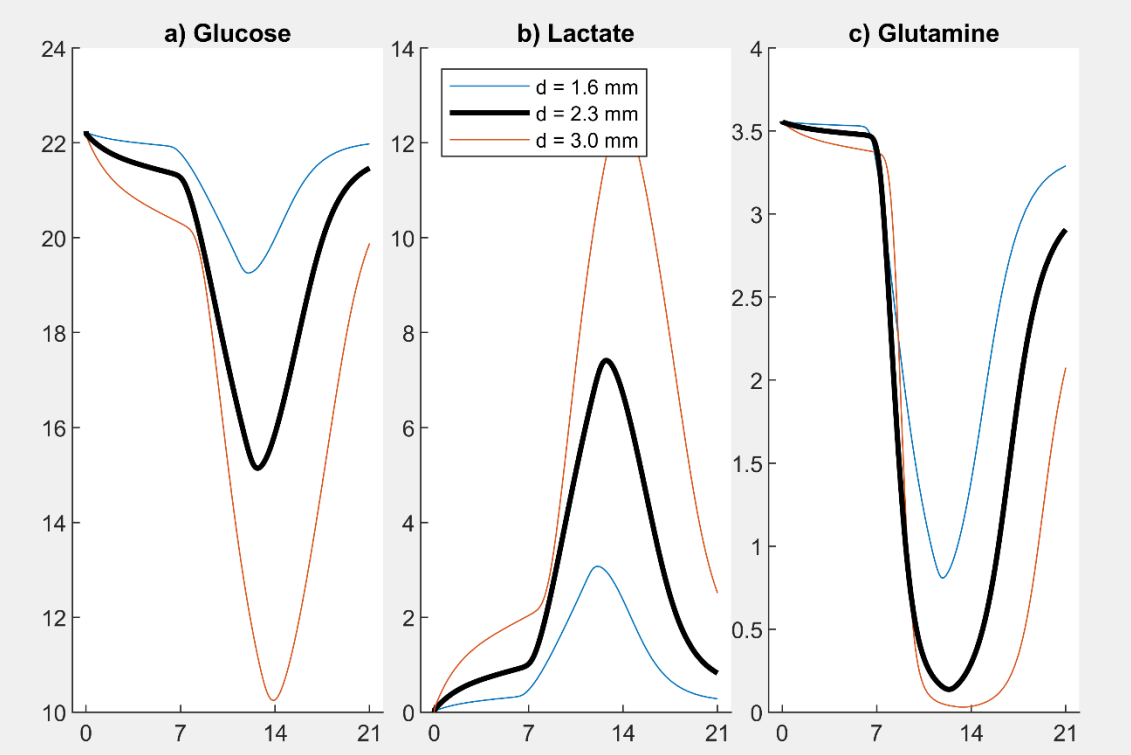

Figure 3.28. Response of extracellular (bulk liquid) metabolite levels to variations in alginate-gelatin bead diameter

Gene expression is visibly affected by the alginate-bead size (Figure 3.29): dexamethasone has easier access to the cells near the center of smaller beads and can trigger the gene switches sooner than in the base case. Larger beads impede the efficient transport of dexamethasone, whose lowered levels require longer times to activate the expression of the two osteogenic genes.

Although the initial cell density was identical in the three scenarios, larger beads have a higher cell count as they can fit more cells in their larger volume, even at the same cell density. Cell counts are, predictably, higher for larger beads (Figure 3.30).

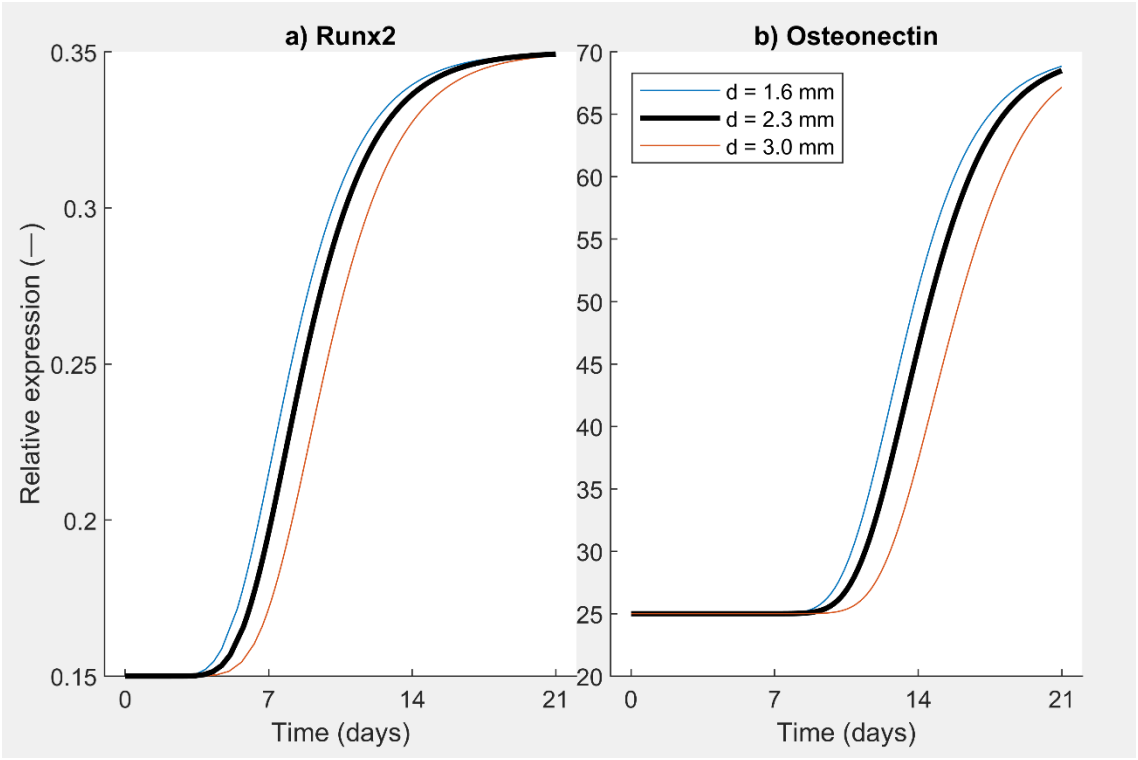

Figure 3.29. Response of relative gene expression to variations in alginate-gelatin bead diameter

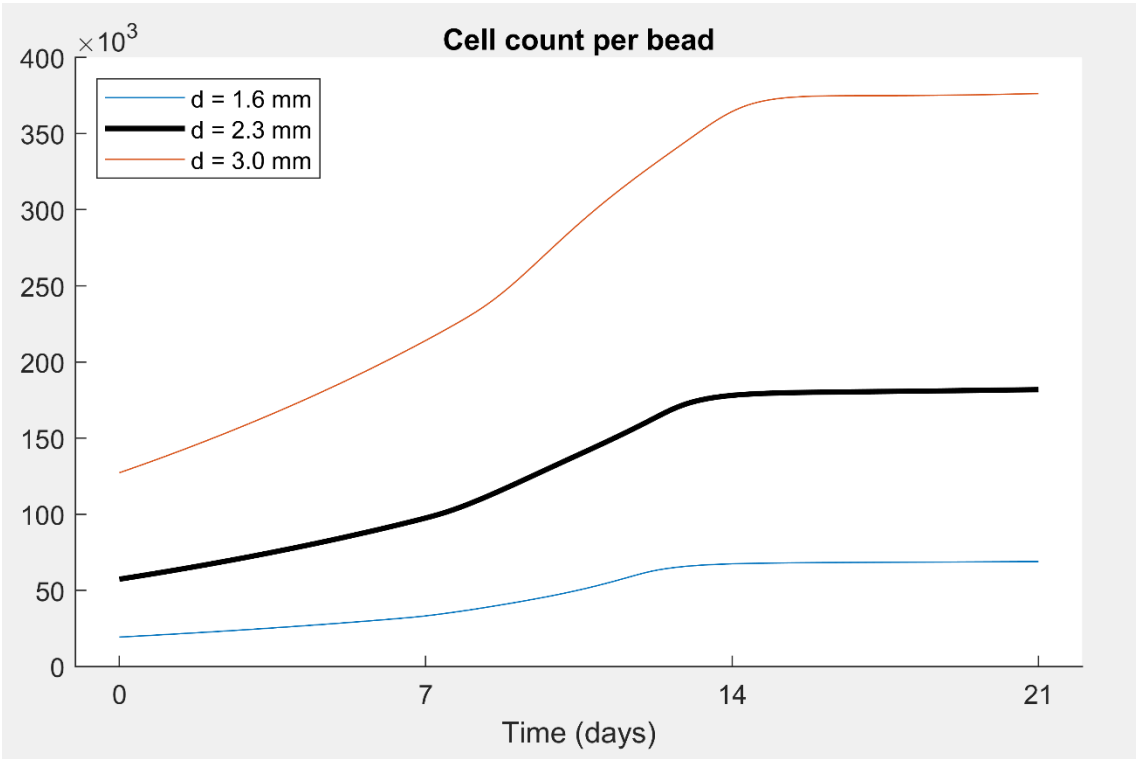

Figure 3.30. Response of total cell population per alginate-gelatin bead to variations in alginate-gelatin bead diameter

The radial cell density profiles at day 21 show higher cell densities in smaller alginate-gelatin beads (Figure 3.31a), corresponding to milder mass

transport limitations. Despite the higher cell density, the cell count per bead is still larger for bigger beads (as shown in Figure 3.30). The efficiency of the mass transport of nutrients radially through the alginate-gelatin bead is confirmed by the relative radial cell density profile (Figure 3.31b): the values of the cell density at the center of the bead and at the outer surface are closer when the beads have smaller radii.

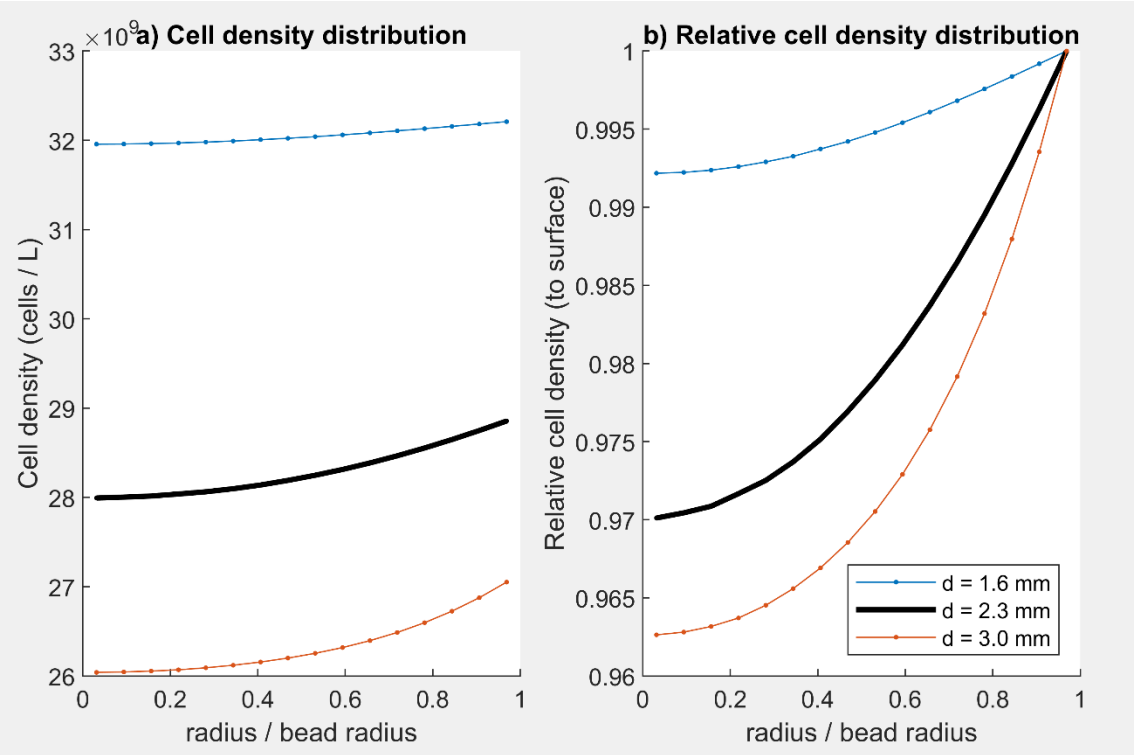

Figure 3.31. Response of the radial cell density distribution at day 21 to variations in alginate-gelatin bead diameter

The results presented in this chapter indicate that the optimal alginate-gelatin bead size is likely determined by a tradeoff between the convenience of using larger beads and the nutrient mass transport efficiency observed when using smaller beads. Alginate-gelatin beads with a radius of 1.5 mm (diameter of 3 mm) do not exhibit strong mass transport limitations.

Chapter 4. Conclusions and Directions for future work

This chapter summarizes the key points of the current thesis, emphasizes the original contributions within, and lists recommendations for future research efforts.

4.1. Conclusions

This thesis demonstrates a population balance model which describes mesenchymal stem cell (MSC) osteogenic differentiation, linking metabolism, gene expression, and cell cycle dynamics. The model introduced in Chapter 2 captures the heterogeneity of the cell cycle, and its predictions agree with experimental measurements. An analysis of the effects of altering the growth rates of mesenchymal stem cells and pre-osteoblasts reveals a potential inherent trade-off between proliferation and differentiation, even when the two behaviors are not competing for the energetic resources of the cell. Global parameter sensitivity analysis reveals that the most significant parameters are related to differentiation (controlled by gene expression) and proliferation (controlled by the duration and traversal rates of the cell cycle phases).

Chapter 3 presents a multiscale approach for the process of osteogenic differentiation of mesenchymal stem cells in a rotating wall bioreactor, built around population balance equations and includes a concise and carefully selected set of intracellular metabolites, as well as gene expression and cell cycle dynamics. The multiscale mathematical model captures cell cycle, differentiation-state and spatial heterogeneity, and interconnects processes at different biological and physical scales: (1) cell cycle phase and population level, (2) bead level, and (3) bioreactor level. The mathematical model was used to simulate the rotating wall bioreactor for 21 days of differentiation. Model predictions agreed with experimental measurements for intracellular metabolism as well as relative gene expression. Global sensitivity analysis revealed that mass transport properties of the alginate-gelatin bead are less significant for the outcome of the simulation than biological parameters of the cultured cells. Future parameter estimation efforts should focus on more accurately determining the

latter. The impact of alginate-gelatin bead size on the outcome of the simulation is negligible for beads smaller than 3–4 mm in diameter.

The mathematical models proposed in this work provide a detailed view of MSC osteogenic differentiation built on deterministic population balances that can serve as a starting point for model-based bioprocess optimization and support the development of bone grafts for medical applications. Although the formulated mathematical model and the implemented companion computational model were adapted for mesenchymal stem cells and their differentiation into the bone cell lineage, the underlying framework is more general and may be successfully applied to other research applications involving the differentiation of stem cells (*e.g.*, nerve or heart muscle cells) with minimal changes to the structure of the mathematical model.

4.2. Original contributions

The mathematical representation for the osteogenic differentiation of mesenchymal stem cells uses a refined population balance equation at the core of the model. The following improvements are original contributions of the work showcased in this thesis:

1. The continuous population balance equation for each cell cycle phase contains a duration variable that can be set to the experimentally determined value and the rest of the computation behaves accordingly.

2. Cellular differentiation has been localized precisely within the lumped Gap 0/Gap 1 cell cycle phase, instead of at the end of the cell division cycle, as done previously in the scientific literature.

3. All cell cycle phases are regarded as growth stages that are conceptually very similar, differing only in terms of their relative position within the division cycle and specific behaviors for transition or differentiation. Each phase uses an appropriate modification of the primary population balance equation to accounts for phase specific behaviors (*i.e.*, the DNA synthesis phase does not utilize a transition function, while the lumped Gap 0/Gap 1 cell cycle phase incorporates information about cellular differentiation rates in addition to transition).

4. The mathematical model includes a representative subset of intracellular metabolites that showed significant changes during the process of osteogenic differentiation of mesenchymal stem cells, selected from the glycolysis and oxidative phosphorylation metabolic pathways (which were shown to play a significant role in differentiation to the bone cell lineage)

5. Cross membrane transport of metabolites is rigorously modelled using a product-inhibited transport rate equation

6. The model improves the mathematical connection between the population-level growth rate of the cells and metabolism by connecting the growth rate to the intracellular context of the cell instead of cell culture metabolite levels (improving on the previously used method)

7. The mathematical model includes two genes that are characteristic of early and late osteogenic differentiation: the runt related transcription factor 2 (*Runx2*) and *osteonectin*.

4.3. Recommendations for future directions

While researching the subject of this thesis, several weaknesses that require further effort or inquiry have been uncovered.

Simulation speed

Although the mathematical model presented in Chapter 3 of this thesis is flexible and accurate, the current computer implementation renders the code too slow for model-based optimization, unless a powerful computational cluster is available and used for calculations.

Future efforts may improve computational efficiency by coding the mathematical model using a lower-level programming language, such as C++ or Fortran. Alternatively, a modeling language (such as gPROMS) may be used to similar effect — this approach was considered for the mathematical model in this thesis as well, but its implementation has been unsuccessful up to this point.

Another option that may be feasible under some scenarios would be to reduce the complexity of the model. Despite being a reasonable research focus,

completing this task successfully is challenging and might be impossible to achieve without reducing the model's flexibility, accuracy, or both.

Integration of computational fluid dynamics in the bioreactor model

The most complex of the mathematical models introduced in this thesis integrates the phenomena that occur at the cell, bead, and reactor scales within a biological reactor. The most comprehensive approach for reactor modeling includes computational fluid dynamics (CFD) to simulate fluid flows during dynamic bioreactor operation. Many such (CFD) modeling and simulation studies have been published in scientific literature, including for models of bioreactors. However, no studies that integrate multiple geometrical scales while using CFD seem to exist, and this is likely because of the complexity of such models and the long duration of the individual simulations. Researching the reactor scale integrated with the cellular and bead-scale phenomena is a logical continuation of the current thesis.

Investigation of other differentiation protocols and cell sources

The mathematical model presented in this thesis is accurate and offers significant flexibility and modularity. However, the set of 3 differentiation states that were included in the description of osteogenesis is based on the phenotypic changes (intracellular metabolism) observed in mesenchymal stem cells treated with dexamethasone as the osteogenic differentiation agent.

Although mesenchymal stem cells (MSCs) are a suitable and reliable starting point for osteogenic differentiation processes, multiple differentiation protocols exist, involving MSCs as well as other stem cell types (such as pluripotent stem cells). To make the model more general, other cell sources and cell types should be researched, and the modeling approach should attempt to identify patterns and common ground between the various experimental methods.

Bibliography

[1] P. v. Giannoudis, H. Dinopoulos, E. Tsiridis, Bone substitutes: An update, Injury. 36 (2005) S20–S27. https://doi.org/10.1016/j.injury.2005.07.029.

[2] V. Martin, A. Bettencourt, Bone regeneration: Biomaterials as local delivery systems with improved osteoinductive properties, Materials Science and Engineering: C. 82 (2018) 363–371. https://doi.org/10.1016/j.msec.2017.04.038.

[3] A.R. Amini, C.T. Laurencin, S.P. Nukavarapu, Bone tissue engineering: recent advances and challenges., Crit Rev Biomed Eng. 40 (2012) 363–408. https://doi.org/10.1615/critrevbiomedeng.v40.i5.10.

[4] F.R. Maia, A.R. Bastos, J.M. Oliveira, V.M. Correlo, R.L. Reis, Recent approaches towards bone tissue engineering, Bone. 154 (2022) 116256. https://doi.org/10.1016/j.bone.2021.116256.

[5] J.-Y. Hsieh, Y.-S. Fu, S.-J. Chang, Y.-H. Tsuang, H.-W. Wang, Functional Module Analysis Reveals Differential Osteogenic and Stemness Potentials in Human Mesenchymal Stem Cells from Bone Marrow and Wharton's Jelly of Umbilical Cord, Stem Cells Dev. 19 (2010) 1895–1910. https://doi.org/10.1089/scd.2009.0485.

[6] C.-C. Wei, A.B. Lin, S.-C. Hung, Mesenchymal Stem Cells in Regenerative Medicine for Musculoskeletal Diseases: Bench, Bedside, and Industry, Cell Transplant. 23 (2014) 505–512. https://doi.org/10.3727/096368914X678328.

[7] Q. Xie, Z. Wang, H. Zhou, Z. Yu, Y. Huang, H. Sun, X. Bi, Y. Wang, W. Shi, P. Gu, X. Fan, The role of miR-135-modified adipose-derived mesenchymal stem cells in bone regeneration, Biomaterials. 75 (2016) 279–294. https://doi.org/10.1016/j.biomaterials.2015.10.042.

[8] C. McLeod, R. Mauck, On the origin and impact of mesenchymal stem cell heterogeneity: new insights and emerging tools for single cell analysis, Eur Cell Mater. 34 (2017) 217–231. https://doi.org/10.22203/eCM.v034a14.

[9] T. Stiehl, A. Marciniak-Czochra, Characterization of stem cells using mathematical models of multistage cell lineages, Math Comput Model. 53 (2011) 1505–1517. https://doi.org/10.1016/j.mcm.2010.03.057.

[10] A. Jilkine, Mathematical Models of Stem Cell Differentiation and Dedifferentiation, Curr Stem Cell Rep. 5 (2019) 66–72. https://doi.org/10.1007/s40778-019-00156-z.

[11] J.E. Till, E.A. McCulloch, A direct measurement of the radiation sensitivity of normal mouse bone marrow cells., Radiat Res. 14 (1961) 213–22.

[12] A. Romito, G. Cobellis, Pluripotent Stem Cells: Current Understanding and Future Directions, Stem Cells Int. 2016 (2016) 1–20. https://doi.org/10.1155/2016/9451492.

[13] T. Graf, M. Stadtfeld, Heterogeneity of Embryonic and Adult Stem Cells, Cell Stem Cell. 3 (2008) 480–483. https://doi.org/10.1016/j.stem.2008.10.007.

[14] T. Shinohara, M.R. Avarbock, R.L. Brinster, β1- and α6-integrin are surface markers on mouse spermatogonial stem cells, Proceedings of the National Academy of Sciences. 96 (1999) 5504–5509. https://doi.org/10.1073/pnas.96.10.5504.

[15] N. Barker, J.H. van Es, J. Kuipers, P. Kujala, M. van den Born, M. Cozijnsen, A. Haegebarth, J. Korving, H. Begthel, P.J. Peters, H. Clevers, Identification of stem cells in small intestine and colon by marker gene Lgr5, Nature. 449 (2007) 1003–1007. https://doi.org/10.1038/nature06196.

[16] J.A. Thomson, J. Itskovitz-Eldor, S.S. Shapiro, M.A. Waknitz, J.J. Swiergiel, V.S. Marshall, J.M. Jones, Embryonic Stem Cell Lines Derived from Human Blastocysts, Science (1979). 282 (1998) 1145–1147. https://doi.org/10.1126/science.282.5391.1145.

[17] K. Takahashi, S. Yamanaka, Induction of Pluripotent Stem Cells from Mouse Embryonic and Adult Fibroblast Cultures by Defined Factors, Cell. 126 (2006) 663–676. https://doi.org/10.1016/j.cell.2006.07.024.

[18] K. Takahashi, K. Tanabe, M. Ohnuki, M. Narita, T. Ichisaka, K. Tomoda, S. Yamanaka, Induction of Pluripotent Stem Cells from Adult Human Fibroblasts by Defined Factors, Cell. 131 (2007) 861–872. https://doi.org/10.1016/j.cell.2007.11.019.

[19] M.J. Shamblott, B.E. Edwards, J.D. Gearhart, PLURIPOTENT STEM CELLS, in: Principles of Tissue Engineering, Elsevier, 2000: pp. 369–381. https://doi.org/10.1016/B978-012436630-5/50033-7.

[20] A.G. Smith, Embryo-Derived Stem Cells: Of Mice and Men, Annu Rev Cell Dev Biol. 17 (2001) 435–462. https://doi.org/10.1146/annurev.cellbio.17.1.435.

[21] J.R. Plews, J.C. Wu, Pluripotent Stem Cells, in: Brenner's Encyclopedia of Genetics, Elsevier, 2013: pp. 370–373. https://doi.org/10.1016/B978-0-12-374984-0.00473-3.

[22] R.G. Hawley, A. Ramezani, T.S. Hawley, Hematopoietic Stem Cells, in: 2006: pp. 149–179. https://doi.org/10.1016/S0076-6879(06)19007-2.

[23] E.A. McCulloch, J.E. Till, Perspectives on the properties of stem cells, Nat Med. 11 (2005) 1026–1028. https://doi.org/10.1038/nm1005-1026.

[24] J.Y. Lee, S.-H. Hong, Hematopoietic Stem Cells and Their Roles in Tissue Regeneration, Int J Stem Cells. 13 (2020) 1–12. https://doi.org/10.15283/ijsc19127.

[25] A.P. Ng, W.S. Alexander, Haematopoietic stem cells: past, present and future, Cell Death Discov. 3 (2017) 17002. https://doi.org/10.1038/cddiscovery.2017.2.

[26] A. Konturek-Ciesla, D. Bryder, Stem Cells, Hematopoiesis and Lineage Tracing: Transplantation-Centric Views and Beyond, Front Cell Dev Biol. 10 (2022). https://doi.org/10.3389/fcell.2022.903528.

[27] L. Walcher, A.-K. Kistenmacher, H. Suo, R. Kitte, S. Dluczek, A. Strauß, A.-R. Blaudszun, T. Yevsa, S. Fricke, U. Kossatz-Boehlert, Cancer Stem Cells—Origins and Biomarkers: Perspectives for Targeted Personalized Therapies, Front Immunol. 11 (2020). https://doi.org/10.3389/fimmu.2020.01280.

[28] S. Buczacki, Cancer Stem Cells, in: Encyclopedia of Cell Biology, Elsevier, 2016: pp. 807–812. https://doi.org/10.1016/B978-0-12-394447-4.30119-5.

[29] J.C. Chang, Cancer stem cells, Medicine. 95 (2016) S20–S25. https://doi.org/10.1097/MD.0000000000004766.

[30] Z. Yu, T.G. Pestell, M.P. Lisanti, R.G. Pestell, Cancer stem cells, Int J Biochem Cell Biol. 44 (2012) 2144–2151. https://doi.org/10.1016/j.biocel.2012.08.022.

[31] R.O. Dillman, J.A. Koziol, A mathematical model of monoclonal antibody therapy in leukemia, Mathematical Modelling. 9 (1987) 29–35. https://doi.org/10.1016/0270-0255(87)90071-6.

[32] F. Nazari, A.T. Pearson, J.E. Nör, T.L. Jackson, A mathematical model for IL-6-mediated, stem cell driven tumor growth and targeted treatment, PLoS Comput Biol. 14 (2018) e1005920. https://doi.org/10.1371/journal.pcbi.1005920.

[33] A.L. Grilo, A. Mantalaris, A Predictive Mathematical Model of Cell Cycle, Metabolism, and Apoptosis of Monoclonal Antibody-Producing GS–NS0 Cells, Biotechnol J. 14 (2019) 1800573. https://doi.org/10.1002/biot.201800573.

[34] T.J. van Steeg, K.R. Bergmann, N. Dimasi, K.F. Sachsenmeier, B. Agoram, The application of mathematical modelling to the design of bispecific monoclonal antibodies, MAbs. 8 (2016) 585–592. https://doi.org/10.1080/19420862.2016.1141160.

[35] S. Singh, N.K. Kumar, P. Dwiwedi, J. Charan, R. Kaur, P. Sidhu, V.K. Chugh, Monoclonal Antibodies: A Review, Curr Clin Pharmacol. 13 (2018) 85–99. https://doi.org/10.2174/1574884712666170809124728.

[36] B. Kelley, P. de Moor, K. Douglas, T. Renshaw, S. Traviglia, Monoclonal antibody therapies for COVID-19: lessons learned and implications for the development of future products, Curr Opin Biotechnol. 78 (2022). https://doi.org/10.1016/j.copbio.2022.102798.

[37] P.S. Grace, B.M. Gunn, L.L. Lu, Engineering the supernatural: monoclonal antibodies for challenging infectious diseases, Curr Opin Biotechnol. 78 (2022) 102818. https://doi.org/10.1016/j.copbio.2022.102818.

[38] A.J. Friedenstein, I.I. Piatetzky-Shapiro, K. v. Petrakova, Osteogenesis in transplants of bone marrow cells, Development. 16 (1966) 381–390. https://doi.org/10.1242/dev.16.3.381.

[39] F.H. Chen, L. Song, R.L. Mauck, W.-J. Li, R.S. Tuan, Mesenchymal Stem Cells, in: Principles of Tissue Engineering, Elsevier, 2007: pp. 823–843. https://doi.org/10.1016/B978-012370615-7/50059-7.

[40] D.-C. Ding, W.-C. Shyu, S.-Z. Lin, Mesenchymal Stem Cells, Cell Transplant. 20 (2011) 5–14. https://doi.org/10.3727/096368910X.

[41] M.F. Pittenger, D.E. Discher, B.M. Péault, D.G. Phinney, J.M. Hare, A.I. Caplan, Mesenchymal stem cell perspective: cell biology to clinical progress, NPJ Regen Med. 4 (2019) 22. https://doi.org/10.1038/s41536-019-0083-6.

[42] C.-T. Chen, Y.-R. v. Shih, T.K. Kuo, O.K. Lee, Y.-H. Wei, Coordinated Changes of Mitochondrial Biogenesis and Antioxidant Enzymes During Osteogenic Differentiation of Human Mesenchymal Stem Cells, Stem Cells. 26 (2008) 960–968. https://doi.org/10.1634/stemcells.2007-0509.

[43] L.C. Shum, N.S. White, B.N. Mills, K.L. de Mesy Bentley, R.A. Eliseev, Energy Metabolism in Mesenchymal Stem Cells During Osteogenic Differentiation, Stem Cells Dev. 25 (2016) 114–122. https://doi.org/10.1089/scd.2015.0193.

[44] M.E. Klontzas, S.I. Vernardis, M. Heliotis, E. Tsiridis, A. Mantalaris, Metabolomics Analysis of the Osteogenic Differentiation of Umbilical Cord Blood Mesenchymal Stem Cells Reveals Differential Sensitivity to Osteogenic Agents, Stem Cells Dev. 26 (2017) 723–733. https://doi.org/10.1089/scd.2016.0315.

[45] Q. Li, Z. Gao, Y. Chen, M.-X. Guan, The role of mitochondria in osteogenic, adipogenic and chondrogenic differentiation of mesenchymal stem cells, Protein Cell. 8 (2017) 439–445. https://doi.org/10.1007/s13238-017-0385-7.

[46] B.H. Shares, M. Busch, N. White, L. Shum, R.A. Eliseev, Active mitochondria support osteogenic differentiation by stimulating β-catenin acetylation, Journal of Biological Chemistry. 293 (2018) 16019–16027. https://doi.org/10.1074/jbc.RA118.004102.

[47] D. Granchi, G. Ochoa, E. Leonardi, V. Devescovi, S.R. Baglìo, L. Osaba, N. Baldini, G. Ciapetti, Gene Expression Patterns Related to Osteogenic Differentiation of Bone Marrow–Derived Mesenchymal Stem Cells During *Ex Vivo* Expansion, Tissue Eng Part C Methods. 16 (2010) 511–524. https://doi.org/10.1089/ten.tec.2009.0405.

[48] H. Drissi, D. Hushka, F. Aslam, Q. Nguyen, E. Buffone, A. Koff, A.J. van Wijnen, J.B. Lian, J.L. Stein, G.S. Stein, The cell cycle regulator p27(kip1) contributes to growth and differentiation of osteoblasts, Cancer Res. 59 (1999) 3705–3711.

[49] P.R. Październiorek, Mathematical Model of Stem Cell Differentiation and Tissue Regeneration with Stochastic Noise, Bull Math Biol. 76 (2014) 1642–1669. https://doi.org/10.1007/s11538-014-9971-5.

[50] G. Vozzi, G. Lucarini, M. Dicarlo, C. Andreoni, E. Salvolini, C. Ferretti, M. Mattioli-Belmonte, In vitro lifespan and senescent behaviour of human periosteal derived stem cells, Bone. 88 (2016) 1–12. https://doi.org/10.1016/j.bone.2016.04.013.

[51] M.J. Chen, J.P. Whiteley, C.P. Please, A. Schwab, F. Ehlicke, S.L. Waters, H.M. Byrne, Inducing chondrogenesis in MSC/chondrocyte co-cultures using exogenous TGF-β: a mathematical model, J Theor Biol. 439 (2018) 1–13. https://doi.org/10.1016/j.jtbi.2017.11.024.

[52] L.K. ANDERSEN, M.C. MACKEY, Resonance in Periodic Chemotherapy: A Case Study of Acute Myelogenous Leukemia, J Theor Biol. 209 (2001) 113–130. https://doi.org/10.1006/jtbi.2000.2255.

[53] A.J. Arenas, G. González-Parra, J.J. Naranjo, M. Cogollo, N. de La Espriella, Mathematical Analysis and Numerical Solution of a Model of HIV with a Discrete Time Delay, Mathematics. 9 (2021) 257. https://doi.org/10.3390/math9030257.

[54] M. Fuentes-Garí, R. Misener, D. García-Munzer, E. Velliou, M.C. Georgiadis, M. Kostoglou, E.N. Pistikopoulos, N. Panoskaltsis, A. Mantalaris, A mathematical model of subpopulation kinetics for the deconvolution of leukaemia heterogeneity, J R Soc Interface. 12 (2015). https://doi.org/10.1098/rsif.2015.0276.

[55] J. Wu, M.R. Rostami, D.P. Cadavid Olaya, E.S. Tzanakakis, Oxygen Transport and Stem Cell Aggregation in Stirred-Suspension Bioreactor Cultures, PLoS One. 9 (2014) e102486. https://doi.org/10.1371/journal.pone.0102486.

[56] E. Bartolini, H. Manoli, E. Costamagna, H.A. Jeyaseelan, M. Hamad, M.R. Irhimeh, A. Khademhosseini, A. Abbas, Population balance modelling of stem cell culture in 3D suspension bioreactors, Chemical Engineering Research and Design. 101 (2015) 125–134. https://doi.org/10.1016/j.cherd.2015.07.014.

[57] S. Banerjee, M.A. Afzal, P. Chokshi, A.S. Rathore, Mechanistic modelling of Chinese hamster ovary cell clarification using acoustic wave separator, Chem Eng Sci. 246 (2021) 116894. https://doi.org/10.1016/j.ces.2021.116894.

[58] S. Seidel, D. Eibl, Influence of Interfacial Force Models and Population Balance Models on the kLa Value in Stirred Bioreactors, Processes. 9 (2021) 1185. https://doi.org/10.3390/pr9071185.

[59] M. Loeffler, H.E. Wichmann, A comprehensive mathematical model of stem cell proliferation which reproduces most of the published experimental results, Cell Prolif. 13 (1980) 543–561. https://doi.org/10.1111/j.1365-2184.1980.tb00494.x.

[60] S.J. Morrison, J. Kimble, Asymmetric and symmetric stem-cell divisions in development and cancer, Nature. 441 (2006) 1068–1074. https://doi.org/10.1038/nature04956.

[61] A.M. Klein, B.D. Simons, Universal patterns of stem cell fate in cycling adult tissues, Development. 138 (2011) 3103–3111. https://doi.org/10.1242/dev.060103.

[62] C. Grün, B. Altmann, E. Gottwald, Advanced 3d cell culture techniques in micro-bioreactors, Part I: A systematic analysis of the literature published between 2000 and 2020, Processes. 8 (2020) 1–24. https://doi.org/10.3390/pr8121656.

[63] J. Zvicer, B. Obradovic, Bioreactors with hydrostatic pressures imitating physiological environments in intervertebral discs, J Tissue Eng Regen Med. 12 (2018) 529–545. https://doi.org/10.1002/term.2533.

[64] Á. Paim, I.C. Tessaro, N.S.M. Cardozo, P. Pranke, Mesenchymal stem cell cultivation in electrospun scaffolds: mechanistic modeling for tissue engineering, J Biol Phys. 44 (2018) 245–271. https://doi.org/10.1007/s10867-018-9482-y.

[65] D. Pearce, S. Fischer, F. Huda, A. Vahdati, Applications of Computer Modeling and Simulation in Cartilage Tissue Engineering, Tissue Eng Regen Med. 17 (2020). https://doi.org/10.1007/s13770-019-00216-9.

[66] S. Seidel, R.W. Maschke, S. Werner, V. Jossen, D. Eibl, Oxygen Mass Transfer in Biopharmaceutical Processes: Numerical and Experimental Approaches, Chem Ing Tech. 93 (2021) 42–61. https://doi.org/10.1002/cite.202000179.

[67] S.-Y. Park, C.-H. Park, D.-H. Choi, J.K. Hong, D.-Y. Lee, Bioprocess digital twins of mammalian cell culture for advanced biomanufacturing, Curr Opin Chem Eng. 33 (2021). https://doi.org/10.1016/j.coche.2021.100702.

[68] V. Jossen, D. Eibl, R. Eibl, Numerical Methods for the Design and Description of In Vitro Expansion Processes of Human Mesenchymal Stem Cells, in: 2020: pp. 185–228. https://doi.org/10.1007/10_2020_147.

[69] S.I. Ngo, Y.-I. Lim, Multiscale eulerian CFD of chemical processes: A review, ChemEngineering. 4 (2020) 1–27. https://doi.org/10.3390/chemengineering4020023.

[70] G. Wang, C. Haringa, H. Noorman, J. Chu, Y. Zhuang, Developing a Computational Framework To Advance Bioprocess Scale-Up, Trends Biotechnol. 38 (2020) 846–856. https://doi.org/10.1016/j.tibtech.2020.01.009.

[71] Y.-H. Du, M.-Y. Wang, L.-H. Yang, L.-L. Tong, D.-S. Guo, X.-J. Ji, Optimization and Scale-Up of Fermentation Processes Driven by Models, Bioengineering. 9 (2022). https://doi.org/10.3390/bioengineering9090473.

[72] A. Drochon, R. Lesieur, M. Durand, Fluid dynamics characterisation of a rotating bioreactor for tissue engineering, Med Eng Phys. 105 (2022) 103831. https://doi.org/10.1016/j.medengphy.2022.103831.

[73] M. Ye, M.C. Hill, Global Sensitivity Analysis for Uncertain Parameters, Models, and Scenarios, in: Sensitivity Analysis in Earth Observation Modelling, Elsevier, 2017: pp. 177–210. https://doi.org/10.1016/B978-0-12-803011-0.00010-0.

[74] F. Campolongo, A. Saltelli, S. Tarantola, Sensitivity Anaysis as an Ingredient of Modeling, Statistical Science. 15 (2000). https://doi.org/10.1214/ss/1009213004.

[75] A. Saltelli, I.M. Sobol', About the use of rank transformation in sensitivity analysis of model output, Reliab Eng Syst Saf. 50 (1995) 225–239. https://doi.org/10.1016/0951-8320(95)00099-2.

[76] T. Homma, A. Saltelli, Importance measures in global sensitivity analysis of nonlinear models, Reliab Eng Syst Saf. 52 (1996) 1–17. https://doi.org/10.1016/0951-8320(96)00002-6.

[77] A. Saltelli, M. Ratto, S. Tarantola, F. Campolongo, Sensitivity analysis practices: Strategies for model-based inference, Reliab Eng Syst Saf. 91 (2006) 1109–1125. https://doi.org/10.1016/j.ress.2005.11.014.

[78] W. Becker, P. Paruolo, A. Saltelli, Variable Selection in Regression Models Using Global Sensitivity Analysis, Journal of Time Series Econometrics. 13 (2021) 187–233. https://doi.org/10.1515/jtse-2018-0025.

[79] T. Ziehn, A.S. Tomlin, GUI–HDMR – A software tool for global sensitivity analysis of complex models, Environmental Modelling & Software. 24 (2009) 775–785. https://doi.org/10.1016/j.envsoft.2008.12.002.

[80] Imperial College, Biological Systems Engineering Laboratory, London, UK. (n.d.). https://www.imperial.ac.uk/bsel/.

[81] I.M. Sobol', On the distribution of points in a cube and the approximate evaluation of integrals, USSR Computational Mathematics and Mathematical Physics. 7 (1967) 86–112. https://doi.org/10.1016/0041-5553(67)90144-9.

[82] Sobol quasirandom point set, The MathWorks, Inc. (2021). https://www.mathworks.com/help/stats/sobolset.html (accessed July 21, 2021).

[83] C. Kontoravdi, S.P. Asprey, E.N. Pistikopoulos, A. Mantalaris, Application of Global Sensitivity Analysis to Determine Goals for Design of Experiments: An Example Study on Antibody-Producing Cell Cultures, Biotechnol Prog. 21 (2008) 1128–1135. https://doi.org/10.1021/bp050028k.

[84] GlutaMAX MEM alpha culture medium, ThermoFisher Scientific. (n.d.). https://www.thermofisher.com/ro/en/home/technical-resources/media-formulation.109.html (accessed September 3, 2018).

[85] R. Győrgy, M.E. Klontzas, M. Kostoglou, N. Panoskaltsis, A. Mantalaris, M.C. Georgiadis, Capturing Mesenchymal Stem Cell Heterogeneity during Osteogenic Differentiation: An Experimental–Modeling Approach, Ind Eng Chem Res. 58 (2019) 13900–13909. https://doi.org/10.1021/acs.iecr.9b01988.

[86] Kanehisa Laboratories, Glycolysis / Gluconeogenesis, Kyoto Encyclopedia of Genes and Genomes. (2017). https://www.genome.jp/kegg-bin/show_pathway?map00010 (accessed January 10, 2017).

[87] Kanehisa Laboratories, Citrate cycle (TCA cycle), Kyoto Encyclopedia of Genes and Genomes. (2017). https://www.genome.jp/kegg-bin/show_pathway?map00020 (accessed January 10, 2017).

[88] F. Langenbach, J. Handschel, Effects of dexamethasone, ascorbic acid and β-glycerophosphate on the osteogenic differentiation of stem cells in vitro, Stem Cell Res Ther. 4 (2013) 117. https://doi.org/10.1186/scrt328.

[89] R. Győrgy, M. Kostoglou, A. Mantalaris, M.C. Georgiadis, Development of a multi-scale model to simulate mesenchymal stem cell osteogenic differentiation within hydrogels in a rotating wall bioreactor, Biochem Eng J. 186 (2022) 108566. https://doi.org/10.1016/j.bej.2022.108566.

[90] J.L. Hargrove, M.G. Hulsey, E.G. Beale, The kinetics of mammalian gene expression, BioEssays. 13 (1991) 667–674. https://doi.org/10.1002/bies.950131209.

[91] RUNX family transcription factor 2, National Library of Medicine – National Center for Biology Information. (2022). https://www.ncbi.nlm.nih.gov/gene/860 (accessed September 13, 2022).

[92] SPARC (osteonectin), National Library of Medicine – National Center for Biology Information. (2022). https://www.ncbi.nlm.nih.gov/gene/6695 (accessed September 13, 2022).

[93] B. Schwanhäusser, D. Busse, N. Li, G. Dittmar, J. Schuchhardt, J. Wolf, W. Chen, M. Selbach, Global quantification of mammalian gene expression control, Nature. 473 (2011) 337–342. https://doi.org/10.1038/nature10098.

[94] G.M. Cooper, R.E. Hausman, The Cell: A Molecular Approach, 4th ed., Sinauer Associates, Inc., Sunderland, MA, 2017.

[95] P.C. Hinkle, P/O ratios of mitochondrial oxidative phosphorylation, Biochimica et Biophysica Acta (BBA) - Bioenergetics. 1706 (2005) 1–11. https://doi.org/10.1016/j.bbabio.2004.09.004.

[96] Process Systems Enterprise, gPROMS, (2020). www.psenterprise.com/products/gproms.

[97] B.M. Deasy, R.J. Jankowski, T.R. Payne, B. Cao, J.P. Goff, J.S. Greenberger, J. Huard, Modeling stem cell population Growth: Incorporating terms for proliferative heterogeneity, Stem Cells. 21 (2003) 536–545. https://doi.org/10.1634/stemcells.21-5-536.

[98] M.E. Klontzas, S.I. Vernardis, M. Heliotis, E. Tsiridis, A. Mantalaris, Metabolomics analysis of the osteogenic differentiation of umbilical cord blood mesenchymal stem cells reveals differential sensitivity to osteogenic agents, Stem Cells Dev. 26 (2017) 723–733.

[99] M.E. Klontzas, S. Reakasame, R. Silva, J.C.F. Morais, S. Vernardis, R.J. MacFarlane, M. Heliotis, E. Tsiridis, N. Panoskaltsis, A.R. Boccaccini, A. Mantalaris, Oxidized alginate hydrogels with the GHK peptide enhance cord blood mesenchymal stem cell osteogenesis: A paradigm for metabolomics-based evaluation of biomaterial design, Acta Biomater. (2019).

[100] C.-T. Chen, Y.-R. V Shih, T.K. Kuo, O.K. Lee, Y.-H. Wei, Coordinated changes of mitochondrial biogenesis and antioxidant enzymes during osteogenic differentiation of human mesenchymal stem cells, Stem Cells. 26 (2008) 960–968. https://doi.org/10.1634/stemcells.2007-0509.

[101] G. Pattappa, H.K. Heywood, J.D. de Bruijn, D.A. Lee, The metabolism of human mesenchymal stem cells during proliferation and differentiation, J Cell Physiol. 226 (2011) 2562–2570. https://doi.org/10.1002/jcp.22605.

[102] J. Wu, M.R. Rostami, D.P. Cadavid Olaya, E.S. Tzanakakis, Oxygen transport and stem cell aggregation in stirred-suspension bioreactor cultures, PLoS One. 9 (2014) 1–12. https://doi.org/10.1371/journal.pone.0102486.

[103] E. Bartolini, H. Manoli, E. Costamagna, H.A. Jeyaseelan, M. Hamad, M.R. Irhimeh, A. Khademhosseini, A. Abbas, Population balance modelling of stem cell culture in 3D suspension bioreactors, Chem Eng Res Des. 101 (2016) 125–134.

[104] M. Fuentes-Garí, R. Misener, D. García-Münzer, E. Velliou, M.C. Georgiadis, M. Kostoglou, E.N. Pistikopoulos, N. Panoskaltsis, A. Mantalaris, A mathematical model of subpopulation kinetics for the deconvolution of leukaemia heterogeneity, J R Soc Interface. 12 (2015) 20150276. https://doi.org/10.1098/rsif.2015.0276.

[105] D.G. García Münzer, M. Kostoglou, M.C. Georgiadis, E.N. Pistikopoulos, A. Mantalaris, Cyclin and DNA distributed cell cycle model for GS-NS0 cells, PLoS Comput Biol. 11 (2015) 1–28. https://doi.org/10.1371/journal.pcbi.1004062.

[106] C.T. Goudar, R. Biener, K.B. Konstantinov, J.M. Piret, Error propagation from prime variables into specific rates and metabolic fluxes for mammalian cells in perfusion culture, Biotechnol Prog. 25 (2009) 986–998. https://doi.org/10.1002/btpr.155.

[107] S.G. Villas-Bôas, J.F. Moxley, M. Akesson, G. Stephanopoulos, J. Nielsen, High-throughput metabolic state analysis: the missing link in integrated functional genomics of yeasts, Biochem J. 388 (2005) 669–677. https://doi.org/10.1042/BJ20041162.

[108] S. Ruijtenberg, S. van den Heuvel, Coordinating cell proliferation and differentiation: Antagonism between cell cycle regulators and cell type-specific gene expression, Cell Cycle. 15 (2016) 196–212. https://doi.org/10.1080/15384101.2015.1120925.

[109] I. Kalajzic, A. Staal, W.P. Yang, Y. Wu, S.E. Johnson, J.H.M. Feyen, W. Krueger, P. Maye, F. Yu, Y. Zhao, L. Kuo, R.R. Gupta, L.E.K. Achenie, H.W. Wang, D.G. Shin, D.W. Rowe, Expression profile of osteoblast lineage at defined stages of differentiation, J Biol Chem. 280 (2005) 24618–24626. https://doi.org/10.1074/jbc.M413834200.

[110] G. Vozzi, G. Lucarini, M. Dicarlo, C. Andreoni, E. Salvolini, C. Ferretti, M. Mattioli-Belmonte, In vitro lifespan and senescent behaviour of human periosteal derived stem cells, Bone. 88 (2016) 1–12. https://doi.org/10.1016/j.bone.2016.04.013.

[111] T. Thalheim, P. Buske, J. Przybilla, K. Rother, M. Loeffler, J. Galle, Stem cell competition in the gut: insights from multi-scale computational modelling, J R Soc Interface. 13 (2016) 20160218. https://doi.org/10.1098/rsif.2016.0218.

[112] M.J. Chen, J.P. Whiteley, C.P. Please, A. Schwab, F. Ehlicke, S.L. Waters, H.M. Byrne, Inducing chondrogenesis in MSC/chondrocyte co-cultures using exogenous TGF-β: a mathematical model, J Theor Biol. 439 (2018) 1–13. https://doi.org/10.1016/j.jtbi.2017.11.024.

[113] M. Renardy, A. Jilkine, L. Shahriyari, C.S. Chou, Control of cell fraction and population recovery during tissue regeneration in stem cell lineages, J Theor Biol. 445 (2018) 33–50. https://doi.org/10.1016/j.jtbi.2018.02.017.

[114] J.M. Cha, A Novel Design of 3D-Bioprocess for Embryonic Stem Cell Expansion and Differentiation, Imperial College London, 2010.

[115] A. Kumar, Development of a three-dimensional bioprocess for bone tissue engineering using a novel bioreactor, Imperial College London, 2018.

[116] M.E. Klontzas, S. Reakasame, R. Silva, J.C.F. Morais, S. Vernardis, R.J. MacFarlane, M. Heliotis, E. Tsiridis, N. Panoskaltsis, A.R. Boccaccini, A. Mantalaris, Oxidized alginate hydrogels with the GHK peptide enhance cord blood mesenchymal stem cell osteogenesis: A paradigm for metabolomics-based evaluation of biomaterial design, Acta Biomater. 88 (2019) 224–240. https://doi.org/10.1016/j.actbio.2019.02.017.

[117] A. Tahlawi, M.E. Klontzas, M.C. Allenby, J.C.F. Morais, N. Panoskaltsis, A. Mantalaris, RGD-functionalized polyurethane scaffolds promote umbilical cord blood mesenchymal stem cell expansion and osteogenic differentiation, J Tissue Eng Regen Med. (2018) term.2784. https://doi.org/10.1002/term.2784.

[118] K.Y. Lee, D.J. Mooney, Alginate: Properties and biomedical applications, Prog Polym Sci. 37 (2012) 106–126. https://doi.org/10.1016/j.progpolymsci.2011.06.003.

[119] W.E. Ranz, W.R. Marshall Jr., Evaporation from drops. Parts I and II, Chem Eng Prog. 48 (1952) 141-146 173-180.

[120] R.B. Bird, W.E. Stewart, E.N. Lightfoot, Transport Phenomena, 2nd ed., John Wiley & Sons, Inc., New York, 2002.

[121] Solve stiff differential equations and DAEs — variable order method, The MathWorks, Inc. (2021). https://www.mathworks.com/help/matlab/ref/ode15s.html (accessed May 13, 2021).

[122] P.S. Stewart, Diffusion in Biofilms, J Bacteriol. 185 (2003) 1485–1491. https://doi.org/10.1128/JB.185.5.1485-1491.2003.

[123] C.R. Wilke, P. Chang, Correlation of diffusion coefficients in dilute solutions, AIChE Journal. 1 (1955) 264–270. https://doi.org/10.1002/aic.690010222.

[124] D.G. García Münzer, M. Kostoglou, M.C. Georgiadis, E.N. Pistikopoulos, A. Mantalaris, Cyclin and DNA Distributed Cell Cycle Model for GS-NS0 Cells, PLoS Comput Biol. 11 (2015) e1004062. https://doi.org/10.1371/journal.pcbi.1004062.

Research output

A summary of the research output pertaining to this dissertation is provided below.

ISI journal publications

1. R. Győrgy, M.E. Klontzas, M. Kostoglou, N. Panoskaltsis, A. Mantalaris, M.C. Georgiadis, Capturing Mesenchymal Stem Cell Heterogeneity during Osteogenic Differentiation: An Experimental–Modeling Approach, Ind Eng Chem Res. 58 (2019) 13900–13909. https://doi.org/10.1021/acs.iecr.9b01988.

2. R. Győrgy, M. Kostoglou, A. Mantalaris, M.C. Georgiadis, Development of a multi-scale model to simulate mesenchymal stem cell osteogenic differentiation within hydrogels in a rotating wall bioreactor, Biochem Eng J. 186 (2022). https://doi.org/10.1016/j.bej.2022.108566.

ISI conference proceedings

3. R. Győrgy, M.E. Klontzas, M. Kostoglou, N. Panoskaltsis, M.C. Georgiadis, A. Mantalaris, oral presentation titled “An integrated experimental modelling approach of mesenchymal stem cell bioprocess towards osteogenic differentiation”, 20th World Congress of the International Federation of Automatic Control (IFAC WC), Toulouse, France, 9–14 July 2017.

   IFAC-PapersOnLine, 2017, https://doi.org/10.1016/j.ifacol.2017.08.1603

4. R. Győrgy, M.E. Klontzas, M. Kostoglou, N. Panoskaltsis, A. Mantalaris, M.C. Georgiadis, oral presentation titled “A population balance model for stem cell differentiation processes”, 27th European Symposium on Computer Aided Process Engineering (ESCAPE), Barcelona, Spain, 1–5 October 2017.

   Computer Aided Chemical Engineering, 2017: pp. 2761–2766. https://doi.org/10.1016/B978-0-444-63965-3.50462-1.

International conference presentations

5. R. Győrgy, M.C. Georgiadis, M. Kostoglou, A. Mantalaris, oral presentation titled “Modelling heterogeneity in stem cell cultures”, 22nd Panhellenic Chemistry Conference (Πανελλήνιο Συνέδριο Χημείας, ΠΣΧ), Thessaloniki, Greece, 2–4 December 2016.

6. R. Győrgy, M.C. Georgiadis, M. Kostoglou, A. Mantalaris, oral presentation titled “A population balance model for embryonic stem cell differentiation”, 11th Panhellenic Scientific Conference on Chemical Engineering (Πανελλήνιο Επιστημονικό Συνέδριο Χημικής Μηχανικής, ΠΕΣΧΜ), Thessaloniki, Greece, 25–27 May 2017

7. M.E. Klontzas, R. Győrgy, M. Kostoglou, N. Panoskaltsis, M.C. Georgiadis, A. Mantalaris, poster presentation titled “Integrated experimental modelling approach for the osteogenic differentiation of umbilical cord blood mesenchymal stem cells for bone tissue engineering applications”, European Chapter Meeting of the Tissue Engineering and Regenerative Medicine International Society (TERMIS EU), Davos, Switzerland, 26–30 June 2017.

Appendix A. Estimation results for the important parameters of the well plate model and their confidence intervals

Table A.1. Estimated values of the important parameters that were identified using global sensitivity analysis and their confidence intervals

Parameter name	Nominal value	Confidence intervals		
		90%	95%	99%
k_{decay}	1.85	0.827394	0.994523	1.33507
$k_{DNA,Runx2}$	117.0355	8.39000	10.0847	13.5380
$k_{DNA,osteonectin}$	0.3953	0.0694921	0.0835291	0.112132
ω_{Runx2}	0.2775	0.173551	0.208608	0.280041
$k_{diff}^{(MSC)}$	0.19	0.0427088	0.0513357	0.0689145
$k_{diff}^{(PRE)}$	35	4.50081	5.40996	7.26248
$k_{E,1}^{(MSC)}$	$5.25 \cdot 10^{-18}$	$4.1682 \cdot 10^{-19}$	$5.0101 \cdot 10^{-19}$	$6.7257 \cdot 10^{-19}$
$E_{ATP}^{(MSC)}$	400	65.1075	78.2588	105.057
$E_{ATP}^{(PRE)}$	80	19.7698	23.7633	31.9004
$k_{cat,2}$	22.66	2.71351	3.26163	4.37850

Appendix B. Convergence of sensitivity analysis for well-plate parameters

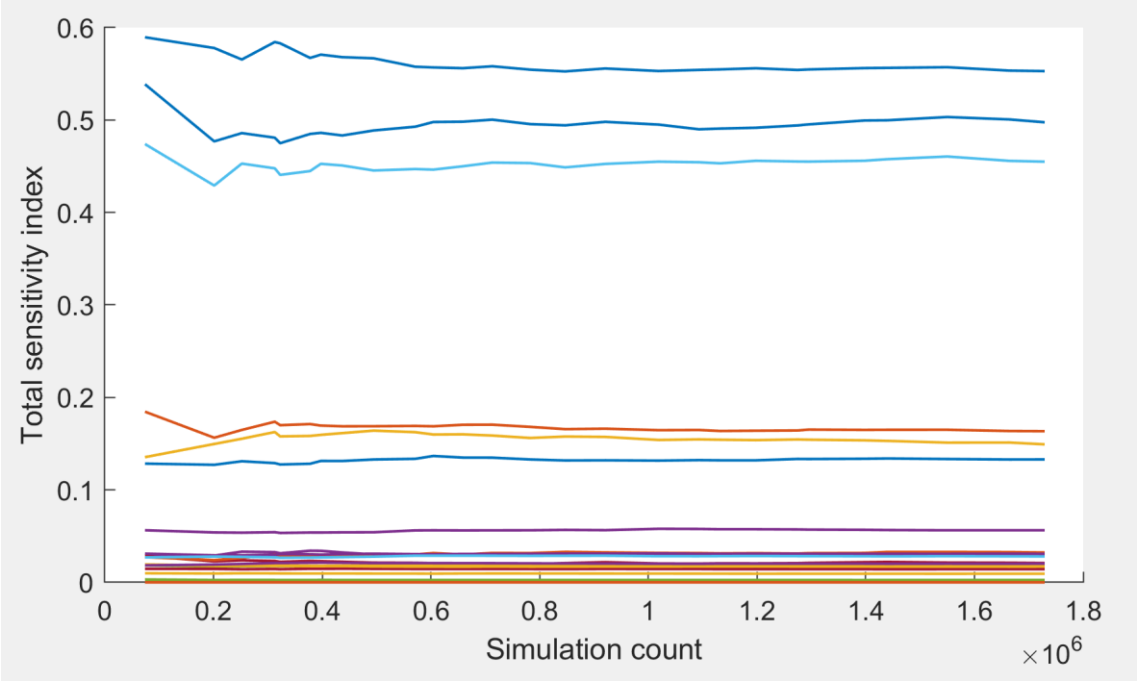

Figure B.1. Convergence plot of global sensitivity analysis for well-plate parameters, when the analyzed response is the total cell count

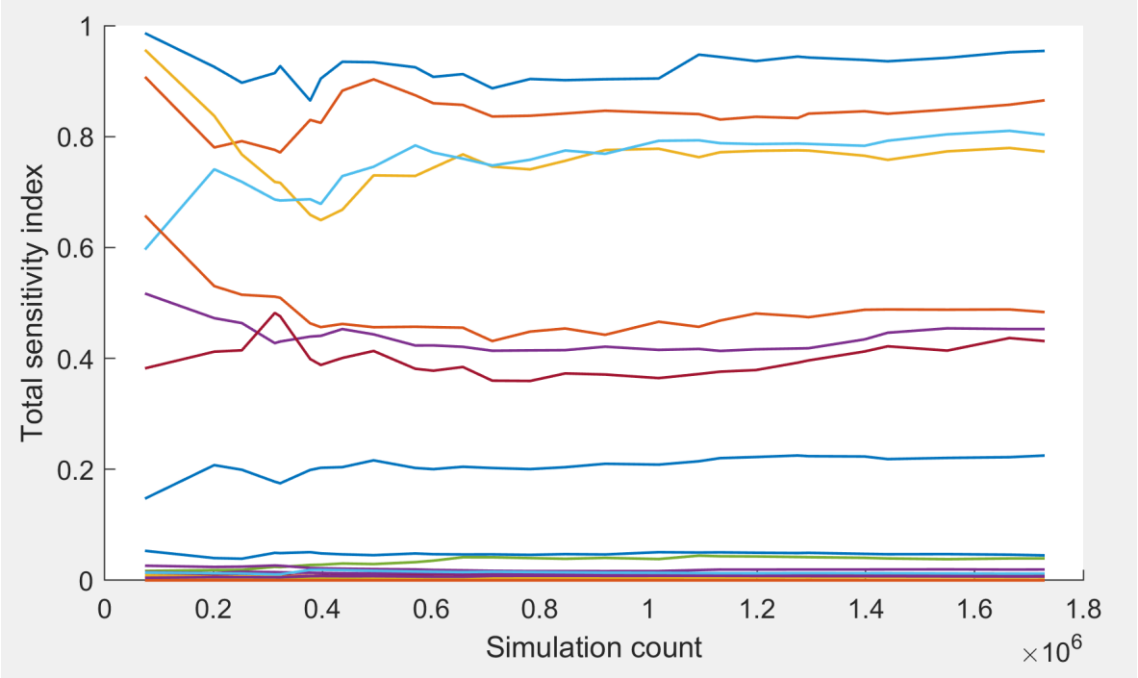

Figure B.2. Convergence plot of global sensitivity analysis for well-plate parameters, when the analyzed response is the osteoblast-only cell count

Appendix C. Statistical significance of experimental measurements for gene expression during osteogenesis in well plates

This appendix presents experimental measurements of gene expression for well-plate cultures, together with statistical significance markers.

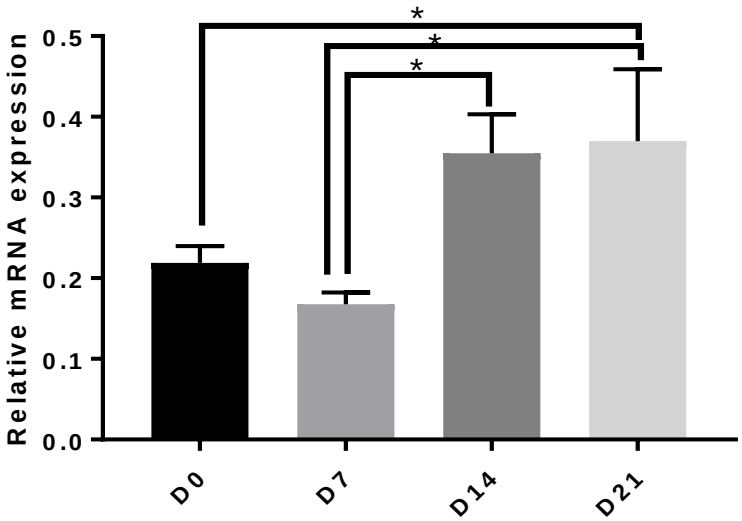

Figure C.1. Experimental measurements for *Runx2* expression during osteogenesis of mesenchymal stem cells in well-plate cultures, with statistical significance markers; the capital letter D on the horizontal axis denotes the day of the measurement

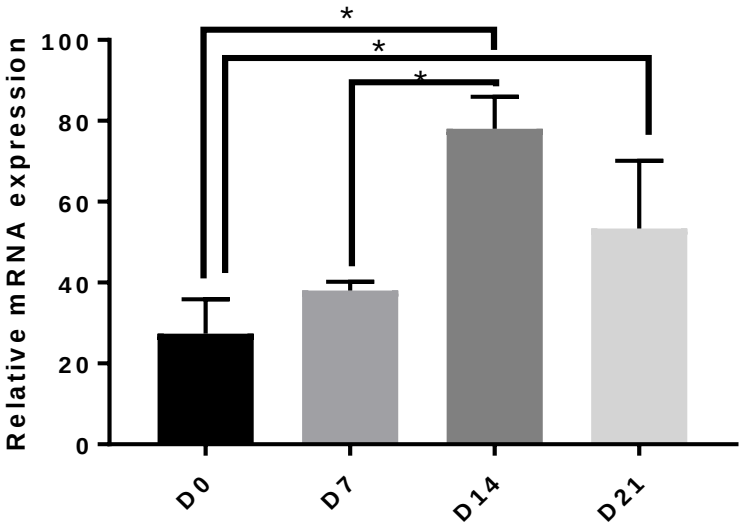

Figure C.2. Experimental measurements for *osteonectin* expression during osteogenesis of mesenchymal stem cells in well-plate cultures, with statistical significance markers; the capital letter D on the horizontal axis denotes the day of the measurement

Appendix D. Convergence of sensitivity analysis for bioreactor parameters

This appendix includes plots of the total sensitivity indices of the parameters included in the global sensitivity analysis for the bioreactor model presented in Chapter 3. Figure D. shows the complete history of sensitivity index values, while Figure D.2 only shows index values calculated using between 10,000 and 14,000 simulations.

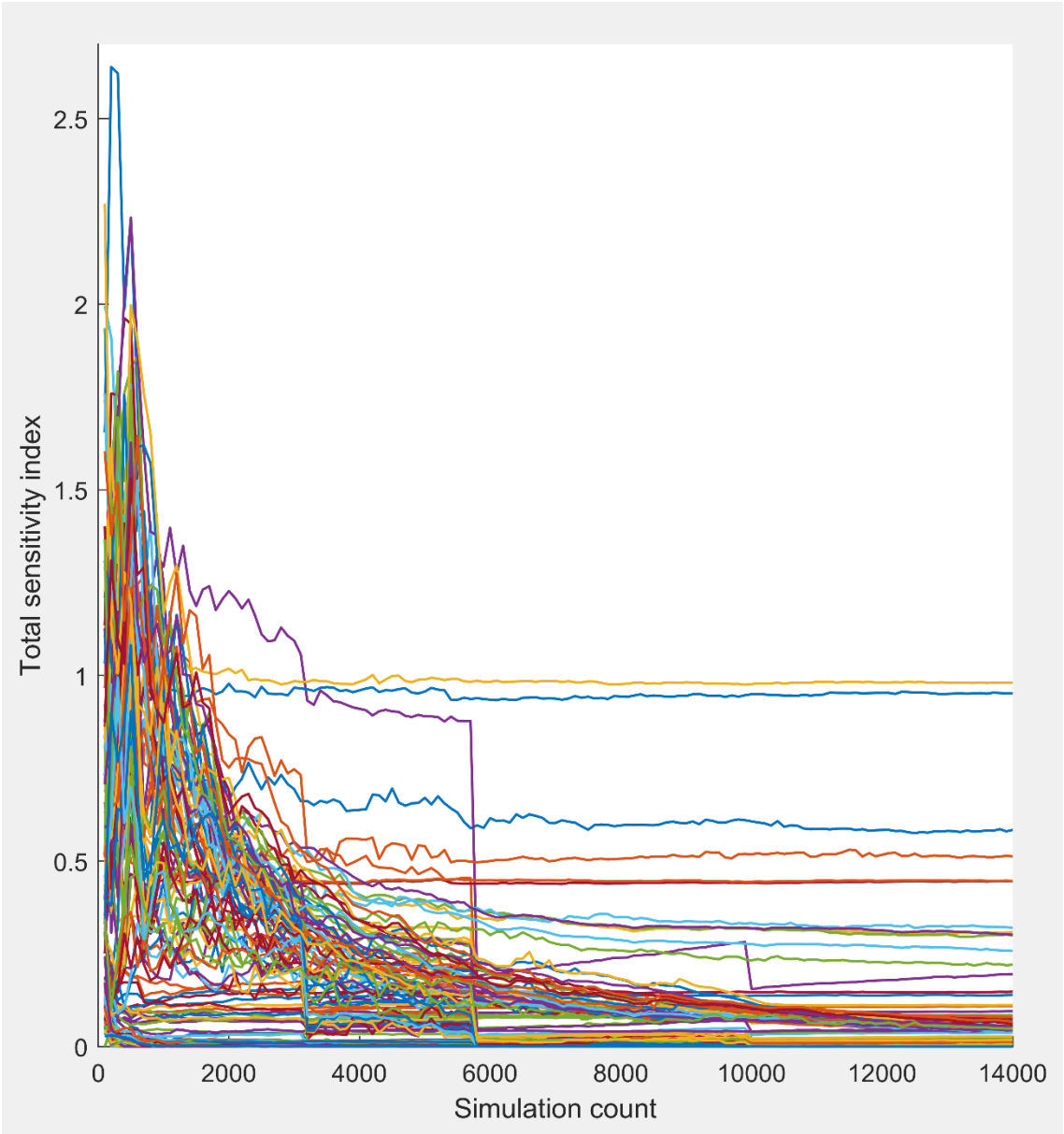

Figure D.1. Convergence plot of global sensitivity analysis for bioreactor parameters

For the figures included in this appendix the values on the horizontal axis indicate the number of simulations that were used in the calculation of (sensitivity index) values plotted on the vertical axis.

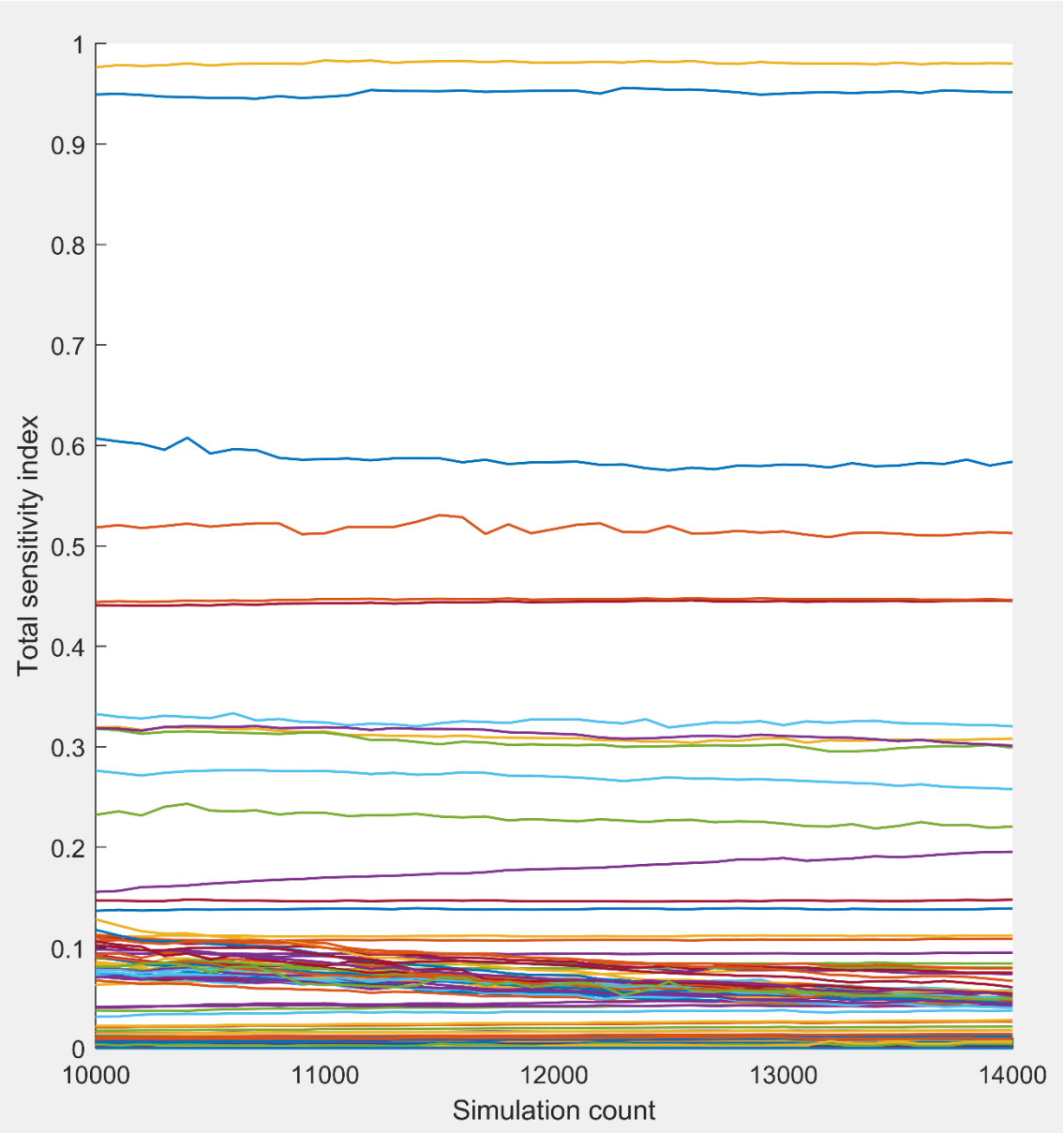

Figure D.2. Convergence plot for global sensitivity analysis showing only the last 4,000 iterations (out of 14,000 in total)